



# Goethe Universität Frankfurt

FRANKFURT INSTITUTE FOR ADVANCED  
STUDIES

Master thesis

## Twin stars in a modified chiral mean field model

Pia Jakobus

Supervisor and 1<sup>st</sup> examiner:

Prof. Horst STÖCKER

2<sup>nd</sup> examiner:

Dr. Jan STEINHEIMER-FROSCHAUER

June 29, 2020



## CONTENTS

---

<b>1 THEORETICAL BACKGROUND</b>	<b>7</b>
<b>1.1 Neutron star properties . . . . .</b>	<b>8</b>
<b>1.1.1 Tolman-Oppenheimer-Volkoff equation . . . . .</b>	<b>9</b>
<b>1.1.2 Tidal deformability . . . . .</b>	<b>12</b>
<b>1.1.3 Stability and Twin stars . . . . .</b>	<b>21</b>
<b>1.2 Equation of state . . . . .</b>	<b>24</b>
<b>1.2.1 Chiral symmetry breaking . . . . .</b>	<b>25</b>
<b>1.2.2 The Bag model . . . . .</b>	<b>27</b>
<b>1.2.3 Standard MIT bag model . . . . .</b>	<b>29</b>
<b>1.2.4 Vector-interaction-enhanced Bag model . . . . .</b>	<b>33</b>
<b>1.2.5 Chiral mean field model (CMF) . . . . .</b>	<b>34</b>
<b>2 RESULTS</b>	<b>39</b>
<b>2.1 Numerical implementation . . . . .</b>	<b>39</b>
<b>2.2 Investigation of the CMF-Model . . . . .</b>	<b>41</b>
<b>2.3 Standard MIT bag model . . . . .</b>	<b>49</b>
<b>2.3.1 Two and Three flavor MIT Bag model . . . . .</b>	<b>52</b>
<b>2.3.2 Investigation of flavor effects . . . . .</b>	<b>55</b>
<b>2.4 vMIT bag model . . . . .</b>	<b>63</b>
<b>2.5 Seidov limit and Twin stars . . . . .</b>	<b>67</b>
<b>2.6 Conclusion and outlook . . . . .</b>	<b>72</b>
<b>A WEIGHT OF A PINHEAD</b>	<b>75</b>



## LIST OF FIGURES

---

Figure 1	Pressure profile for a white dwarf . . . . .	13
Figure 2	Map of light-based observatories and gravitational wave detectors . . . . .	14
Figure 3	Gravitational wave signals . . . . .	15
Figure 4	Example visualization for a binary merger . . . . .	17
Figure 5	Constraints for M-R relations (left) and Twin star configuration (right) . . . . .	23
Figure 6	Twin stars classification schemes . . . . .	24
Figure 7	Quarks inside a Bag . . . . .	27
Figure 8	lQCD phase diagram . . . . .	33
Figure 9	Crust equation of state . . . . .	38
Figure 10	Results for the CMF model . . . . .	44
Figure 11	Particle population and $\sigma$ -field for the CMF model . . . . .	47
Figure 12	Tidal deformability (left) and speed of sound (right) for the CMF model . . . . .	48
Figure 13	Grid of parameter-space for randomly generated EoS . .	50
Figure 14	EoS for different Bag constants . . . . .	51
Figure 15	Results for the 2 and 3 flavor Bag model . . . . .	54
Figure 16	Results for the variation of the Stefan-Boltzmann limit II .	57
Figure 17	Results for variation of the Stefan-Boltzmann limit I . .	58
Figure 18	Comparison of the pure quark star maximum masses with the M-R relation of the modified EoS . . . . .	60
Figure 19	M-R relations for different Bag constants and EoS for different Stefan-Boltzmann limits . . . . .	62
Figure 20	Results for the vMIT model . . . . .	65
Figure 21	Results for the vMIT model . . . . .	66
Figure 22	Mass-radius-relations for different Seidov-limits . . . . .	69
Figure 23	Tidal deformability $\Lambda$ as function of radius for different Seidov-limits . . . . .	70
Figure 24	Love number $k_2$ as function of radius for different Seidov-limits . . . . .	71

## ACRONYMS

<b>AI</b> Artificial Intelligence	48	<b>MIT</b> Massachusetts Inst. of Technology	28, 29, 31, 63
<b>CMF</b> chiral mean field model	25, 26, 35, 37, 38, 41, 44, 46, 48, 49, 51–53, 55–63, 65–71, 73	<b>NS</b> neutron star	7–9, 12–15, 18, 21, 22, 25, 30, 31, 33, 35, 36, 44, 46, 59, 72, 73, 75
<b>EoS</b> equation of state	8, 11–13, 18, 19, 21–23, 33–35, 37–39, 41, 42, 44, 45, 48–72	<b>QCD</b> quantum chromodynamics	8, 24, 26, 27, 49, 56
<b>lQCD</b> lattice quantum chromodynamics	24, 33, 34, 45, 49, 72	<b>TOV</b> Tolman-Oppenheimer-Volkoff	9–13, 21, 39, 48, 49, 52, 59, 61
<b>M-R relation</b> mass radius relation	12, 22–24, 45, 49, 52–60, 63, 65–71	<b>vMIT</b> vector interaction Bag model	27, 33, 34, 52, 63, 64, 66, 67, 72

## THEORETICAL BACKGROUND

---

This thesis investigates the possibility of hybrid twin **neutron stars (NSs)**.

Our galaxy contains around  $10^8 - 10^9$  **NSs** [1]. Many of the observed **NSs** are pulsars, i.e. rotating objects with rotational periods up to a few milliseconds [2]. **NSs** form during supernovae explosions when massive stars, after they fulfilled all elements up to iron, collapse. As far as we know, they are the densest objects in our universe, except for black holes. The density of **NS** matter is running over many orders of magnitudes. Estimates indicate that the achieved densities in **NS** cores lie at  $n_0 \gtrsim (4 - 7) n_0^1$  [4]. A pinhead of neutron star matter would weight more than the world population (see Appendix A). The escape velocity of a **NS** lies at about half the speed of light  $\frac{c}{2} \sim 150\,000$  km/s, by comparison, our earth has an escape velocity of about 11 km/s. Furthermore, they have extremely strong magnetic fields of the order  $10^{15}$  G [5]. In 2004 the outburst of a magnetar<sup>2</sup> caused an ionospheric disturbance on earth, recorded all around the globe [6]. This magnetar, called SGR 1806-20, is located 50.000 light years away from our solar system which is about one quarter to one third of the diameter of our milky way away from earth.

The record mass claim for a **NS** is  $2.17_{-0.10}^{+0.11} M_\odot$ , from a pulsars PSR J0740+6620 which was recently observed [7]. It is difficult to obtain precise measurements for radii since they are more sensitive to properties like composition of **NS** atmospheres, magnetic fields, accretion and distance to the source [8]. Currently observed **NS** radii are in the range 9 – 13 km with large error bars of around 10% [9, 10]. Central **NS** densities reach several times the density of normal nuclear matter [11]. So how can one observe and measure an object that does not emit light by thermonuclear fusion? In fact, there are two connected properties of **NSs** that make them detectable: First, as already mentioned, **NSs** rotate. Second and similar to conservation of angular momentum, there is a conservation of magnetic flux. This leads in total, to giant magnetic fields. This magnetization leads to an acceleration of particles along magnetic field lines

---

<sup>1</sup> $n_0 \approx 2.3 \cdot 10^{17} \frac{\text{kg}}{\text{m}^3}$  is the nuclear saturation density above which hadrons start to overlap [3].

<sup>2</sup>A **NS** with extraordinary strong magnetic fields

and an ejection of electromagnetic radiation near the magnetic poles. The electromagnetic radiation can be measured on earth, PSR B1913+16, better known as the Hulse-Taylor pulsar binary, was first observed in 1974. It was recorded by Bell Burnell and the discovery rewarded with the Nobel Price in 1993<sup>3</sup>. NSs can also radiate X-rays which is a result of the accretion of mass from low-mass companions in a binary system.

All these remarkable properties give an impression of these “extreme” objects and also a sense of why their exploration through effort at astrophysical laboratories is so important. Because of their high densities, they could contain quark matter [12]. Therefore they might play a decisive role for low to high energy physics in the exploration of the strong interaction and the **quantum chromodynamics (QCD)** phase diagram [13]. Next to particle accelerators like the Large Hadron Collider (LHC) at CERN, Facility for Antiproton and Ion Research (FAIR) at GSI Darmstadt, Nuclotron-based Ion Collider fAcility (NICA), High Intensity Heavy-Ion Accelerator Facility (HIAF) in China, Japan Proton Accelerator Research Complex (J-PARC), NSs open an alternative window into the structure of the densest matter in our universe.

The latest observation of gravitational waves, emitted during the in spiral of NSs, created a new “back tracing” possibility by giving constraints to the equation of state with the so called tidal deformability.

### 1.1 NEUTRON STAR PROPERTIES

NS matter has a number of distinct properties which are important when one wants to consider physically relevant **equation of state (EoS)**:

- **Global charge neutrality**  $\sum_i n_i Q_i \simeq 0$ :

If there was a global net charge on the surface of stars then the coulomb interaction would overwhelm the gravitational pull and the star would shed its outer layers [14, 15].

- **Baryon number conservation:**

The Baryon number is conserved. This follows from the U(1)-symmetry of **QCD** and the Noether-theorem [16].

- **Chemical equilibrium:**  $\sum_i \mu_i dN_i = 0$

If a system of  $N_i \times i$  particle species  $i$  is in detailed balance, meaning that

---

<sup>3</sup>received by Hulse and Taylor, not Burnell

reaction and back-reaction are balanced and  $N_i$  is approximately constant averaged over spacetime, then it is said to be in chemical equilibrium so that the chemical composition is fixed. From this condition follows a relation between the different particle chemical potentials  $\mu_e + \mu_p = \mu_{\nu_e} + \mu_n$  [13]. The Baryon charge is conserved because proton decay has not been observed. The dominating reaction in NS matter is  $e^- + p \rightarrow n + \nu_e$  (neutronisation). Neutrinos in cold matter interact weakly with their surroundings and escape the star. Their number is therefore not conserved and one sets their chemical potential to zero<sup>4</sup> so that the above reaction reduces to  $\mu_e + \mu_p = \mu_n$ . This is called beta equilibrium.

- **Isospin asymmetry:**

Neutrons make up more than 70% of NS matter, which therefore is highly asymmetric in isospin.

### 1.1.1 Tolman-Oppenheimer-Volkoff equation

The Tolman-Oppenheimer-Volkoff (TOV) equation describes the balance of hydrostatic pressure and gravitational pull in general relativity and is used to calculate the masses and radii of spherically symmetric objects containing isotropic material in static gravitational equilibrium. In order to obtain solutions to the TOV equation, one first solves the Einstein equation

$$-8\pi GT^{\mu\nu} = R^{\mu\nu} - \frac{1}{2}g^{\mu\nu}R \equiv G^{\mu\nu} \quad (1)$$

where  $R^{\mu\nu}$ ,  $R$  are Ricci curvature and scalar curvature of the metric tensor  $g^{\mu\nu}$ , respectively.  $T^{\mu\nu}$  represents matter. These equations are a set of 10 non-linear partial differential equations containing partial derivatives of the metric tensor  $g_{\mu\nu}$  with the signature  $(+, -, -, -)$ . Mass and Energy are conserved so that the Einstein tensor  $G_{\mu\nu}$ , by construction, has a vanishing covariant divergence  $(G_{\mu\nu})_{;\nu} = 0$ . The TOV equation can be obtained by solving the Einstein equation for a spherically symmetric, static case. In this scenario the solution has the following form:

- The inner solution, which describes the metric inside a mass distribution where  $G_{\mu\nu} \neq 0$

---

<sup>4</sup>However, neutrinos contribute significantly to cooling processes in NSs [17]

- The outer solution with a vanishing Einstein Tensor  $G_{\mu\nu} = 0$ <sup>5</sup>.

These solutions were derived by Schwarzschild in 1915 [18]. The components of the Schwarzschild metric are time independent<sup>6</sup>. From the metric, one can obtain the curvature of spacetime. The scalar curvature for isotropic static spacetime is given by

$$R = e^{-2\alpha} R_{00} - e^{-2\beta} R_{11} - \frac{2}{r^2} R_{22} \quad (2)$$

with the isotropic static metric chosen by

$$\begin{aligned} g_{00} &= e^{2\nu(r)} \\ g_{11} &= -e^{2\lambda(r)} \\ g_{22} &= -r^2 \\ g_{33} &= g_{22} \\ g_{\mu\nu} &= 0, \mu \neq \nu \end{aligned}$$

For the TOV equation we now look at a solutions inside a star where  $G_{\mu\nu} \neq 0$ . Using the Einstein equation 1, we obtain for an isotropic, static star<sup>7</sup>

$$G_0^0 = e^{-2\lambda} \left( \frac{1}{r^2} - 2 \frac{\lambda'}{r} \right) - \frac{1}{r^2} \quad (3)$$

$$G_1^1 = e^{-2\lambda} \left( \frac{1}{r^2} - 2 \frac{\nu'}{r} \right) - \frac{1}{r^2} \quad (4)$$

$$G_2^2 = e^{-2\lambda} \left( \nu'' + \nu'^2 - \lambda' \nu' + \frac{\nu' - \lambda'}{r} \right) \quad (5)$$

$$G_3^3 = G_2^2, \quad (6)$$

where the prime denotes radial derivatives. The symmetric second rank Einstein curvature tensor  $G_{\mu\nu}$  implies that the energy momentum tensor has the same properties. Its general form is  $T^{\mu\nu} = -pg^{\mu\nu} + (p + \epsilon)u^\mu u^\nu$  but in the case of a static star the spatial components of the four velocity are zero. One therefore obtains

$$T_0^0 = \epsilon \quad (7)$$

---

<sup>5</sup>For the outer solution the Ricci Scalar and Tensor also vanish, which follows from eq. 1

<sup>6</sup>The Birkhoff theorem states that all spherically symmetric mass distributions are static and asymptotically flat and therefore the exterior solutions are given by the Schwarzschild metric [19]

<sup>7</sup>for convenience one works with mixed tensors for static isotropic fields

$$T_i^i = -p, \quad i \neq 0 \quad (8)$$

with the local fluid four velocity  $u^\mu = \frac{dx^\mu}{d\tau}$ .  $p(\epsilon)$  is called **EoS** and the characteristic function of the implicit **TOV** differential equation. The solution of the **TOV** equation with a given **EoS** determines the values for masses and radii of differently composed stars. Using the Einstein eq. 1 and our definition of the energy momentum tensor  $T_\nu^\mu$  one obtains

$$G_0^0 = -8\pi G\epsilon(r) \quad (9)$$

$$G_1^1 = 8\pi P(r) \quad (10)$$

$$G_2^2 = 8\pi P(r) \quad (11)$$

$$G_3^3 = G_2^2 \quad (12)$$

We can now solve this set of differential equations for  $\nu, \lambda$ . With the gravitational mass

$$M(r) = 4\pi \int_0^r \epsilon(r)r^2 dr$$

the final result for the **TOV** equation is

$$\frac{dP}{dr} = -\frac{G\epsilon(r)M(r)}{c^2 r^2} \left[ 1 + \frac{p(r)}{\epsilon(r)} \right] \left[ 1 + \frac{4\pi r^3 p(r)}{M(r)c^2} \right] \left[ 1 - \frac{2GM(r)}{rc^2} \right]^{-1} \quad (13)$$

There are three things which can be observed here:

1. Eq. 13 has a coordinate singularity for  $r = 0$ <sup>8</sup> and one true singularity<sup>9</sup> at  $r_s = 2GM$ . Stars with radii below their Schwarzschild radius collapse into black holes.
2. The mass term is not to be confused with the baryon mass of the star. The gravitational mass and thus potential of a **TOV** star is the energy necessary to decompose the star into its components. The baryon mass is the sum of all baryon masses inside the star. The mass of the star (with mass I refer to the gravitational mass) is smaller than its baryonic mass and the difference is proportional to the star's compactness and can be as large as 25% of the gravitational mass [20].

---

<sup>8</sup>The numerical integration starts from small values of  $r$ .

<sup>9</sup>True singularity means that one can not gauge the singularity away by coordinate transformation.

3. Eq. 13 has a negative sign since all parameters are positive and  $r \leq 2GM$ . Fig. 1 shows that the pressure falls monotonically and approaches zero at the surface of the star. This is the condition which is used to stop the numerical integration method. On the surface  $P = 0$ , otherwise the star is unstable.
4. In the non relativistic limit  $c \rightarrow \infty$ , the relativistic corrections vanish and one obtains the Newtonian formulation

$$\frac{dp}{dr} = -\frac{G\pi\epsilon(r)m(r)}{c^2r^2}$$

One solution of the TOV equation corresponds to a star configuration with a given mass  $M$  and radius  $R$ . The profile of the star is determined by the initial pressure at  $p(\delta r) = p_c$  and  $m(\delta r) = 0$ <sup>10</sup>. The masses and radii of the stars are ambiguous, meaning that for different starting conditions, given one EoS, it is possible to obtain identical radii and masses (one point in the [mass radius relation \(M-R relation\)](#)). Solutions with two identical masses but different radii are called Twin star solutions and are discussed in detail in section 1.1.3. We can illustrate the solutions of the TOV equation for slightly less extreme objects. Low or medium mass stars ( $\leq 8M_\odot$ ) that do not burn up to iron in a thermonuclear process (due to their lower masses compared to NSs) end up as white dwarfs. These objects are also extremely dense, but less than NSs. A typical white dwarf with one solar mass would have a radius in the range of the earth's radius. Fig. 1 shows an example of a non-relativistic polytropic EoS using a free degenerate electron gas assumption. The EoS reads

$$P \propto \epsilon^{5/3}$$

Different pressures in the stellar interior lead to different masses and radii. The curved lines show the decrease of pressure when moving away from the stellar interior. Fig. 1 is only a toy-plot for a star's profile, this is why I dropped the numbers of x- and y-axis.

### 1.1.2 Tidal deformability

The tidal deformability describes the deformation of an object driven by tidal fields. A tidal field is generated by a time changing gravitational field. The

---

<sup>10</sup>As already mentioned, eq. 13 diverges for  $r = 0$  so one chooses a small value  $\delta r$  to start the numerical integration.

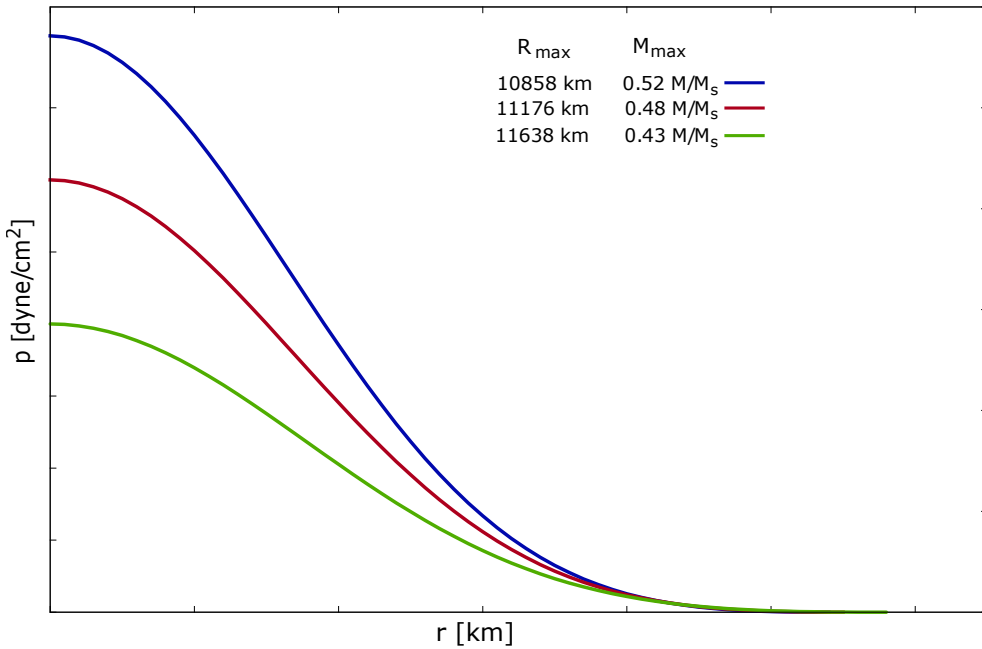


Figure 1: Qualitative example of a white dwarf pressure profile. The pressure is given as function of radius for one given EoS and plugged in the TOV eq. 13. The blue configuration has the highest starting pressure that leads to the highest mass of the star. Vice versa, the lowest (green) lines correspond to the star with the lowest initial pressure and smallest mass.

tidal deformability is sensitive to a deformed object's internal structure and measurable with gravitational field detectors. This makes this parameter very interesting in terms of investigating with regard to compact star physics. I know want to give a brief overview how tidal deformability is specifically related to NS merger before I introduce some mathematical concepts.

NS merger emit gravitational waves because of their spacetime changing gravitational field. The orbital radii of both objects decrease while the orbital velocity increases up to a point where both objects merge. This motion is called NS inspiral. Fig. 4 shows a simplified neutron binary merger. At its late stage, the frequency of the radiated gravitational waves lies within the range of the earth based detectors. A signal is shown in the left plot of fig. 3 where frequency as function of time is shown for the binary merger event GW170817, recorded by the 3 biggest gravitational wave detectors LIGO and VIRGO.

<sup>11</sup>[www.ligo.caltech.edu/image/ligo20171016e](http://www.ligo.caltech.edu/image/ligo20171016e)

<sup>12</sup>[www.ligo.org/detections/GW170817.php](http://www.ligo.org/detections/GW170817.php)

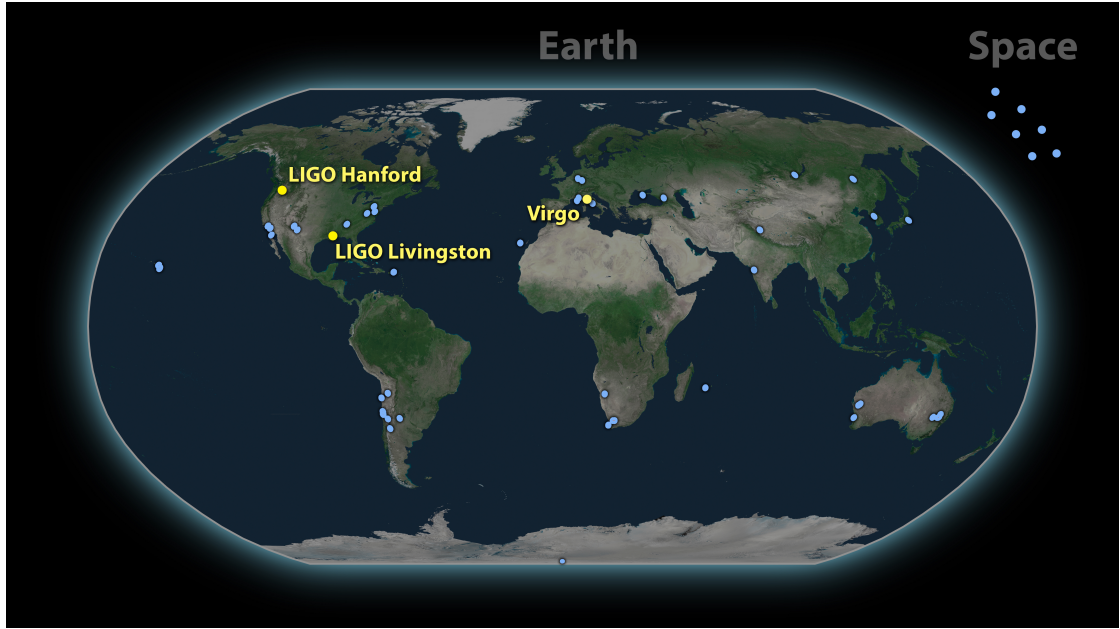


Figure 2: Map of the 70 light-based observatories and gravitational waves detectors that detected the aftermath of the gravitational wave event. On August 17 in 2017, the gravitational wave detectors LIGO and VIRGO registered signals from colliding NSs<sup>11</sup>.

### 1.1.2.1 Tidal response of a NS

We want to understand the concept of tidal deformability, therefore one first needs to introduce the tidal response of a NS to an external tidal field by which it is deformed. In Newtonian gravity, the curvature of the scalar potential  $U_G(r)$  of a **static** spherical symmetric body with mass distribution  $\rho(r)$  is proportional to its mass density  $\rho(r)$

$$\nabla^2 U_G(r) = -4\pi\rho(r); \quad r \leq R \quad (14)$$

where  $R$  is the radius of the star. The solution of this differential equation can be obtained from the solution of the Poisson equation  $\nabla^2 U(r) = -4\pi\rho(r)$ . Outside the star at  $r > R$ , the mass distribution is zero that  $\nabla^2 U_G(r) = 0$ . This equation is called Laplace's equation and one solution is the free Green's function, also called Newton kernel<sup>13</sup>. A generating function set to expand the Newton kernel is the Laplace expansion which is written in terms of the Legendre polynomials  $P_l(\cos \gamma)$  [21]. It is possible to rewrite the Newtonian

---

<sup>13</sup>The general form of the Newton kernel is  $G(r, r') = -\frac{1}{4\pi} \frac{1}{|r-r'|}$

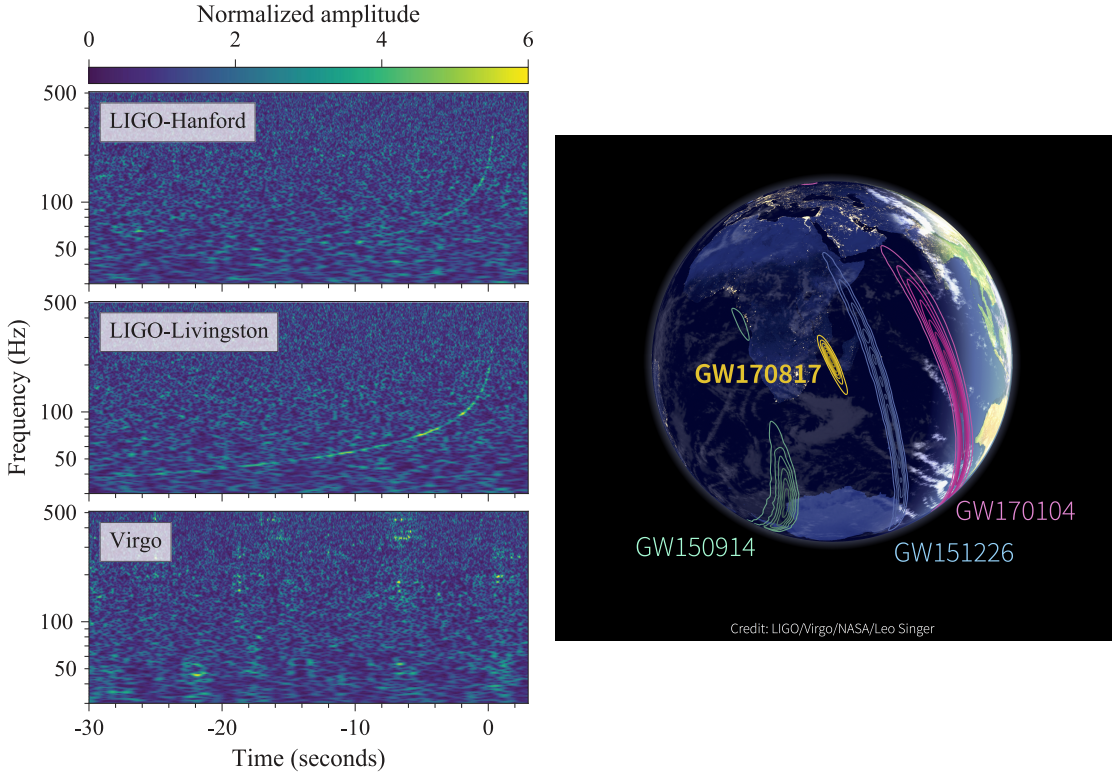


Figure 3: **Left:** Chirp signal of the NS inspiral from August, 2017 as function of time. The color indicates the strength of the signal. **Right:** Sky locations of the gravitational waves signals from 2015 up to 2017 projected onto the earth's surface. Since VIRGO first came online in 2017, the error of the signal (GW170817) was dramatically reduced<sup>12</sup>.

potential in its Laplace expanded form around a mass center at  $r = 0$  and in terms of the tidal moments  $\mathcal{E}_L$  of the form

$$U_{G;\text{ext}}(r) = - \sum_{l=0}^{\infty} \frac{1}{(l-1)!} r^l \mathcal{E}_L \Omega^L \quad (15)$$

where  $\Omega^L := \Omega^{a_1}\Omega^{a_2}\dots\Omega^{a_l}$  are  $l$  angular vectors [22]

$$\Omega := [\sin \theta \cos \Phi, \sin \theta \sin \Phi \cos \theta]$$

$\mathcal{E}_L$  is a set of  $l$  symmetric, trace free tidal moment tensors, called tidal moments

$$\mathcal{E}_L := -\frac{1}{(l-2)!} \partial_L U_{\text{ext}}(0) \quad (16)$$

The subscript  $L$  indicates a set of indices  $\{a_1 a_2 \dots a_l\}$  and  $\partial_L := \partial_{a_1} \partial_{a_2} \dots \partial_{a_l}$ . This tidal field is sourced by the Newtonian potential of eq. 14.

One can formulate the  $(2l + 1)$  coefficients of the tidal tensor in terms of spherical harmonics<sup>14</sup> of the form

$$\mathcal{E}_L \Omega^L = \sum_{m=-l}^l \mathcal{E}_m^{(l)} \mathcal{Y}_{lm}(\theta, \phi) \quad (17)$$

The tidal field in eq. 17 has **electric-type** tidal moments. This means that the spherical harmonics have even parity given their integers  $l$  and  $m$  [23].

$$\mathcal{Y}_{lm} \rightarrow (-1)^l \mathcal{Y}_{lm}$$

We focus on even parity perturbations since these type tidal fields generate gravitational waves. Given a tidal field  $\mathcal{E}_L$  from a star B we want to express the induced multipole deformation  $Q_L^{\text{adiab}}$  of the companion star A.

$$Q_L^{\text{adiab}} = -\lambda_l \mathcal{E}_L \quad (18)$$

$Q_L^{\text{adiab}}$  is a symmetric, trace free tensor and contains the tidal moments as defined in eq. 17. Eq. 18 tells us that the deformation  $Q_L^{\text{adiab}}$  of a star B is proportional to the tidal field  $\mathcal{E}_L$  of the reference body of the deformed companion star in the adiabatic limit<sup>15</sup>. Adiabatic limit means that the time scale of the variation of the tidal field is much smaller than the variation of the bodies internal structure  $\tau_{\text{tidal field}} \ll \tau_{\text{internal}}$  [24]. The tidal coefficients  $\lambda_l$ , sometimes also called tidal polarizability [24], define the ratio between a tidal field  $\mathcal{E}_L$  and its induced multipole moments  $Q_L^{\text{adiab}}$  of a companion star B. They are given by

$$\lambda_l = \frac{2(l-2)!}{(2l-1)!!} k_l R^{2l+1} \quad (19)$$

This equation relates the quadrupole tensor  $Q_{ab}$  of the deformed compact star to the tidal field  $\mathcal{E}_{ab}$  of the companion star. A visualization of this concept is shown in fig. 4.

$k_l$  are the body's Love numbers that had first been described by E.E.H. Love in 1909 and  $R$  denotes the radius of the star [25]. For this thesis we look at deformations up to  $l = 2$  quadrupole order, I will refer to  $k_l$ , with  $l = 2$  as  $k_2$  Love number from now on. There is no deformation of the star in the absence

---

<sup>14</sup>the spherical harmonics appear as scalar, vector and tensor spherical harmonics

<sup>15</sup>The multipole moments can be expanded in tensor spherical harmonics  $\mathcal{Y}_L^{lm}$  of the form  $Q_L = \frac{l!}{(2l-1)!!} \sum_{m=-l}^l Q_{lm} \mathcal{Y}_L^{lm}$ , where the subscript  $l$  stands for the  $l$ 'th multipole of the tidal field  $\mathcal{E}_L$  and quadrupole  $Q_L$ .

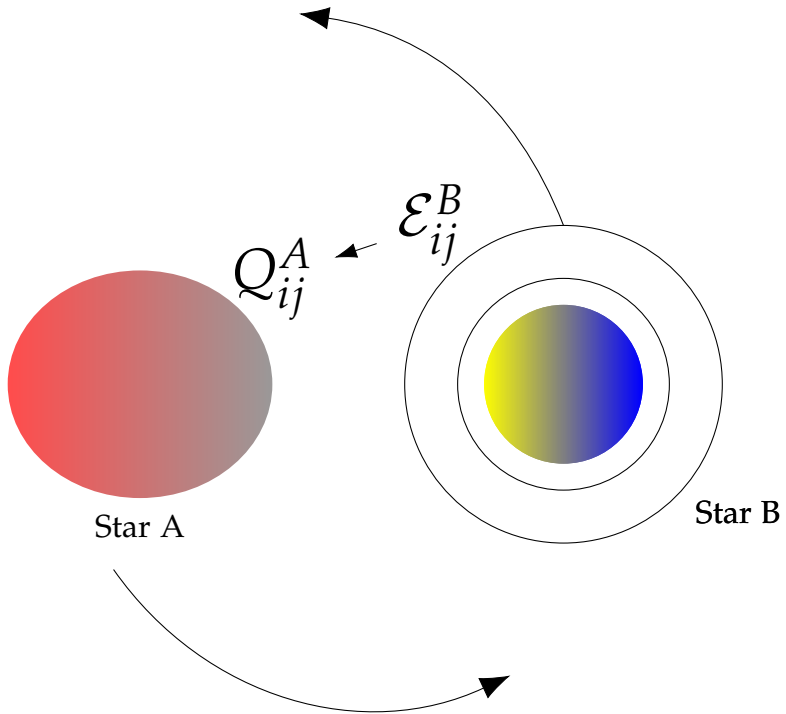


Figure 4: We see two stars that orbit each other. Star B is more compact than star A. I have drawn the gravitational isolines of star B as circles and we assume that  $M_{\text{StarB}} \gg M_{\text{StarA}}$ . If  $M_{\text{StarB}}$  is very big then there is large gradient of the gravitational field of star B and star A gets distorted. The tidal field  $\mathcal{E}_{ij}$  encodes the strength of the gravitational pull from star B onto star A,  $Q_{ij}^A$  is a measure for the tidal response of the lighter companion star A, it gives information about how strongly star A is deformed by star B. This deformation is sensitive to star A's microscopic structure. The tidal deformability  $\Lambda$  that encodes the deformation is indirectly measurable by gravitational wave detectors. This opens up a new window for investigating extremely dense matter.

of a tidal field and the quadrupole moment vanishes since the star is symmetric. For non-zero tidal fields up to quadrupole order, eq. 18 becomes

$$Q_{ab} = -\frac{2}{3}k_2 R^5 \mathcal{E}_{ab} \quad (20)$$

$k_2$  refers to the  $l = 2$  tidal Love number and  $R$  is the radius of the deformed star. The next step is now to relate the  $l = 2$  tidal moment tensor  $\mathcal{E}_{ab}$  to the curvature of spacetime, i.e. the Riemann tensor. It can be shown that  $\mathcal{E}_{ab}$  relates to the  $R_{0a0b}$  components of the Riemann tensor [26].

Damour and Nagar classified the Love numbers into two categories [27]:

1. **Gravitational Love number:** deformation of bodies gravitational potential, as measured by  $l$ 'th multipole of its mass distribution
  - (a) **Electric-type:** Tensor spherical harmonics with even parity. Associated with gravito-electric part of gravitational field. Even parity motion change density and pressure inside the star and lead to the emission of gravitational waves [26].
  - (b) **Magnetic-type:** Tensor spherical harmonics with odd parity. Associated with Gravito-magnetic interaction. Odd-parity motions do not lead to gravitational waves.
2. **Surficial Love number:** Deformation of bodies surface (also expanded in multipole moments).

Thorne et al. give a physical interpretation of the non-existence of odd parity pulsations [26]. Because of the assumption of a perfect fluid where only isotropic stress is present, one rules out odd parity gravitational waves (that come from odd parity perturbation tidal fields) by definition which only couple to anisotropic stresses inside the star. Summarizing, we have the following points on the tidal deformability parameter

- The ratio of induced multipole moment and perturbing gravitational field is called tidal deformability.
- In 2007 Flanagan and Hinderer [28] suggested that the tidal deformability  $\lambda$  as measured by NS inspiral events can give insights in its internal structure of a NS by giving constraints to the EoS [22].
- The gravitational Love numbers of black holes are zero [29].

- The I-Love-Q relations (moment of inertia  $I$ , Love number  $k_2$  and quadrupole moment  $Q$ ) have been suggested to be universal, meaning that a ratio between the 3 parameters would then not be EoS dependent [30] whereas each quantity on its own strongly depends on the EoS.

### 1.1.2.2 Perturbation of spacetime

Relativistic equilibrium configurations in a coordinate system  $(t, r, \theta, \phi)$  can be formulated in the Schwarzschild metric with the line element [31]

$$ds = e^{\nu(r)} dt^2 - e^{\lambda(r)} dr^2 - r^2(d\theta^2 + \sin^2 \theta d\phi^2) \quad (21)$$

where  $e^{-\nu(r)} = e^{\lambda(r)} = (1 - 2M/R)^{-1}$ . Let's look at a coordinate transformation of the form

$$x^\alpha \rightarrow x'^\alpha = x^\alpha + \xi^\alpha \quad (\xi^\alpha \ll x^\alpha) \quad (22)$$

where  $\xi^\alpha$  is the fluid displacement vector. A small amplitude motion is formulated within the displacement vector  $\xi(t, r, \theta, \phi)$  which makes it no longer possible to formulate equilibrium configurations by the unperturbed Schwarzschild metric in eq. 21. A linear perturbation<sup>16</sup> metric tensor  $h_{\mu\nu} dx^\mu dx^\nu$  is added to the unperturbed line element  $ds_0^2$  containing 10 more entries  $h_{\mu\nu}(t, r, \theta, \phi)_{ij}$  because  $h_{\mu\nu}$  is symmetric

$$ds^2 \equiv (ds^2)_0 + h_{\mu\nu} dx^\mu dx^\nu \quad (23)$$

Before we can continue, we need to obtain the transformation behaviour of  $h_{\mu\nu}$  in terms of the metric displacement vector  $\xi^\mu$ . In the so called Regge Wheeler gauge, the coordinate system is chosen in a way so that  $h_{\mu\nu}$  transforms as

$$h_{\mu\nu}^{old} \rightarrow h_{\mu\nu}^{new} = h_{\mu\nu}^{old} + \xi_{\mu;\nu} + \xi_{\nu;\mu} \quad (24)$$

In this gauge the four vector  $\xi^\mu$  is a spherical harmonic and one also expresses the perturbation  $h_{\mu\nu}$  in terms of vector valued and tensor valued spherical harmonics [23]. The formulation of the metric perturbation  $h_{\mu\nu}$  in terms of spherical harmonics for the even parity (electric-type) perturbations<sup>17</sup> then becomes

$$h_{\alpha\beta} = \text{diag}[e^{\nu(r)} H_0, e^{\lambda(r)} H_2, r^2 K(r), r^2 \sin^2 \theta K(r)] \mathcal{Y}_{2m}(\theta, \phi) \quad (25)$$

---

<sup>16</sup>linear means that higher order perturbations  $\mathcal{O}(h_{\mu\nu}^2)$  in the metric are not taken into account

<sup>17</sup>A multipole perturbation of order  $l$  in spherical harmonics is determined by its quantum numbers  $(l, m, \pi)$ , where  $\pi^{(even)} = (-1)^l$  or  $\pi^{(odd)} = (-1)^{l+1}$ .

$\mathcal{Y}_{2m}(\theta, \phi)$  is a  $l = 2$  spherical harmonic function. There are also 3 unknown functions of  $r$  for the even case:  $(H_0, H_2, K)$ <sup>18</sup>.

Between here and the next step lie some tedious calculations. There is a good amount of literature for the derivation of the Love number  $k_2$  in which we are interested in this thesis. A lot of work has been written by Hinderer [28, 32, 24], which is mostly based on the early work of Regge, Wheeler, Thorne and Compoltaro [23, 26]. The main points within the full derivation are

- linearized expansion of Schwarzschild metric
- expansion of perturbed metric  $h_{\mu\nu}$  into spherical harmonics
- isolation of even parity part
- multipole expansion of external gravitational potential and induced tidal field
- expansion of induced tidal field into spherical harmonics
- formulation of mass distribution of (tidal field induced) companion star up to quadrupole order

For  $l = 2$  one obtains for the metric perturbation functions  $H_0 = H_2 \equiv H$  and its derivative  $\beta \equiv \frac{dH}{dr}$  [32]

$$\frac{dH}{dr} = \beta \quad (26)$$

$$\frac{d\beta}{dr} = 2 \left(1 - 2 \frac{m(r)}{r}\right)^{-1} H \left\{ 2\pi \left(5\epsilon(r) + 9p + \frac{d\epsilon(r)}{dp(r)}\right) + \frac{3}{r^2} \right. \quad (27)$$

$$\left. + 2 \left(1 - 2 \frac{m(r)}{r^2}\right)^{-1} \left(\frac{m(r)}{r^2} + 4\pi rp(r)\right)^2 \right\} \frac{2\beta}{r} \left(1 - 2 \frac{m(r)}{r}\right)^{-1} \quad (28)$$

$$\times \left\{ -1 + \frac{m(r)}{r} + 2\pi r^2(\epsilon - p(r)) \right\} \quad (29)$$

At the surface  $r = R$

$$y = \frac{R\beta(R)}{H(R)} \quad (30)$$

The  $l = 2$  Love number of eq. 19 is:

$$k_2 = \frac{8C^5}{5}(1 - 2C)^2[2 + 2C(y - 1) - y] \quad (31)$$

---

<sup>18</sup>There is actually one more unknown function  $H_1$  in the off diagonal of  $h_{01}$  and  $h_{10}$  component but in the static case (which is the one we are interested in) it can be shown that  $H_1$  vanishes [23]

$$\times \{2C[6 - 3y + 3C(5y - 8)]\} \quad (32)$$

$$+ 4C^3[13 - 11y + C(3y - 2) + 2C^2(1 + y)] \quad (33)$$

$$+ 3(1 - 2C)^2[2 - y + 2C(y - 1)\ln(1 - 2C)]\}^{-1} \quad (34)$$

with the compactness  $C \equiv M/R$ . Once we have calculated  $k_2$  the dimensionless tidal deformability  $\Lambda$  is given by

$$\Lambda = \frac{2k_2}{3C^5}. \quad (35)$$

$\Lambda$  is usually referred to as “tidal deformability” (instead of “dimensionless tidal deformability”), however some literature uses the notation  $\lambda$  which is related to the dimensionless  $\Lambda$  via

$$\lambda = \Lambda M^5 \quad (36)$$

and can be identified as the negative proportionality factor  $\lambda \equiv \frac{2}{3}k_2R^5$  between quadrupole moment  $Q_{ij}$  and tidal field  $\mathcal{E}_{ij}$ , see eq. 20.

### 1.1.3 Stability and Twin stars

With the TOV equation it is possible to obtain masses and radii of physically viable fluid stars. This required an EoS as external input. For each initial starting pressure, the TOV solution yields a mass and indirectly the radius (via the pressure profile). Masses and radii depend on macroscopic properties that are encoded in the EoS. There are 4 constraints for the stellar density profile [33, 34]

1. The average density decreases radially. NSs are densest in their core and monotonically decreasing outwards.
2. The mass density  $\rho \geq 0$  and  $\rho + P \geq 0$  (weak energy condition). For non-exotic matter,  $\rho$  is always positive.
3. Matter is microscopically stable. This is equivalently formulated as  $\frac{dp}{dr} \geq 0$ .
4.  $v_s^2 \leq c^2$ , this refers to the causal limit where  $v_s^2$  is the speed of sound defined as  $v_s^2 = \frac{dp}{dr}$ . For causality reasons the speed of sound can not be faster than the speed of light  $c$ .

If one does not consider any microscopical properties then the lowest limit for radii is the Schwarzschild radius. A star with a radius smaller than  $R_s$  collapses

into a black hole. A second limit is the Buchdahl limit that has some further constraints, namely point 1,2 and 3 from the upper list. This is expressed as

$$\frac{2M}{R} \leq \frac{8}{9}$$

and constitutes an upper limit for the compactness of a star prior to its gravitational collapse. It ignores point 4 so that the EoS can violate the causality limit. Fig. 5a show various M-R relations of different EoS. The dark shaded area indicates the black hole limit. In this case the radius of the star is smaller than its Schwarzschild radius and therefore collapses into a black hole. The light grey line is the Buchdahl limit. Stars within the Photon sphere area (white with grey lines) are compact objects that have strong gravitational fields which bend light. These photons form a so called photon sphere on the star's surface. The green area is compatible with the two solar mass constraint [35]. This constraint rules out many soft EoS because stiffness is an important criterion to obtain high massNSs. The dashed red line is the bound on the tidal deformability parameter  $\Lambda$  [36]. The tidal deformability has been indirectly measured from gravitational wave event GW170817. It is an EoS sensitive quantity which was discussed in numerous studies in context of GW170817.

Besides generic conditions arising from the density profile inside NSs, there exist also more “structural” conditions for stellar equilibrium . A branch in a M-R relation is called stable if:

- The mass decreases if one increases the central energy density. Figure 5b shows mass as function of a central core energy density [37]. The right side of each of the two maxima corresponds to a stable branch until it reaches a minimum. The stable branch at lower central energy density exhibits twin stars. Twin stars are stars with same masses but different radii. This so called BTM-criterion (Bardeen, Thorne, and Meltzer) is a rather heuristic but convenient way to look for twins/stability.
- One can look at radial oscillations of stars. The oszillation modes can be reduced to the Sturm-Liouville eigenvalue problem. The eigenmodes of the star are real valued if the star is in stellar equilibrium and imaginary otherwise. Imaginary oscillations would exponentially increase and make the star unstable. This is equivalent to the BTM criterion but formulated in a less heuristic way [38, 39, 37].

There are two convenient classification schemes for twin stars and M-R relations in general:

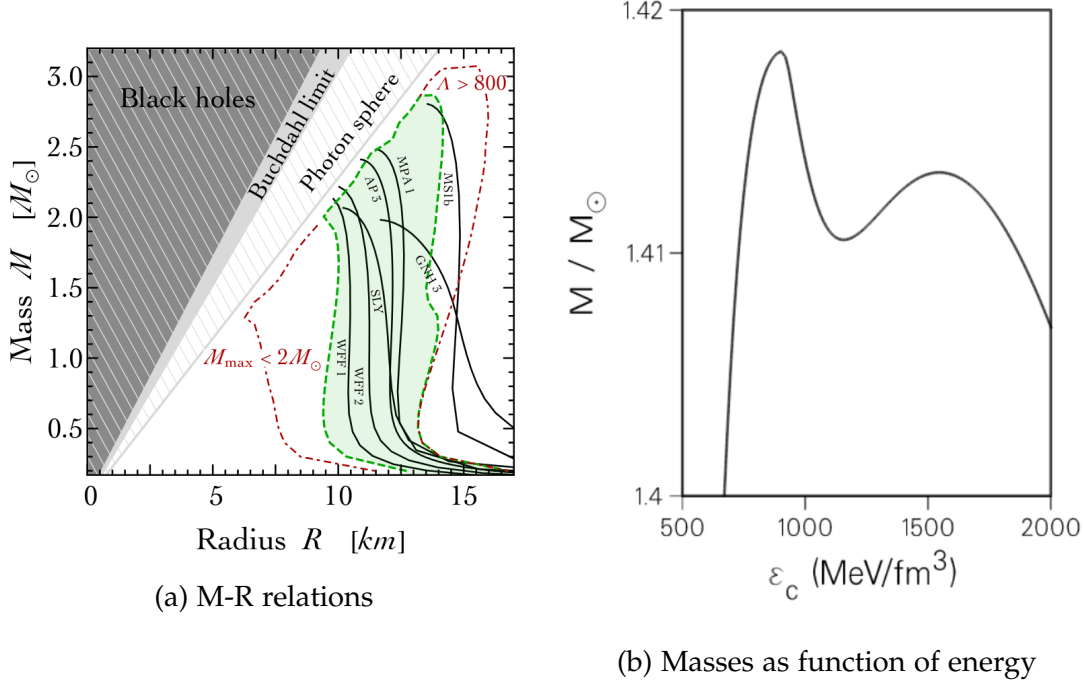
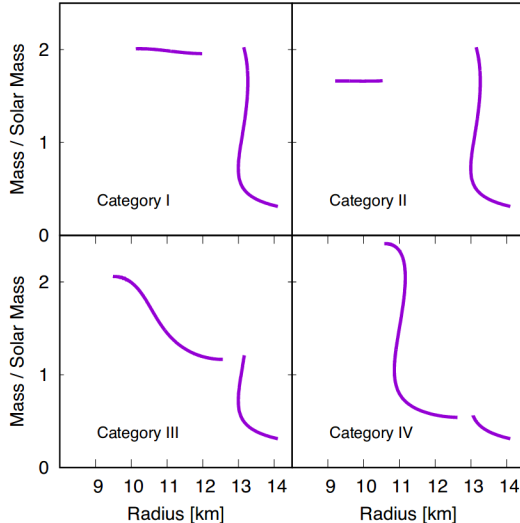


Figure 5: **Left:** M-R relation for different EoS with constraints from various observations [33]: The Black hole limit (dark grey area), Buchdahl limit (grey area) and Photon sphere (light grey area). The green area is a result from the two solar mass constraint. The red dashed area is the bound on the tidal deformability parameter. **Right:** Masses of stars as function of energy density in core [37]. The two maxima show twin star solutions. This means that two stable branches appear for one single EoS.

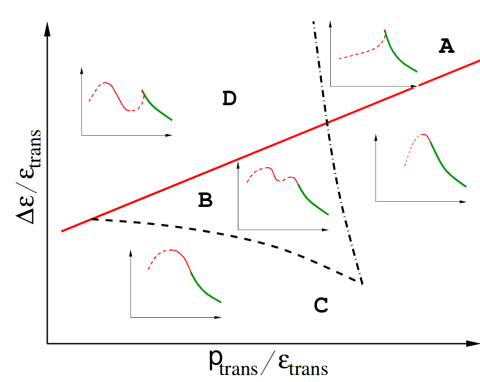
1. How are the different branches connected regarding the composition of the EoS, See fig. 6b and [40]
  - (a) A: no hybrid branch
  - (b) B: connected and disconnected hybrid branches
  - (c) C: one connected hybrid branch
  - (d) D: one disconnected hybrid branch<sup>19</sup>
2. In which range do both maximum masses lie and which branch has a higher maximum mass [41], see fig. 6a. The following attributes classify the twins

<sup>19</sup>Stars that inhibit quark content in their core are called hybrid stars

- (a) all masses of first branch are below  $1M_{\odot}$  (Category IV)
- (b) maximum mass of second branch is higher than first branch (Category III, possibly Category I)
- (c) maximum mass of second branch is lower than first branch (Category II, possibly Category I)
- (d) both maximum masses are above  $2M_{\odot}$  (Category I)



(a)



(b) Latent heat as function of pressure

Figure 6: Various classification schemes for twin stars. **Left:** The ratio of the two maxima of both branches classify M-R relations into four categories [41]. **Right:** Latent heat as function of transition pressure in units of transition energy density (for Maxwell construction). This classification theme depends on the star composition. The red line is the Seidov limit which divides M-R relations into connected and disconnected branches. Twin stars can occur above and below the Seidov limit and lie within the black dashed triangular line [40].

## 1.2 EQUATION OF STATE

QCD is the theory of strong interactions between quarks and gluons. Lattice quantum chromodynamics (lQCD) is an approach to solve QCD numerically in vacuum at vanishing chemical potential and finite temperatures. Numerical

difficulties (in particular the fermionic sign problem) prevent Monte Carlo methods at finite baryon density. A complex weight factor prohibits a probabilistic interpretation of the expectation value  $\langle A \rangle = \frac{1}{Z} \text{Tr } A \exp(-H/T)$  which is necessary for the usage of Monte Carlo methods [42, 43]. Particularly, this regime is of great interest for [NSs](#) and core-collapse supernova [44].

Phenomenological models of interacting quarks at high chemical potential and in the vicinity of the believed deconfinement phase transition are adopted to give an alternative approach to this density regime. There are generally two approaches to describe an equation of state

1. derive thermodynamic quantities like energy density and pressure within **two distinct models** and then chose the phase with the higher pressure at a given baryon density. At the crossing point both curves are either connected by a **Maxwell or Gibbs construction**. I use two models that describe two distinct phases. The [chiral mean field model \(CMF\)](#) model at lower chemical potential and the bag model for the quark phase. I connect these with a Maxwell construction.
2. an more sophisticated ansatz is to derive one single Lagrangian that is valid in both the hadronic and quark regime. The **CMF model** is such an approach. It has a crossover from hadrons to quarks. These kind of models are usually more “physical” in the sense that they are not patched together but rather result from fundamental quantum field theoretical and mathematical considerations. They are often very complicated and less phenomenological “intuitiv” than other models and may therefore be less appropriate to explore the physical mechanism leading to an observation.

### 1.2.1 Chiral symmetry breaking

The Noether theorem relates symmetries to conserved currents. A Lagrangian that is invariant under transformations possesses a globally conserved current. The baryon number is an example of an invariant under  $SU(1)$ -transformations, i.e. a multiplication with a local phase factor  $\theta^{20}$

$$\Psi(x) \rightarrow \exp(i\theta)\Psi(x)$$

---

<sup>20</sup>Local means that the phase factor is spacetime dependent

with the corresponding conserved baryon number

$$B = \frac{1}{3} \int d^3x \Psi^\dagger \Psi$$

The [QCD](#) Lagrangian for massless quarks is invariant under  $SU(3)_R \times SU(3)_L$ . For a detailed overview of group theoretical aspects of [QCD](#), see here [45]. Left and right handed states refer to fermionic states that are transformed by the projection operator with eigenvalues  $\pm 1$  into their so called left and right handed state

$$\Psi_{L/R} = P_{L/R} \Psi$$

The  $SU(3)_R \times SU(3)_L$  transformations that act on this projected states read

$$\begin{aligned} \Psi_L &\rightarrow \exp(-i\theta_L \Lambda) \Psi_L \\ \Psi_R &\rightarrow \exp(-i\theta_R \Lambda) \Psi_R \end{aligned}$$

A symmetry under these transformation is called chiral symmetry. In [QCD](#) this symmetry is spontaneously broken. The term “spontaneous” refers to the fact that it is only broken in the vacuum ground state. Instead of “spontaneous” one sometimes also uses the term “hidden” [46]. It leads to a non-mass degeneracy of baryons and their parity partners. We will later see that the [CMF](#) model restores this symmetry by a  $\sigma$  field that dynamically changes the effective masses of the baryons towards degeneracy with their parity partners [47].

#### 1.2.1.1 Asymptotic freedom and Deconfinement

At low energies, quarks and gluons form a bound state due to color confinement. They appear as color neutral states in bound forms of hadrons. Hadrons can either be baryons, which are composed of three quarks  $qqq$  or mesons with a quark - anti-quark pair  $q\bar{q}$ . The interaction strength  $\alpha_s$  between quarks becomes smaller at a large momentum scale which is referred to as a deconfined state where quarks and gluons can move outside hadrons. The reason for this varying coupling between quarks and gluons is the running coupling constant  $\alpha$ . At a low momentum scale thus larger distances  $\alpha$  is increasing and perturbation theory becomes inaccessible. The interaction strength becomes so large that at one point the energy that pulls apart the quarks will create a new quark anti-quark pair. At high momentum scale and thus larger distances  $\alpha$  becomes small. Quarks can move freely and the interaction is weak. This is called asymptotic freedom. Asymptotic freedom makes it possible to use perturbation theory because we have a small parameter around which can be expanded (the [QCD](#) coupling constant).

### 1.2.2 The Bag model

Individual quarks have not been observed to date, although a theoretical framework has already been developed since the late 60's to describe deconfined quarks and gluons. The first formulation of a Bag model came from Bogoliubov who build a theory where three massless quarks inside a spherical volume with radius  $R$  are bound in an infinite square well potential [48]. The Bag model is a phenomenological model that describes both confinement and asymptotic freedom. An important property of confined matter is that it can not be accessed by perturbative methods such as in QED because the coupling constant  $\alpha_s$  becomes very large at low energies. Low energy means that the momentum exchange  $Q^2$  is small and therefore leads to a low resolution and larger distances. Treating the interaction of quarks and gluons as a small perturbation in this energy regime would contradict the physical nature. The bag model phenomenologically assumes that hadrons are embedded into a "non-perturbative" QCD vacuum (also called normal QCD vacuum) and considered as "bags" inside which quarks and gluons are confined. So to say, there are two regions [49, 50]

- Interior of bag: masses of quarks are low and interaction is weak
- Exterior of bag: quark and gluon condensate

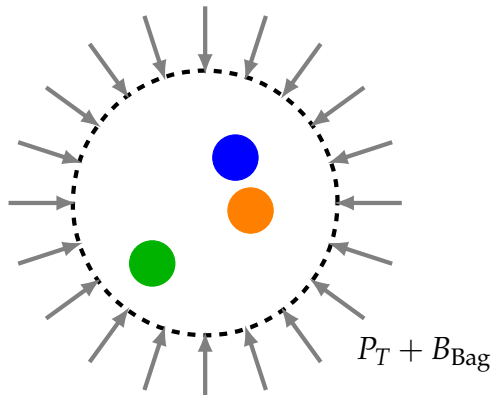


Figure 7: A positive non-zero vacuum pressure  $B_{\text{Bag}}$  confines quarks inside the bag. Additional particles outside the bag (like mesons as for the vector interaction Bag model (vMIT)) can increase the outwards pressure (here indicated by  $P_T$ ).

Outside of the bag there is a constant positive potential energy  $B$  which enters as the bag constant in further calculations. It is the difference of energy density between the vacuum and bag energy  $\epsilon_{\text{bag}} - \epsilon_{\text{vac}} > 0$ . The surface of the bag

has boundary conditions such that the perpendicular quark current is zero. This enforces confinement. For the Quark Gluon plasma in this model, the standard [Massachusetts Inst. of Technology \(MIT\)](#) Bag Model (see here the original paper: [49]) with **massless** and **non interacting** quarks is used with its simple Lagrangian in its most general form [51, 52].

$$\mathcal{L} = \sum_q \frac{i}{2} [\bar{\Psi}_q(x) \gamma^\mu \partial_\mu \Psi_q(x) - B] \theta_V(p) - \frac{1}{2} \bar{\Psi}_q(x) \Psi_q(x) \delta_S(p) \quad (37)$$

where  $\theta_V$  is the heaviside step function and  $x = (\vec{r}, t)$  and  $p \equiv |\vec{r}| - R_{\text{surface}}$

$$\theta_V(p) = \begin{cases} 1 & \text{inside bag} \\ 0 & \text{otherwise} \end{cases} \quad (38)$$

$\delta_S(p)$  is the delta distribution that contributes only to the Lagrange density  $\mathcal{L}$  at the bag surface:

$$\delta_S(p) = \begin{cases} \infty & \text{at bag surface} \\ 0 & \text{otherwise} \end{cases} \quad (39)$$

The index  $q$  indicates the summation over the different quark flavors.  $\bar{\Psi}$  is the Dirac adjoint  $\gamma^\mu \Psi^\dagger$  and  $\Psi^\dagger$  the Hermitian adjoint of the wave function. One obtains the equations of motion by applying the Euler Lagrange equation for each  $\Psi$  and its adjoint.

The free Dirac equation for massless particles **inside the bag** is then simply given by

$$i\gamma^\mu \partial_\mu \Psi = 0$$

The boundaries on the **surface of the Bag** for  $|\vec{r}| = R_{\text{surface}}$  yield

$$\Psi = i\gamma^\mu \eta_\mu \Psi \quad (40)$$

$$\bar{\Psi} = -i\gamma^\mu \eta_\mu \bar{\Psi} \quad (41)$$

$\eta_\mu$  is normal to the surface  $S$ . These two boundary conditions ensure that the normal quark current  $\eta_\mu j^\mu$  vanishes on the surface. The boundaries provide confinement of the quarks so they can not propagate outwards. A full derivation of the equations can be read in Ref. [53].

The next step is derive the boundary condition for the Bag constant. In order to fulfill the conservation of the energy momentum tensor  $\partial_\mu T^{\mu\nu} = 0$  in this

model, the Bag constant must be equal the particle pressure inside an infinitely deep spherical well<sup>21</sup> [54, 55].

$$P = -\frac{1}{2} \frac{d}{dr} (\bar{\Psi} \Psi)$$

At the surface this reduces to

$$B = -\frac{1}{2} \eta_\mu \partial^\mu (\bar{\Psi} \Psi) \quad (42)$$

The Bag pressure with a negative sign  $-B$  in the Lagrangian in eq. 37 has to be equal the vacuum pressure at the surface. This ensures energy and momentum conservation.  $B$  has the units MeV<sup>4</sup> often but one uses  $B^{1/4}$  for convenience.

### 1.2.3 Standard MIT bag model

I will now introduce the Standard MIT Bag model. The probability distribution of fermions and bosons to be located at an energy state  $E$  is described by the Fermi-Dirac and Bose-Einstein statistics

$$f_{\text{Fermi-Dirac/Bose-Einstein}} = \frac{1}{1 \pm e^{(E-\mu_f)/T}} \quad (43)$$

with the relativistic energy momentum relation  $E = \sqrt{k^2 + m^2}$ . The grand canonical partition function with fixed volume  $V$ , temperature  $T$  and chemical potential  $\mu$  for fermions and bosons is obtained by integrating over all possible momentum states  $k = \hbar p$  inside the unit volume. Using the logarithm of the partition function simplifies subsequent calculations

$$\ln \mathcal{Z} = \frac{V}{(2\pi)^3} \int d^3 k \ln \left( 1 \pm e^{-(E_k \pm \mu)/T} \right) \quad (44)$$

The lower sign in the integral stands for fermions and bosons respectively. The sign in the exponent is for particles and antiparticles respectively. At  $T = 0$ , Bosons from Borse-Einstein condensate and do not contribute to the pressure. I will therefore only consider Fermions from now on. We now calculate, at  $T = 0$ , the thermodynamic quantities  $p, n, s$  via the known thermodynamic relations

$$p = T \frac{\partial \ln \mathcal{Z}}{\partial V}, \quad (45)$$

---

<sup>21</sup>spherical means that the normal component projected onto the four divergence becomes a derivative of only the radial component

$$n = \frac{T}{V} \frac{\partial \ln \mathcal{Z}}{\partial \mu}, \quad (46)$$

$$s = \frac{1}{V} \frac{\partial(T \ln \mathcal{Z})}{\partial T}, \quad (47)$$

$$\epsilon = -p + Ts + \mu n \quad (48)$$

For a non-interacting gas of fermions, eq. 44 can be evaluated further [56]

$$\ln \mathcal{Z}_f(T, \mu_f) = \frac{V}{2\nu_f \pi^2} \int_0^\infty dk \left\{ k^2 \ln \left[ 1 + e^{-(E_f(k) - \mu_f)/T} \right] + \ln \left[ 1 + e^{-(E_f(k) + \mu_f)/T} \right] \right\} \quad (49)$$

$\mathcal{Z}_f$ ,  $\nu_f$ ,  $m_f$  are partition functions, degeneracy factors and mass for fermions, respectively. The two terms in the partition function for fermions are the particle and anti-particle contributions. The integral can be evaluated analytically in the limit of massless particles,  $m_f \rightarrow 0$  [57]

$$T \ln \mathcal{Z}_f = \frac{\nu_f V}{12} \left( \frac{7}{30} \pi^2 T^4 + T^2 \mu_f^2 + \frac{1}{2\pi^2} \mu_f^4 \right) \quad (50)$$

It is now straightforward to obtain the thermodynamic quantities of eq. 45 to eq. 48 by taking the partial derivatives of eq. 50. We have for pressure  $p$ , number density  $n$  and entropy  $s$  for our massless Bag model with degeneracy factor  $\nu_f$ :

$$P = \frac{\nu_f}{24\pi^2} \left[ \frac{7}{15} \pi^4 T^4 + 2\pi^2 \mu_f^2 T^2 + \mu_f^4 \right] \quad (51)$$

$$n = \frac{\nu_f}{6\pi^2} \left[ \pi^2 \mu_f T^2 + \mu_f^3 \right] \quad (52)$$

$$s = \frac{\nu_f}{6\pi^2} \left[ \pi^2 \mu_f^2 T + \frac{7}{15} \pi^4 T^3 \right] \quad (53)$$

### 1.2.3.1 Particle compositions

The number of quark flavors determines the degeneracy factor  $\nu_f$  and  $\nu_b$ . Neutrons dominate NS matter and are composed of three quarks  $n = (u, d, d)$  so that one can approximately relate baryon and quark chemical potential by the factor 1/3 (Where  $\mu_q = \sum_{u,d,s} \mu_{q_i}$ ).

$$\mu_q = \frac{1}{3} \mu_B \quad (54)$$

The baryon chemical potential above the energy at which the Maxwell construction takes place is described in terms of quark chemical potential where we have  $\mu_f \equiv \mu_B^{\text{hadr}} = 3\mu_q^{\text{QGP}}$ <sup>22</sup>. Chemical equilibrium of quark flavours and leptons eliminate degrees of freedoms for the possible particle compositions. In NS matter we have for beta equilibrium the relations [58]

$$\begin{aligned}\mu^d &= \mu^u + \mu^e \\ \mu^d &= \mu^s\end{aligned}$$

### 1.2.3.2 Two flavors (up and down quarks)

We will now look at the two flavor MIT Bag model. We assume zero masses of  $u$  and  $d$  quarks and an infinite massive strange quark (so that its appearance is suppressed). Gluons come in eight colors and two polarizations so that  $\nu_b = 16$ . Quarks have three colour degrees of freedom and two flavours if we only consider the two lightest quark flavours  $u$  and  $d$  and two spin states. Each of the six flavors (u,d,s,c,b,t) of quarks can have three different “colors” (r,g,b) [56]. The degeneracy factors are chosen such that  $\nu_b \rightarrow \nu_g = 16$  and  $\nu_f \rightarrow \nu_q = 12$ . By summing over the partition functions of all particles we obtain

$$\ln \mathcal{Z}_f = \sum_{f_i} \ln \mathcal{Z}_{f_i} \quad (55)$$

Adding up the partition functions for all particles is equivalent to summing up the partial pressures of the particles (similar for energy density and entropy). One therefore has  $P = P_{\text{gluons}} + P_{\text{quarks}}$  and  $\epsilon = \epsilon_{\text{gluons}} + \epsilon_{\text{quarks}}$  so that we obtain for pressure, energy density, entropy and number density [59]

$$P = \frac{37\pi^2}{90} T^4 + \frac{1}{9} T^2 \mu_q^2 + \frac{1}{162\pi^2} \mu_q^4 \quad (56)$$

$$\epsilon = \frac{37\pi^2}{30} T^4 + \frac{1}{3} T^2 \mu_q^2 + \frac{3}{162\pi^2} \mu_q^4 \quad (57)$$

$$s = \frac{74}{45} \pi^2 T^3 + \frac{1}{9} \pi^2 T \quad (58)$$

$$n = 2 \left( \mu T^2 + \frac{\mu_q^3}{\pi^2} \right) \quad (59)$$

---

<sup>22</sup>This still conserves the condition for the Maxwell construction where  $\mu_{\text{crit}}^{\text{hadr}} = \mu_{\text{crit}}^{\text{QGP}}$ . I formulate everything in terms of  $\mu_B$  therefore eq. 51 from now on carries a factor of 1/3 in  $\mu$ .

To make the prefactors as compact as possible from now on I define the constant

$$a_3 \equiv \frac{\nu_{u,d}}{3^4 \cdot 24\pi^2} = \frac{1}{162\pi^2} \quad (60)$$

The factor in the nominator  $\nu_{u,d} = 12$  arises from the degeneracy of 2 flavors  $\times$  2 spin states  $\times$  3 colors.

#### 1.2.3.3 Three flavors (up, down and strange quarks)

We now consider massless  $u$ ,  $d$  and  $s$  quarks,  $m_u = m_d = m_s = 0$ , for the three flavors Bag model. The strange quark with its mass of  $\sim 100$  MeV is much heavier than its light companions so that setting its mass to zero is a crude approximation that one has to keep in mind. The degeneracy factors change to  $\nu_f = 2 \cdot 3 \cdot 3$  (spin  $\times$  color  $\times$  flavor) by a factor 1.5. The equations for pressure and energy density read

$$P = \frac{37\pi^2}{90} T^4 + \frac{1}{6} T^2 \mu_q^2 + \frac{1.5}{162\pi^2} \mu_q^4 \quad (61)$$

$$\epsilon = \frac{37\pi^2}{30} T^4 + \frac{1}{2} T^2 \mu_q^2 + \frac{4.5}{162\pi^2} \mu_q^4 \quad (62)$$

The amount of flavors will have an impact on Twin star solution, I will discuss this in detail in section [2.3.1](#) and [2.3.2](#).

#### 1.2.3.4 Quark Gluon Plasma

The Bag pressure **outside** the bag contributes to a positive vacuum pressure  $P_{vac} = +B$  and a negative energy density  $\epsilon_{vac} = -B$ . From the stability condition inside the Bag follows a positive energy contribution  $\epsilon_{bag} = B$  and a negative pressure contribution  $P_{bag} = -B$ . We saw in the previous chapter that these relations of pressure and energy inside and outside the bag ensure energy momentum conservation. So adding the contributions of  $B$  we finally obtain for the Quark-Gluon Plasma **inside** the bag

$$P_{QGP} = \frac{37\pi^2}{90} T^4 + \frac{1}{9} T^2 \mu_q^2 + \frac{\text{flavor} \times a_3}{162\pi^2} \mu_q^4 - B \quad (63)$$

$$\epsilon_{QGP} = \frac{37\pi^2}{30} T^4 + \frac{1}{3} T^2 \mu_q^2 + \frac{3 \times \text{flavor} \times a_3}{162\pi^2} \mu_q^4 + B \quad (64)$$

It is possible to calculate the bag constant by using results from [lQCD](#). To do so, one uses the pseudocritical temperature  $T_p = 156.6 \pm 1.5$  MeV that had been measured in lattice calculations [60] and fits it to the relations in eq. 63. A value of the bag constant is  $B^{1/4} \approx 236$  MeV, the baryonic chemical potential  $\mu_B$  at the pseudocritical point is approximately 1594 MeV [56]. Fig. 8 shows a phase diagram where temperature is plotted as function of baryon chemical potential in units of the critical temperature. The broad green band comes from lattice calculations and the black line is MIT Bag model curve.

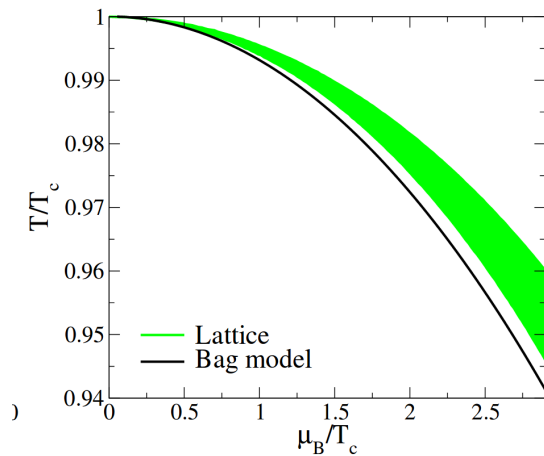


Figure 8: Phase diagram of lattice calculations and the MIT bag model for  $B = 236$  MeV [56]. The green area is the error of the lattice calculations. Qualitatively, the MIT Bag model gives similar results but does not lie within the (green) shaded area.

#### 1.2.4 Vector-interaction-enhanced Bag model

The original MIT bag model does not describe chiral symmetry effects. The phenomenological [vMIT](#) Bag model includes chiral symmetry breaking and repulsive vector repulsion [61] in its Lagrangian. It has been discussed with respect to constraints from [lQCD](#) [62, 63] and the two solar mass constraint from observational astrophysics [64, 44, 65]. In case of a Hybrid star, i.e. stars with a quark core, the two solar mass constraint requires a very stiff quark [EoS](#). There are precise Shapiro time delay measurements that observed high [NS](#) masses<sup>23</sup>.

<sup>23</sup>pulsars PSR J0740+6620 ( $2.17_{-0.10}^{+0.11} M_\odot$ ) [7] and PSR J0348+0432 ( $2.01 \pm 0.04 M_\odot$ ) [66] and recently PSR J0348+0432 ( $2.27_{-0.15}^{+0.17} M_\odot$ ) [67]

The **vMIT** Bag model is an attempt to describe such a stiff quark **EoS**. It has an additional term that describes repulsive vector interactions coming from a non-vanishing mean field in the vector meson interaction channel. From a **lQCD** motivated side, a high repulsion strength contradicts lattice results which I will discuss later. The Lagrangian for the **vMIT** Bag model reads

$$\mathcal{L} = \sum_q \frac{i}{2} \left[ \bar{\Psi}_q(x) \gamma^\mu \partial_\mu \Psi_q(x) - g_q^{(\omega)} \gamma^\mu V_\mu^{(\omega)} - m_q - B \right] \theta_V(p) \quad (65)$$

$$- \frac{1}{2} \bar{\Psi}_q(x) \Psi_q(x) \delta_S(p) \quad (66)$$

$$+ \sum_l \bar{\Psi}(x)_l \gamma^\mu [i\partial_\mu - m_l] \Psi_l(x) \quad (67)$$

It has the same form as the Lagrangian in eq. 37 except that the quarks have non-vanishing masses and also we consider leptons, see the last term in eq. 67. One sums over the contributions of up, down and strange quarks and in the second sum over  $e^-$  and  $\mu^-$  leptons. The vector potential  $V_\mu^{(\omega)}$  describes the interaction of quarks with the  $\omega$  vector isoscalar meson<sup>24</sup>. No  $\rho$  mesons are taken into account.

$$V_\omega^\mu = g_\omega \omega \quad (68)$$

The modified quark chemical potential at  $T = 0$  reads

$$\mu_q^* = \sqrt{k^2 + m_q^2} + g_V V \quad (69)$$

with the momentum vector  $k$  and the bare quark masses. The  $\omega$ -field suppresses hadronic abundances. A repulsive quark coupling changes the thermodynamic properties of dense matter and thus requires the investigation of possible contradictions to results from **lQCD**. This has been studied in the past by comparing model and **lQCD** Baryon number susceptibilities. It has been shown that even a small quark vector coupling leads to a significant deviation of the baryon number susceptibilities [63, 62]. The quark repulsion needs to be chosen near-zero in order to be consistent with **lQCD**.

### 1.2.5 Chiral mean field model (CMF)

The Chiral  $SU(3)$ -flavor parity-doublet Polyakov-loop quark-hadron mean-field model describes hadrons and quarks that interact via meson exchange. The

---

<sup>24</sup>Mesons are composed of a quark, anti-quark pair

effective masses of the particles are generated by their interaction with hadrons<sup>25</sup> and as the baryon density  $\rho$  increases the baryon octet masses degenerate with respect to their parity partner. This restores chiral symmetry [68]. The hadronic phase describes a dilute gas of hadrons. Their masses are chosen such that they obey correct vacuum properties like saturation density, binding energy, incompressibility and symmetry energy, see table 1 and [69]. There are two crossovers, the chiral symmetry restoration where the baryons get degenerate with respect to their parity partners and deconfinement.

I will now give a brief overview over the particle population and the different terms in the CMF Lagrangian. The scalar  $\sigma$  meson is responsible for the attraction among baryons. The vector mesons  $\omega$ ,  $\rho$  and  $\Phi$  mesons have a repulsive coupling and therefore lead to a stiffer EoS. The Lagrangian reads

$$\mathcal{L} = \mathcal{L}_{kin} + \mathcal{L}_{int} + \mathcal{L}_{meson} + \mathcal{L}_{SB} - U \quad (70)$$

$\mathcal{L}_{kin}$  is the kinetic energy term for free particles, including the Dirac, Klein-Gordon and Procca equation for fermions, scalar and vector mesons respectively.  $\mathcal{L}_{int}$  is the interaction term between baryons<sup>26</sup> and vector-  $\omega$ - and scalar  $\phi$ -mesons. The scalar-isovector  $\rho$ - meson is important as it is related to the isospin asymmetry that is relevant for NS matter where the amount of neutrons is much larger than the amount of protons [71, 72, 14].

$$\mathcal{L}_{int} = - \sum_i \bar{\Psi}_i [\gamma_0(g_{i\omega}\omega + g_{i\rho}\rho + g_{i\phi}\phi) + m_i^*] \Psi_i \quad (71)$$

$g_{i\omega}$ ,  $g_{i\rho}$  and  $g_{i\phi}$  are the coupling constants of the baryon octet to the  $\omega$ ,  $\rho$  and (hidden strange)  $\phi$  field [69]. The third term  $\mathcal{L}_{meson}$  is the self interaction term for the spin-0 and spin-1 meson fields

$$\mathcal{L}_{meson} = -\frac{1}{2} (m_\omega^2 \omega^2 + m_\phi^2 \phi^2 + m_\rho^2 \rho^2) \quad (72)$$

$$- g_4 \left( \omega^4 + \frac{\phi^4}{4} + 3\omega^2\phi^2 + 3\omega^2\rho^2 + \frac{4\omega^3\phi}{\sqrt{2}} + \frac{2\omega\phi^3}{\sqrt{2}} + \frac{3\rho^2\phi^2}{2} \right) \quad (73)$$

$$+ \frac{1}{2} k_0 (\sigma^2 + \zeta^2) - k_1 (\sigma^2 + \zeta^2)^2 \quad (74)$$

$$- k_2 \left( \frac{\sigma^4}{2} + \zeta^4 \right) + k_6 (\sigma^6 + 4\zeta^6) \quad (75)$$

---

<sup>25</sup>The meson fields are formulated within a mean field approach

<sup>26</sup>the index  $i$  stands for particles of the Baryon Octet [70]

$\mathcal{L}_{SB}$  is an explicit symmetry breaking term.

$$\mathcal{L}_{SB} = m_\pi^2 f_\pi \sigma + \left( 2\sqrt{2}m_k^2 f_k - \frac{1}{\sqrt{2}}m_\pi^2 f_\pi \right) \zeta \quad (76)$$

The baryon masses are dynamically generated by their couplings to the scalar  $\sigma$  and strange  $\zeta$  field. These two fields are order parameters for the chiral transition and directly affect the effective baryon masses, see eq. 77 and [47]. With increasing density  $\rho_B$ , the  $\sigma$ -field decreases and causes the effective masses of the particles to restore chiral symmetry. The effective masses read

$$m_{i\pm}^* = \sqrt{(g_{\sigma i}^1 \sigma + g_{\zeta i}^1 \zeta)^2 + (m_0 + n_s M_s)^2} \pm g_{\sigma i}^2 \sigma \pm g_{\zeta i}^2 \zeta \quad (77)$$

$m_0$  is an explicit mass term of the baryon octet  $m_0 = 759$  MeV,  $n_s$  is the number of strange quarks in baryons and  $M_s = 130$  MeV is the mass of the strange quark. The signs  $\pm$  indicate the parity state of the particle<sup>27</sup>.  $g_{\sigma i}^1$ ,  $g_{\zeta i}^1$ ,  $g_{\zeta i}^2$  and  $g_{\zeta i}^2$  are  $2 \times i$  different coupling constants, two for each scalar field  $\sigma$  and  $\zeta$  for all  $i$  baryons of the octet.

At high densities, deconfined quarks dominate the phase so that one needs to explicitly formulate a deconfined mechanism to the model. This is done in analogy to the Nambu Jona-Lasinio (PNJL) model [73] which is an Polyakov-loop-extended effective chiral field theory describing the mechanism of spontaneous symmetry breaking. The appearance of quarks is controlled by a temperature dependent Polyakov loop order parameter  $\Phi$  [74, 75]. The Polyakov-loop is controlled by the Polyakov-loop potential  $U$

$$U(T, \Phi, \Phi^*) = -\frac{1}{2}a(T)\Phi\Phi^* + b(T)\log\left[1 - 6\Phi\Phi^* + 4(\Phi^3 + \Phi^{*3}) - 3(\Phi\Phi^*)^2\right] \quad (78)$$

where  $a(T) = a_0 T^4 a_1 T_0 T^3 + a_2 T_0^2 T^2$  and  $b(T) = b_3 T_0^4$  [47].  $\Phi$  is only defined for  $T \neq 0$ . In the framework of my thesis, i.e. in the specific case of NSs, it is set to one. The grand canonical potential<sup>28</sup> in which the Polyakov loop enters, is for quarks/anti-quarks expressed as

$$\Omega_q = -T \sum_{i=u,d,s} \frac{\nu_i}{(2\pi)^3} \int d^3 k \left\{ 1 + \Phi \ln \left( 1 + e^{-(E_i^* - \mu_i^*)/T} \right) \right\} \quad (79)$$

---

<sup>27</sup>More specifically, it is the eigenvalue of the parity projector  $P_\pm$  with eigenvalues  $\pm 1$

<sup>28</sup>The grand canonical potential is related to the partition function which I introduced in eq. 44:  $\Omega = -T \ln Z$

$$\Omega_{\bar{q}} = -T \sum_{i=u,d,s} \frac{\nu_i}{(2\pi)^3} \int d^3 k \left\{ 1 + \Phi^* \ln \left( 1 + e^{-(E_i^* + \mu_i^*)/T} \right) \right\} \quad (80)$$

$\nu_i$  is the degeneracy factor and  $E_i^* = \sqrt{m_i^* + p^2}$ . The quark masses  $m_i^*$  and quark chemical potential  $\mu_i^*$  are dynamically generated and controlled by the  $\sigma$ -field and  $\chi$ -field. The effective masses for up, down and strange quarks and their chemical potential read

$$m_q^* = -g_{q\sigma}\sigma + \delta m_q + m_{0q} \quad (81)$$

$$m_s^* = -g_{s\zeta}\zeta + \delta m_s + m_{0s} \quad (82)$$

$$\mu_i^* = \mu_i - g_{i\rho}\rho - g_{i\phi}\phi \quad (83)$$

As one can see the  $\sigma$ -meson is the generating field for up and down quarks. The  $\zeta$ -meson leads to dynamic strange quark masses. The light  $u$  and  $d$  quarks have the explicit ground state mass term  $\delta m_u = \delta m_d = 5$  MeV and the heavier strange quark has a mass  $\delta_s = 150$  MeV and  $m_{0q} = 235$  MeV. To suppress quarks at nuclear ground state additional mass terms  $m_{0q}$  and  $m_{0s}$  are added to the effective masses. The chemical potential for all three quark flavors is affected by the couplings to the vector  $\omega$  and  $\phi$  fields. An explicit volume term  $v_B$  is added to the baryons and quarks to suppress hadrons in the quark phase

$$v_B = v$$

$$v_M = v/a$$

$v_M$  is the meson volume term and  $a$  a positive real number larger than 1 [71]. The modified baryon chemical potential then reads  $\tilde{\mu}_B = \mu_B - v_B \cdot P$ . So to say as soon as quarks contribute to the pressure  $P$ , they suppress hadrons by lowering their chemical potential.

$\rho_0$	$0.14 \pm 0.02 \text{ fm}^{-3}$
$E_{\text{bind}}/\text{nucleon}$	$16.6 \pm 0.8 \text{ MeV}$
Compressibility $K_0$	$269 \pm 54 \text{ MeV}$
$E_{\text{asym}}$	$30 \pm 6 \text{ MeV}$

Table 1: Saturation properties

Fig. 9 shows the EoS (dashed red line) for the crust. I used a zero temperature model for white dwarfs with coulomb interacting matter consisting of electrons and neutrons. For more details see here [76]. The green line is the CMF EoS.

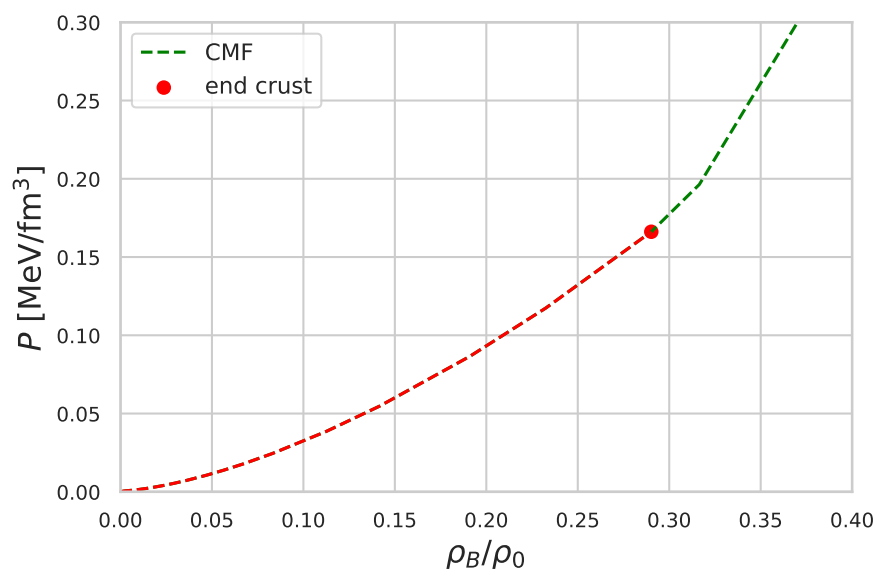


Figure 9: Pressure as function of central density. The dashed red line is the crust-[EoS](#) for low densities. This low density regime [EoS](#) is fitted to the [CMF EoS](#) (red) at  $\sim 0.3\rho_0$ .

# 2

## RESULTS

---

### 2.1 NUMERICAL IMPLEMENTATION

The Love number  $k_2$  can be obtained numerically by solving the coupled first order implicit differential eq. 26- 29 in each step of the TOV solver. I solve for pressure, mass and the two variables  $H$  and  $\beta$  from eq. 26, 28, using a 4<sup>th</sup> order Runge Kutta method. The input table from the EoS lists energy density for every  $P$  but as we relate pressure and energy density to the radius, one needs to interpolate between  $p(r_i)$  and  $p(r_{i+1})$  in each Runge Kutta step (the index  $i$  refers to the i'th table entry) in order to find the corresponding  $\epsilon$ . The simplest interpolation scheme is a linear interpolation between  $p(r_i)$  and  $p(r_{i+1})$  in order to find the corresponding value for  $\epsilon$  from the table. One can also do a function fit  $\epsilon(r)$  that returns the right value for the energy density at a given evaluated pressure  $P(r_i)$ . For this thesis it turned out to be sufficient to do a linear interpolation. The Runge Kutta method evaluates the differential equation at four different points so that for each step, one needs to obtain the corresponding  $\epsilon(r)$ . The 4 coupled implicit differential equations read

$$\frac{dP}{dr} = -\frac{G\epsilon(r)m(r)}{r^2} \left[ 1 + \frac{p(r)}{\epsilon(r)} \right] \left[ 1 + \frac{4\pi r^3 p(r)}{m(r)} \right] \left[ 1 - \frac{2m(r)}{r} \right]^{-1} \quad (84)$$

$$\frac{dm}{dr} = -4\pi\epsilon(r) \quad (85)$$

$$\frac{dH}{dr} = \beta \quad (86)$$

$$\frac{d\beta}{dr} = 2 \left( 1 - 2\frac{m(r)}{r} \right)^{-1} H \left\{ 2\pi \left( 5\epsilon(r) + 9p + \frac{d\epsilon(r)}{dp(r)} \right) + \frac{3}{r^2} \right\} \quad (87)$$

$$+ 2 \left( 1 - 2\frac{m(r)}{r^2} \right)^{-1} \left( \frac{m(r)}{r^2} + 4\pi r p(r) \right)^2 \left\{ \frac{2\beta}{r} \left( 1 - 2\frac{m(r)}{r} \right)^{-1} \right. \quad (88)$$

$$\times \left. \left\{ -1 + \frac{m(r)}{r} + 2\pi r^2 (\epsilon - p(r)) \right\} \right\} \quad (89)$$

I obtain masses and radii by solving eq. 84 and eq. 85. With these two structural observables, I obtain the compactness  $C \equiv M/R$  which I need, in order to calculate the  $k_2$  love number (see eq. 31) and dimensionless tidal deformability  $\Lambda$  (see eq. 35). So to speak, I need the compactness and the solution of 86 and 89 in order to calculate  $k_2$  and  $\Lambda$ . The corresponding code is given in listing 2.1

Listing 2.1: M-R Code

```

1 #rungekutta() : Fourth order runge kutta method
2 #interpolate(): linear interpolation
3 #k_2()       : computes Love number k_2
4 #p_0         : smallest initial pressure
5 #p_max       : highest initial pressure
6 #dr          : stepwidth inside star
7 #e           : tiny float > 0
8
9 for p_i in xrange(p_0, p_max):
10    epsilon_i = epsilon_0
11    r = 0
12    do while p_i > e:
13        p_i, m_i, H_i, beta_i = rungekutta(p_i, epsilon_i, r)
14        epsilon_i = interpolate_epsilon(p_i, epsilon_i)
15        r_i += dr
16        y = r_i*beta_i/H_i
17        k_2 = k_2(y, m_i/r_i)
```

## 2.2 INVESTIGATION OF THE CMF-MODEL

In this chapter I present the results from the [CMF](#) and show that no twin star solutions are possible within this framework [47]. I plot and discuss the following relations

1. pressure as function of energy density  $\epsilon$
2. mass  $M/M_\odot$  as function of central density in units of  $\rho_0$ <sup>1</sup>
3. squared speed of sound as function of central density
4. adiabatic index  $\Gamma$  as function of central density
5. dimensionless deformability  $\Lambda$  as function of mass  $M/M_\odot$
6. Mass-Radius relation
7.  $k_2$  Love number as a function of mass
8. solutions of differential equation for tidal deformability  $\Lambda$ ,  $y$ ,  $H$  and  $\beta$  as a function of the radius

The color bars in each of the following plots show the quark core content in units of baryon density  $\rho_B^{\text{all}}$ . Fig. 10a shows the [EoS](#) for the [CMF](#) model with energy density on the x- and pressure on the y- axis. The subscript  $c$  stands for “core”. The black dashed curve is the causal limit beyond which the speed of sound exceeds the speed of light. The light grey dashed line is the Stefan Boltzmann limit that is  $1/3c$ . The black star represents maximum stable masses. I divide the [EoS](#) in fig. 10a into 5 sections:

- $n \leq 2n_0$ : fluid purely made up of hadrons
- $2n_0 \leq n_B \leq 2.5n_0$ : phase crossover from a hadron resonance gas to stiff hadronic liquid
- $2.5n_0 \leq n_B \leq 2.7n_0$ : Effective masses of baryon octet and respective parity partners decrease (controlled via the  $\sigma$ -order parameter that affects the effective masses in eq. 77) towards chiral restoration so that the masses of the parity partners become degenerate. It is now energetically more favourable to create new parity partners than to keep increasing the Fermi energy by adding new baryons of the same parity. This is why the pressure shrinks and the [EoS](#) softens.

---

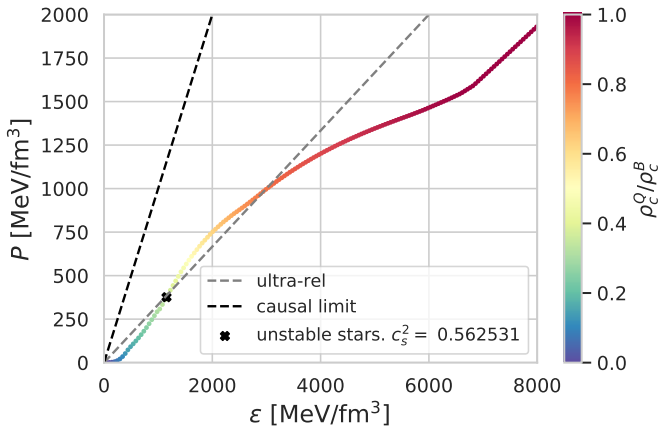
<sup>1</sup>As the baryon particle number is a conversed quantity  $\rho^{\text{all}} = \rho^B$

- $2.7 n_0 \leq n_B \leq 6 n_0$ : Chiral symmetry is restored and repulsion increases again up to a maximum
- $n \geq 6n_0$ : Quarks and gluons dominate the matter. The repulsion among particles is lowered and the curve is converging towards the Stefan Boltzmann limit (grey dashed line).

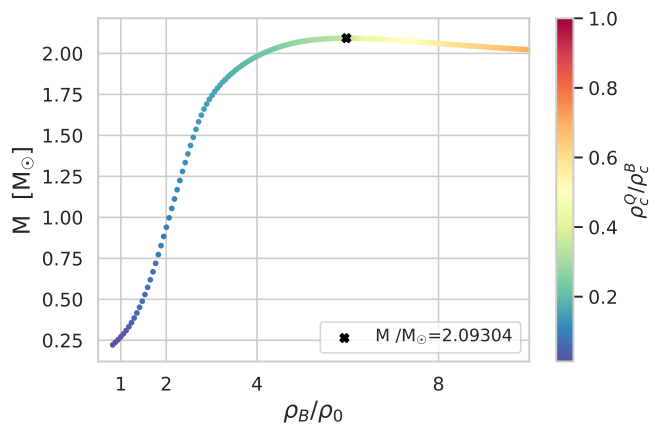
Fig. 10b shows the corresponding masses of the stars as function of central density. The maximum mass is  $\sim 2.1 M_\odot$ . All stellar configurations at the right side of the black star refer to unstable configurations. Compared to fig. 10a, we are in the lower left side where the quark fraction is  $\leq 0.5\rho_B$ . Interestingly, the last stable stellar configuration is where the squared speed of sound is at its global maximum at  $\sim 6\rho_0$ , as one can see in fig. 10c. Stiffness alone therefore is not a sufficient criterion for stable solutions. I plotted the second derivative, the adiabatic index  $\Gamma$ , in fig. 10d. It is defined as

$$\Gamma \equiv \frac{P + \epsilon}{P} v_s^2$$

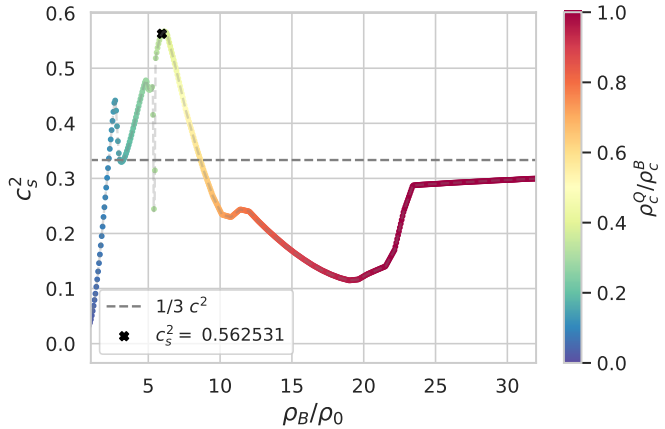
and a measure for the curvature of the EoS [15]. One observes that the last stable star also lies at a maximum, this time a local one. Looking at fig. 10a, we see that right before the black dot, the EoS changes its slope from a left handed curvature into a right handed one. One needs to solve the differential equations  $H$  and  $\beta$  of eq. 26 and eq. 28 in order to calculate the tidal Love number  $k_2$  in fig. 10g and 10h, the tidal deformability  $\Lambda$  (fig. 10e), see eq. 30, 31 and 35. I plotted beta and  $H$  as functions of  $R$  in fig. 10j and 10i. One can see a discontinuity of both functions  $H$  and  $\beta$  just before the unstable branch. This can have numerical reasons and as it appears after the destabilization it might not be correlated to the stellar instability occurring shortly before but one could investigate this further in future studies.



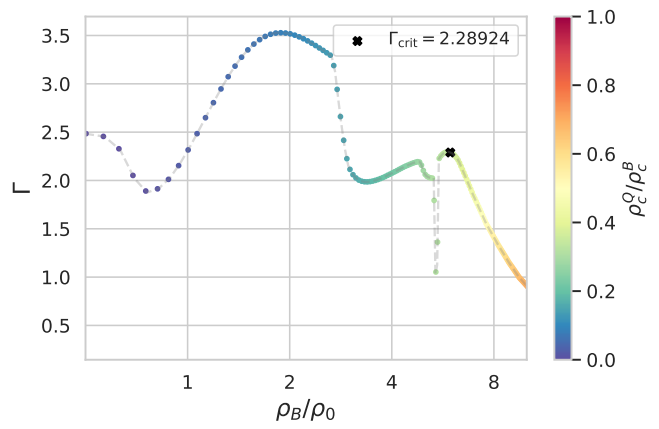
(a) Pressure  $P$  as a function of energy density  $\epsilon$ .



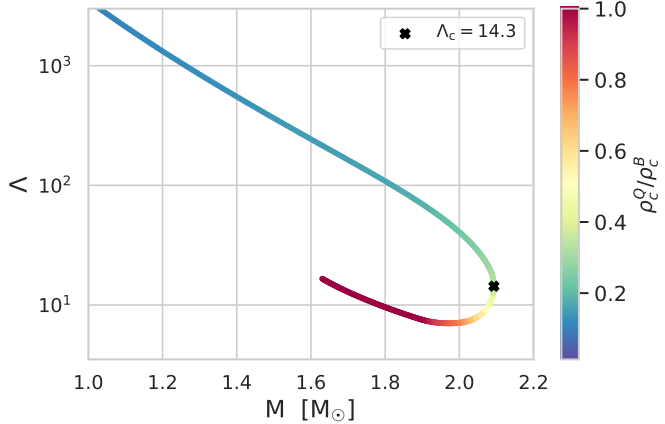
(b) Mass  $M$  as function of  $\rho/\rho_0$



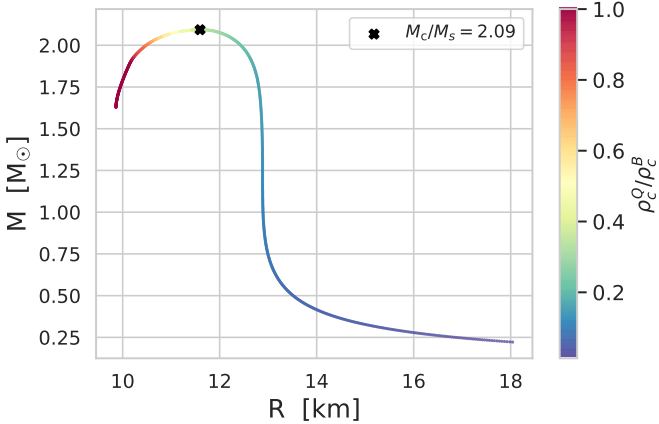
(c)  $c_s^2 [c]$  as function of  $\rho_B/\rho_0$



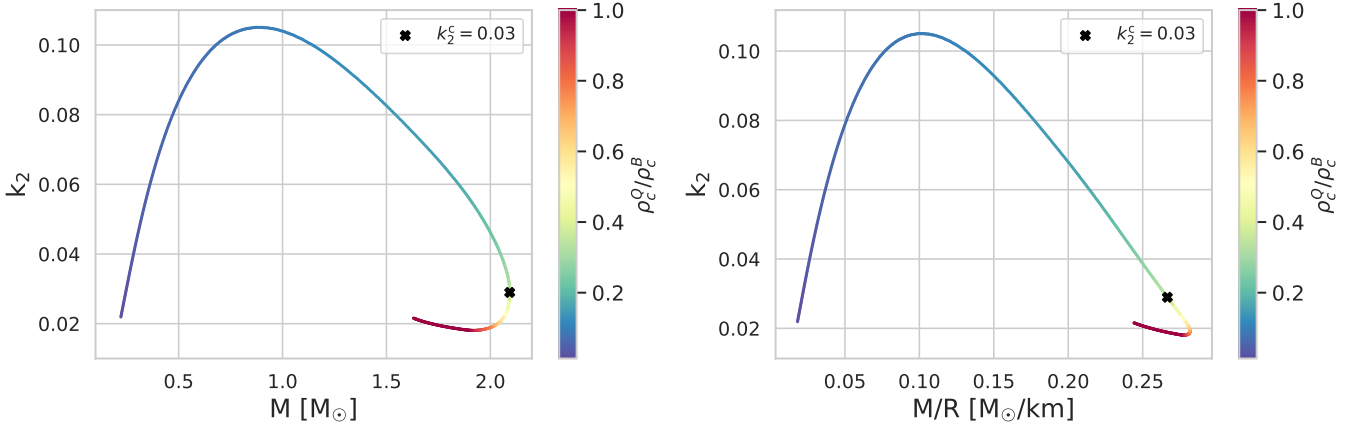
(d) Adiabatic index  $\Gamma$  (dim.less) as function of  $\rho/\rho_0$ .



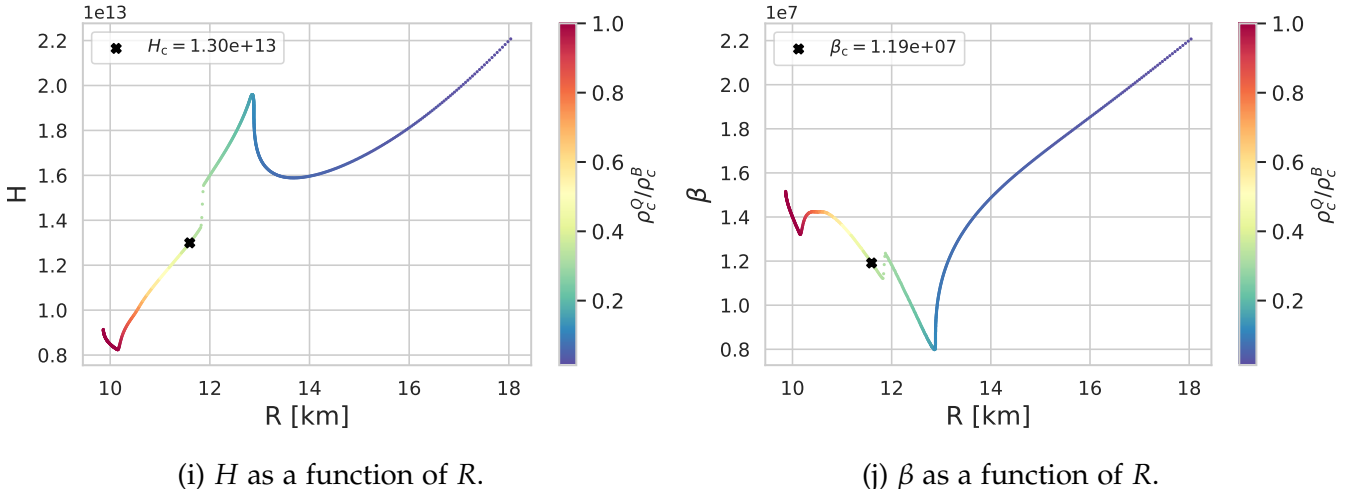
(e) Tidal deformability  $\Lambda$  as a function of mass.



(f) Mass-radius relation



(g) Love number  $k_2$  (in units  $\text{km}^5/M_\odot^5$ ) as function of  $M$ .  
(h) Love number  $k_2$  (in units  $\text{km}^5/M_\odot^5$ ) as function of compactness  $C$ .



(i)  $H$  as a function of  $R$ .

(j)  $\beta$  as a function of  $R$ .

Figure 10: Here we see various plots from the [CMF EoS](#). The colorbar for each plot shows the quark fraction in the [NS](#) core.

[Fig. 10a](#) shows pressure as function of energy density. The relevant part for [NSs](#) is for energy densities  $\leq 2000 \text{ MeVfm}^{-3}$ . At energy densities above  $6000 \text{ MeVfm}^{-3}$  one clearly sees the converging behaviour of the [EoS](#) towards the Stefan-Boltzmann limit. This is where the quarks are deconfined. There black star corresponds to the last stable star configuration of the pure [CMF EoS](#). The [CMF](#) model has a smooth crossover from hadrons to quarks and hybrid stars are stable within this model up to a quark fraction of  $\sim 0.3$ . I discuss the behaviour of the [EoS](#) in detail in the text.

[Fig. 10b](#) shows the mass as function of central density in units of nuclear saturation density  $\rho_0$ . Increasing the central density increases the mass for stellar configurations. All stars that lie on the right side of the black star correspond to unstable configurations. I discussed this in detail in section [1.1.3](#). The maximum mass has a central density of about  $\rho/\rho_0 \sim 6$ .

Fig. 10c shows the speed of sound as function of central density. The last stable star occurs at the maximum stiffness. The grey red line is the lQCD limit of 1/3. It is interesting that an unstable branch occurs if the EoS is maximally stiff. The speed of sound at this point is  $\sim c/2$ . At this point, the star should still be able to support high masses because stiff means that the pressure rises strongly with increasing densities. It clearly shows that stiffness alone is not a sufficient criterion alone for high mass support.

In Fig. 10d I plot the adiabatic index as function of central density.  $\Gamma$  has a local maximum that corresponds to the onset of the unstable branch and the global maximum of fig. 10c.

In fig. 10e I plot the dimensionless tidal deformability as function of mass. Clearly visible,  $\Lambda$  decreases with increasing masses. If one follows the “blue to yellow” line, it corresponds to the stable branch in fig. 10f. When  $M_{\text{star}} = M_{\text{max}}$  the curve “turns” to the left into high quark fraction regions and from then on the branch is unstable. Fig. 10f shows mass as function of radius.

Fig. 10g shows the  $k_2$  love number as function of mass. The  $k_2$  love number is, compared to the tidal deformability  $\Lambda$ , very sensitive to the compactness of stars. Instead of monotonically decreasing up to the unstable point as one observes in fig. 10e,  $k_2$  has a clear maximum at about  $1M_{\odot}$ . The unstable branch (black star) at the far most right point of the plot before the line curve left again. Fig. 10h shows as well  $k_2$  but as function of compactness instead of mass. From this and the previous plot 10g one can conclude that the maximum mass of a M-R relation does not correspond to the most compact star, since in this curve unstable stars right of the black star have higher compactness. This means that the decrease in radius is higher than the decrease in mass (so that C increases), see the also M-R relation in fig. 10f.

Fig. 10i and fig. 10j are the differential equations of eq. 26 and eq. 28, as function of radii (these plots do not show the differential equation itself but one point of it, evaluated at the surface  $R$  of the star. These two plots are the only ones showing a clear numerical instability around the maximum (with maximum I refer to the maximum in the M-R relation).

Fig. 11a shows the particle composition as function of baryon density in units of nuclear saturation density  $\rho_0$ . Fig. 11b shows the sigma field that is an order parameter for the chiral restoration. By decreasing  $\sigma$  the baryon octet masses degenerate with their parity partners (see eq. 81) and chiral symmetry is restored. This happened at about  $\rho = 4\rho_0$ . In the plot the amount parity partners  $n^*$  and  $p^*$  increase when chiral symmetry is restored. The second order parameter from the CMF model is the Polyakov loop. Within the framework of this thesis it is set to one for cold NS matter.

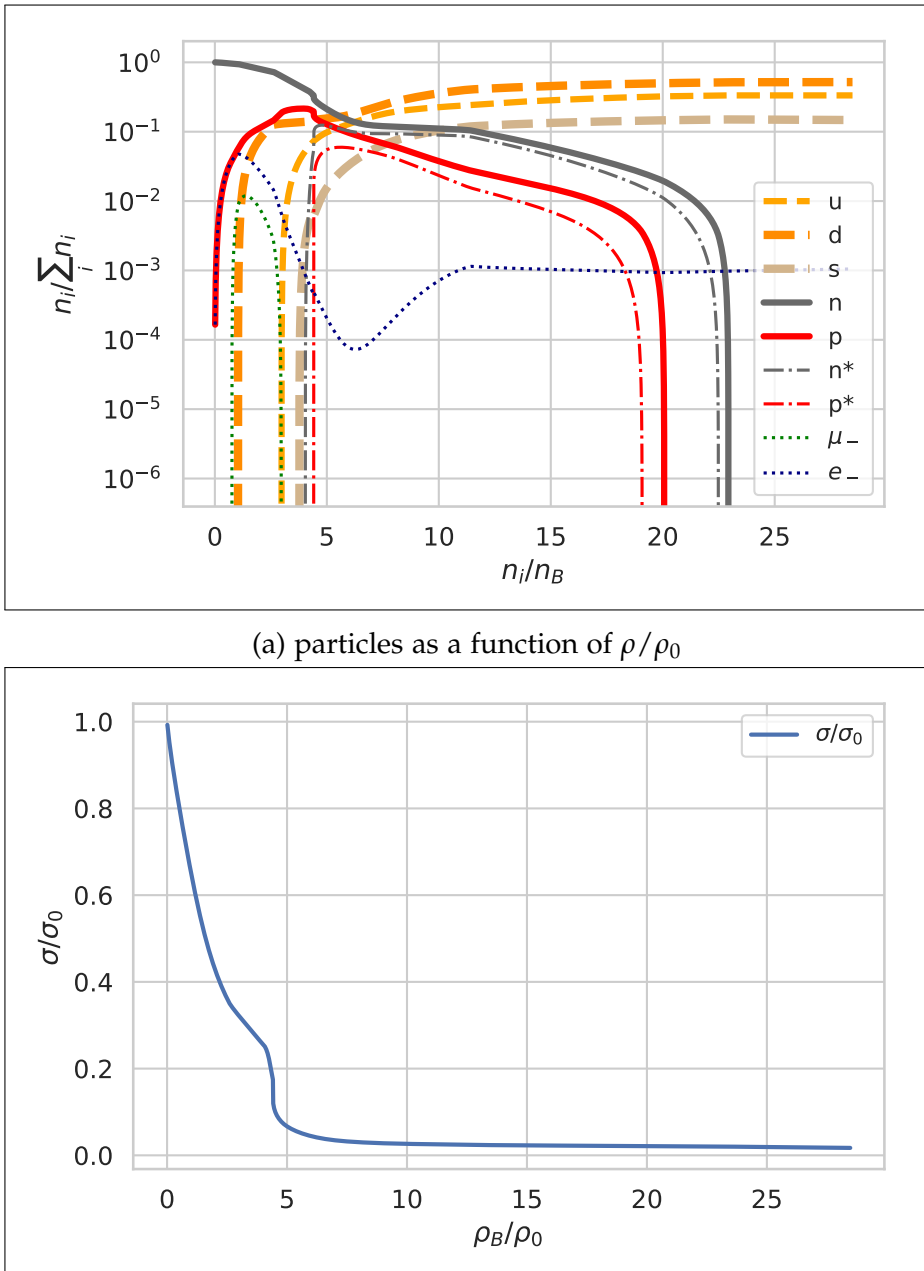


Figure 11: **Top:** Different particles as function of density  $\rho/\rho_0$ . Protons and neutrons dominate the star below  $5\rho/\rho_0$  but their density decreases. Quarks appear at  $\approx 0.75\rho/\rho_0$ . The parity partners of  $n$  and  $p$  appear when the sigma field reduces dramatically (see right plot) at about  $4\rho/\rho_0$ . **Bottom:**  $\sigma$  field as function of  $\rho/\rho_0$ . It monotonically decreases. It is easy to spot the chiral restoration where parity partners appear in the left plot.

### 2.2.0.1 Comparison to GW170817

**Artificial Intelligence (AI)** has become a powerful tool to investigate parameter spaces in an efficient way. In astronomy it is as well widely used to determine for example **EoS** with these methods. In a recent published paper, Fujimoto et al. trained a neural network with observational input data to predict an **EoS** [77]. They constructed a four layer neural network to output the most likely **EoS**, given 14 measurements of masses<sup>2</sup> and radii with values that lie within the  $1\sigma$  range. The neural network returned five  $(P, \rho)$  coordinates. The shaded area in fig. 12a shows the most likely tidal deformability given the training data. The blue line is the pure **CMF**-model curve. The red bar is the GW170817 observation. The blue shaded speed of sound in fig. 12b topologically covers most of the area of the blue **CMF** - curve. **AI** is one option to invert the **TOV**

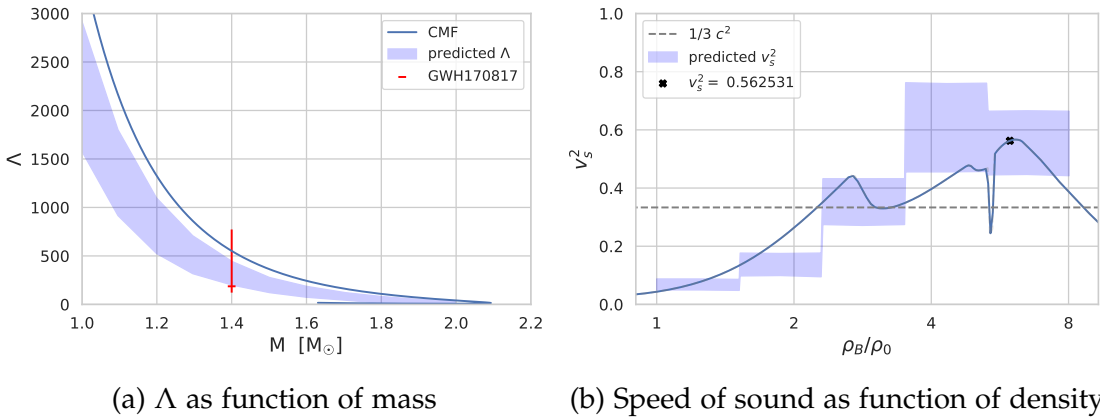


Figure 12: **Left:** Tidal deformability  $\Lambda$  as function of mass. The blue shaded area is what [77] predicted. The blue line is the tidal deformability as calculated from the **CMF** model. The red bar is the tidal deformability as measured from GW170817. **Right:** Speed of sound as function of density. Predicted output (shaded area) and **CMF** model lie within a similar range. The dashed grey line is the Stefan Boltzmann limit of  $1/3$ . The black star at  $\sim 8\rho/\rho_0$  is the maximum mass of the **CMF EoS** and the speed of sound  $v_s^2$  in this region is around one half the speed of light.

solver and, based on observational input data, extract the **EoS** in a probabilistic manner (meaning that one obtains probabilities how likely a certain **EoS** is normalized to all solutions of the neural network). The neural networks learns from observations when when mass and corresponding radius are known. Mathematically, it finds a inverse map  $\Psi_{\text{TOV}}^{-1}$  to the **TOV** that maps the curve

<sup>2</sup>The data is free available under [xtreme.as.arizona.edu/NeutronStars/](http://xtreme.as.arizona.edu/NeutronStars/)

$(\rho(p), p)$  onto the curve  $(M(p_c), R(p_c))$  [78]. Fujimoto et al. created training data by using many different EoS and calculated their corresponding M-R relation curves with the TOV solver. With this training data the network was able to “learn” an inverse mapping  $\text{TOV} \rightarrow \text{EoS}$  and then predict the most likely EoS, based on the observational data.

- The training data is biased in a way, since it relies on general relativity. The goal was to find the inverse mapping  $\Psi_{\text{TOV}}^{-1}$  so of course, the outputted EoS is based on the assumption that general relativity is the correct and only contributing theory for TOV-stars.
- Deep neural networks have many layers with neurons so that the few data points can rapidly be overfitted by the huge amount of parameters from the neural network.

It is possible to create EoS that are only constrained by first-principles hadron theory that includes hadron physics at lower densities and high density perturbative QCD. One can “brute-force” cover the whole parameter space of possible connections in the  $(p, \rho)$  plane by connecting both experimental results and calculate all possible paths that lie in between, see fig. 13. The only constraint in this approach is causality [79].

### 2.3 STANDARD MIT BAG MODEL

In the following I present the procedure for calculating the combined CMF and bag model EoS. The CMF model is a sophisticated temperature and density dependent model however it does not produce twin star solutions. Twin stars, if they existed, are interesting because they could prove the existence of a new phase in the second branch [80]. A crossover to a deconfined phase may not be strong enough to destabilize the star. By adding a Maxwell construction one can artificially insert a latent heat. Even though such a new EoS may violate constraints from lQCD, it is useful in this thesis, to allow for a parameter study for the properties of these hypothetical Twin stars, often abbreviated “Twins” in this work. As a first approach a Toy-model like the Bag model provides an EoS that is able to describe the deconfinement of quarks. Fig. 14 shows different EoS where each color interval represents a range of Bag constants. The color bar on the right side shows the value of  $B$ . A higher Bag constant leads to a higher chemical potential. If  $B^{1/4}$  is smaller than  $\approx 140$  MeV then both curves do not intersect, the same happens for  $B^{1/4} \geq 450$  MeV. In yellow one can see

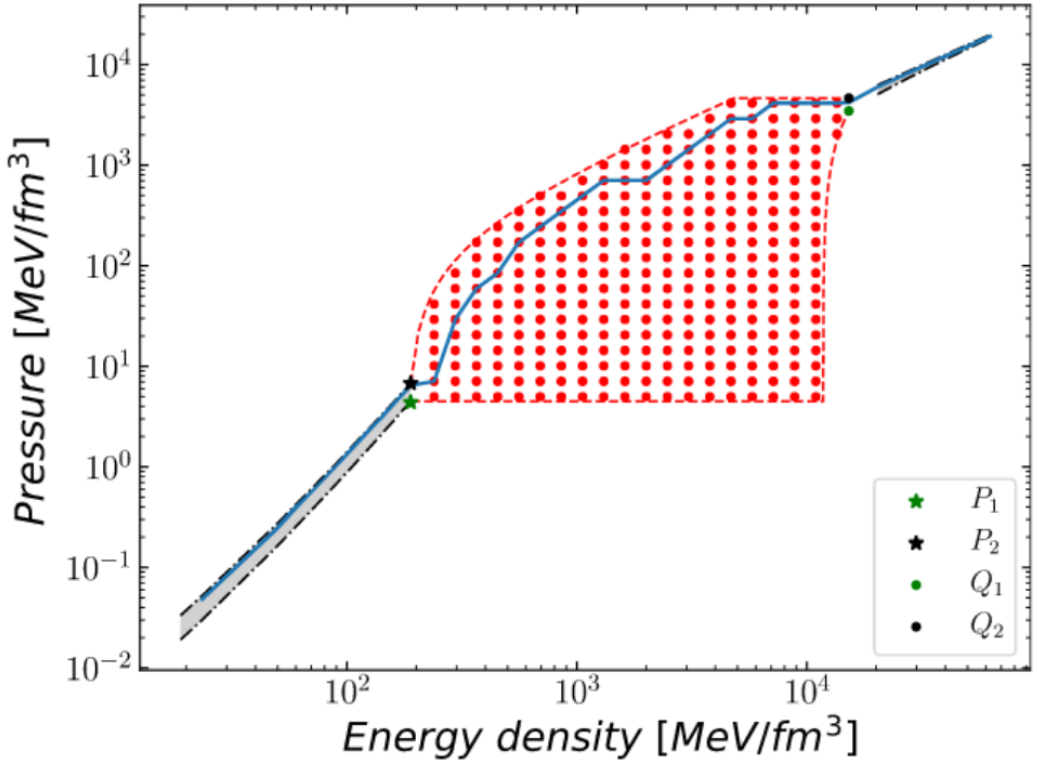


Figure 13: Pressure as function of energy density. The lower left and upper right lines are constraints for the EoS from first-principle hadron theory. Red grid nodes in the middle show allowed “pathpoints”. E. Oter calculated many EoS that choose random points with the only constraints being causality and monotony  $0 \leq dP/d\epsilon \leq c^2$  [79].

the Stefan Boltzman limit as a thin line. One Bag parametrization corresponds to one colour. The Bag model equations read

$$\frac{p}{\mu_q^4} = \frac{c}{162\pi^2} - \frac{B}{\mu_q^4} \quad (90)$$

$c$  is a prefactor that arises from the degeneracy factor, i.e. the amount of flavors I consider in my Bag model. For two flavors, it is 1 by definition of 6o. The intersection of the coloured curves with the parity doublet model shows a discontinuity in the first derivative of  $\frac{dP}{d\mu}$  which leads to a jump in baryon number density

$$n_B = \frac{\partial P}{\partial \mu_B}$$

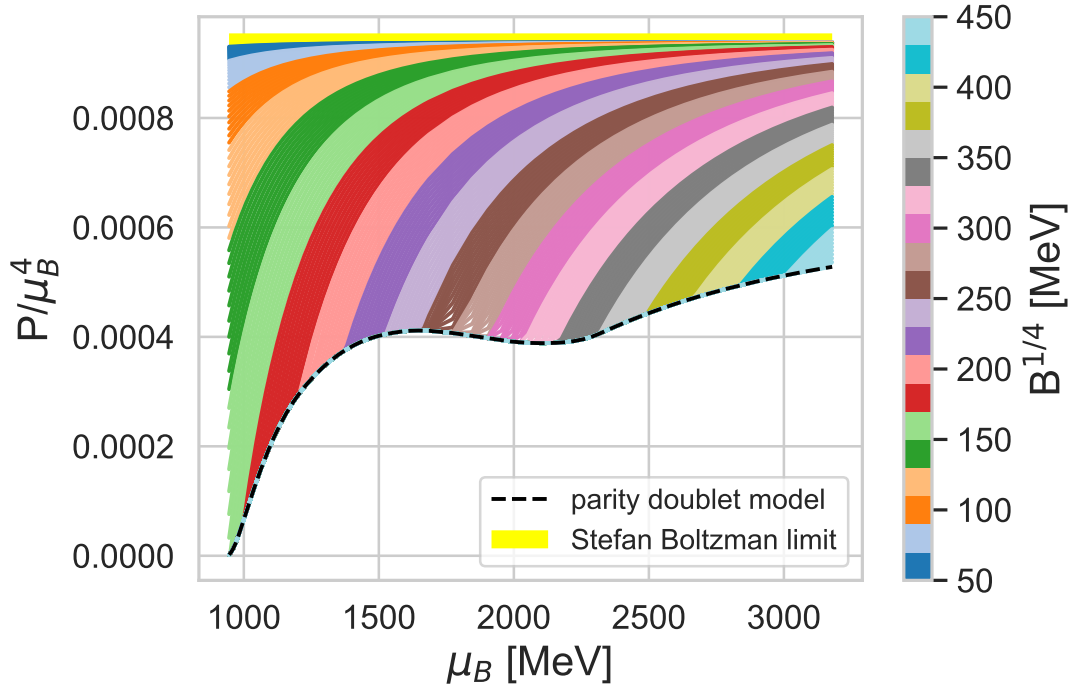


Figure 14: Pressure as function of baryon chemical potential. The colored areas are different Bag model EoS and the black dashed line is the CMF model EoS. A higher Bag constant shifts the Bag EoS to the right side and thus leads to a later phase transition. There's a lower and upper bound for  $B$  arising from the crossing points for both curves so that  $200 \leq B^{1/4} \leq 450$  MeV. The horizontal yellow line is  $a_3$ , see eq. 91.

A jump in  $n_B$  leads to a jump in the energy density  $\epsilon$  from the first law of thermodynamic at zero temperature  $\epsilon = -P + \mu_B \cdot n_B$  so that one obtains

$$\epsilon = -a_3 \mu_q^4 + \mu_q n_q + B, \quad a_3 \equiv \frac{1}{162\pi^2} \quad (91)$$

From now on I use the Baryon chemical potential  $\mu_B$  in units of the quark chemical potential  $\mu_q$  since  $\mu_q = \mu_B$  at the Maxwell construction. Summarizing the following steps are required

1. derive pressure (here in terms of chemical potential<sup>4</sup>)  $P/\mu_q^4 = -B/\mu_q^4 + a_3$
2. use the validity of the following condition at the Maxwell construction:

$$P_B^{\text{tr}} = \sum_i P_{q_i}^{\text{tr}} \quad \text{and} \quad \mu_B^{\text{tr}} = \sum_i \mu_{q_i}^{\text{tr}}$$

3. calculate the quark density:  $n_q = \partial p / \partial \mu_q = 4a_3 \mu_q^3$
4. calculate the energy density which is given by  $\epsilon = -P + \mu_q n_q$

In the following section I will show my results for the **M-R relations** for two and three flavor for the MIT bag model and for the three flavor **vMIT** bag model.

### 2.3.1 Two and Three flavor MIT Bag model

The following shows results for massless two and three flavor Bag models. In fig. 15a - fig. 15f, I plotted different mass-radius relations, corresponding EoS and dimensionless tidal deformabilities for the two (left column) and three flavor (right column) Bag model. The difference between a two and three flavor Bag model is the constant factor in eq. 63. For three flavors, the degeneracy  $2 \times 3 \times 3 = 18$  respectively for two spin states, 3 colours and 3 flavours. This results in an overall factor of 1.5 compared to two flavour limit with a degeneracy factor of 12. The horizontal black and blue line in the right plot is the Stefan Boltzmann limit, see eq. 91 (for three quark flavors it is shifted upwards). I introduce the constant  $c$  that encodes the amount of quarks as follows:

$$c \cdot a_3 \equiv \frac{N_i/2}{162\pi^2} \quad (92)$$

where  $c \equiv N_i/2$  and  $N_i$  is the number of quarks.  $a_3 = \frac{1}{162\pi^2}$ . The amount of quarks is then simply given by

$$N_i = 2 \times c \quad (93)$$

The colorbar at the right side of each plot shows different Bag parameters in multiple ranges. The black dashed lines in each of all 6 plots correspond to the **CMF** model and the colored ones represent **TOV**-solutions with different Bag parameters.

In fig. 15a and fig. 15b, we see the two and three flavor Bag model M-R relation relations. We see that for the red and yellow curves ( $B^{1/4} \approx 160 - 170$  MeV) in fig. 15a, the destabilization occurs in a rather smooth way. This means that the masses after the transition are still increasing for a little bit before they become unstable. For Bag constants above 175 MeV the branch becomes immediately unstable. In fig. 15b we see twin star solutions that correspond to two local maxima. The maximal masses are all smaller than  $\sim 1.5M_\odot$  which is very low compared to observed masses which are around  $2M_\odot$ . For two as well as three

flavors, a higher Bag constant leads to higher masses.

In fig. 15c and fig. 15d we see the EoS for the above M-R relations with pressure (in units of  $\mu_B$ ) as function of chemical potential  $\mu_B$ . We see the change in the Stefan Boltzmann limit in fig. 15d where the blue line (corresponding to three flavors) is shifted upwards relative to the black line (two flavor). The Bag parameters for three flavors is shifted upwards since smaller values would not intersect with the CMF curve anymore.

In fig. 15e and fig. 15f, I plotted the tidal deformability for the two and three flavor Bag model and compared it to the GW170817 signal. The shaded blue area is the result from a neural network that calculated the most likely tidal deformability. They used several observed masses and radii as training data and predicted what was the most likely EoS and tidal deformability for these observations [77]. One can see that for two flavors in fig. 15e,  $\Lambda$  lies within the blue area but for three flavors in fig. 15f the values for  $\Lambda$  are too low.

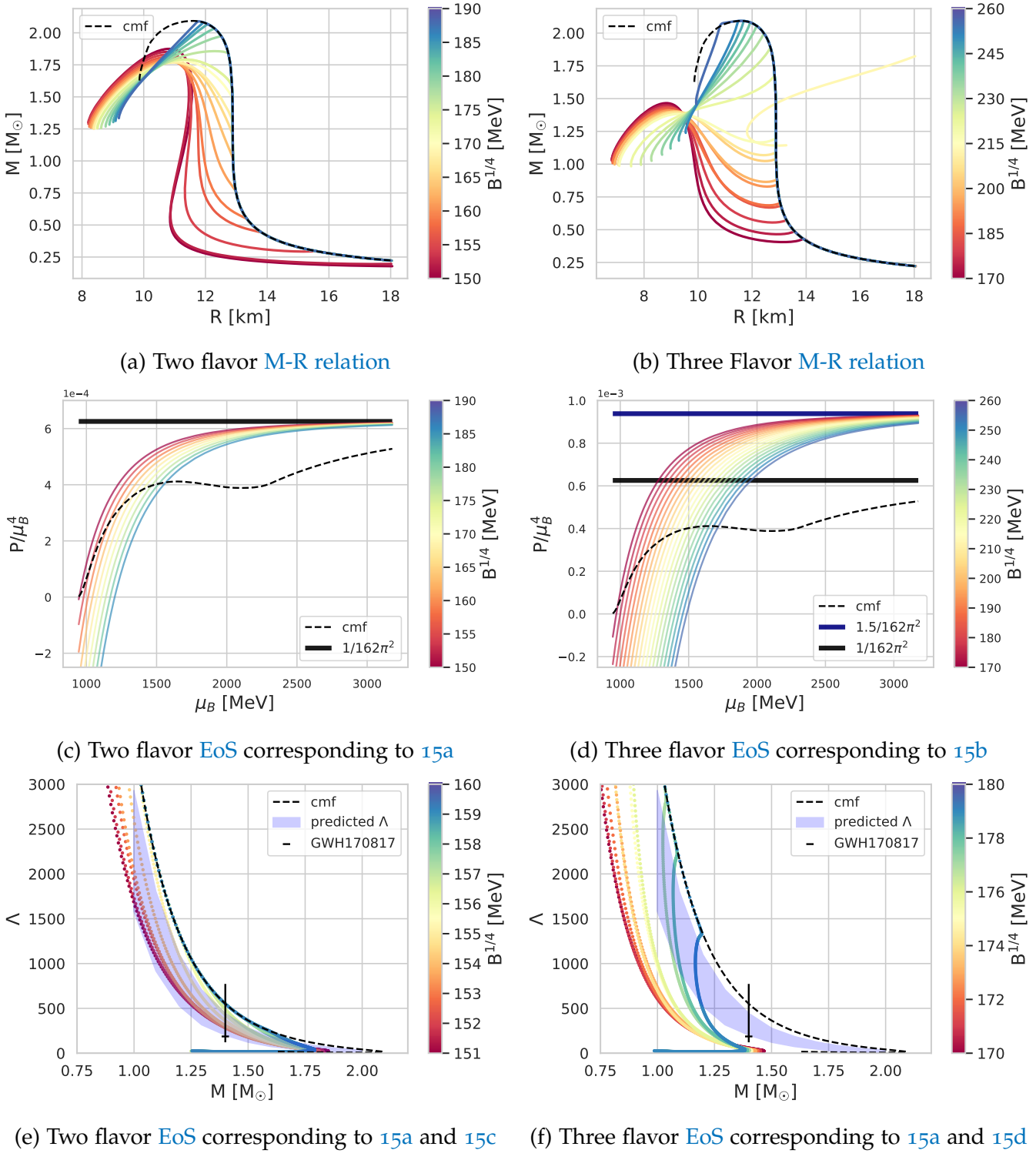


Figure 15

### 2.3.2 Investigation of flavor effects

In this following I want to compare different degeneracy factors and investigate their influence on masses, radii and possibly twin star solutions. The constant  $a_3$  from eq. 63 enters pressure and energy density, see eq. 90 and eq. 91 as a factor of degeneracy. We have seen that that for two and three flavors, this determines if Twin star solutions exist in the model. For two flavors we observed Twins whereas for three flavors we did not. To understand the reason for that, it is useful to plot different degeneracy factors (also non-physical floating points) and look for differences in the EoS. Fig. 16 shows six different equations of state (right side) and their corresponding M-R relations (left side).  $1.00 a_3$  corresponds to a two flavor Bag model.  $1.50 a_3$  corresponds to a three flavor Bag model, I have introduced the degeneracies in section 1.2.3.2 and 1.2.3.3. I recall eq. 93 where we related prefactor of  $a_3$  to the amount of flavors:

$$N_{\text{flavors}} = 2 \cdot c$$

I will now discuss the following 12 plots. The left plots on the following pages each show M-R relations with radii on the x-axis and masses on the y-axis. The black dashed line is the CMF model M-R relation. The color bar shows the Bag constant. For each degeneracy factor I used several different Bag constants in the range  $B^{1/4} \in [180, 280]$  MeV.

Correspondingly, the right side of each M-R relation shows the EoS. The black dashed line of these plots is the pure CMF EoS. The lower black horizontal line is the Stefan-Boltzmann limit for two flavors e.g.  $1.00 \times a_3$ . The upper horizontal line is the shifted limit (an increase in the prefactor increases the horizontal line, see eq. 90. In each plot there is a colored text showing the prefactor of  $a_3$ . There are two dominate factors, namely onset of Maxwell construction and angle of intersection that I will discuss in the following two points, each for the EoS and M-R relation

1. chemical potential at transition

- (a) **EoS**: increasing the flavors shifts the pure Bag curves to the left. This means that the chemical potential at the crossing point of CMF and Bag model is lower.
- (b) **M-R relation**: increasing the prefactor lowers the lowest purple curve because if the chemical potential at the Maxwell construction is lower, so is the corresponding mass in the M-R plane.

## 2. angle of intersection

- (a) **EoS:** The angle between the **CMF** model and the Bag model **EoS** (counterclockwise  $\angle(\text{CMF}, \text{Bag})$ ) depends on the amount of flavors. For a prefactor of 1.5 the angle is around 45 deg whereas if the prefactor is 2 then the angle is between 45 deg and 90 deg. A larger angle means the same as a larger difference in the slope of both **EoS**. Since the baryon density is given by the partial derivative of  $P$  with respect to  $\mu_B$ , a larger change in slope corresponds to a larger jump in the Baryon number density  $n_B$  and thus  $\epsilon$ , see eq. 91.
- (b) **M-R relation:** Twin star solutions only exist if the jump in energy density is larger than a specif value, it is called Seidov limit and given by eq. 97. I will discuss it in detail in section 2.5. For smaller flavors, only one Twin star solution exists whereas for 4 flavors, the third curve vom below (light purple) has two maxima.

Freedman et al. analyzed a **QCD** Bag model with massless up and down quarks and a finite mass for the strange quark  $m_s = 280$  MeV. They chose a Bag constant  $B^{1/4} = 53$  MeV and predicted that a quark star would have strangeness comparable to its baryon number [81].

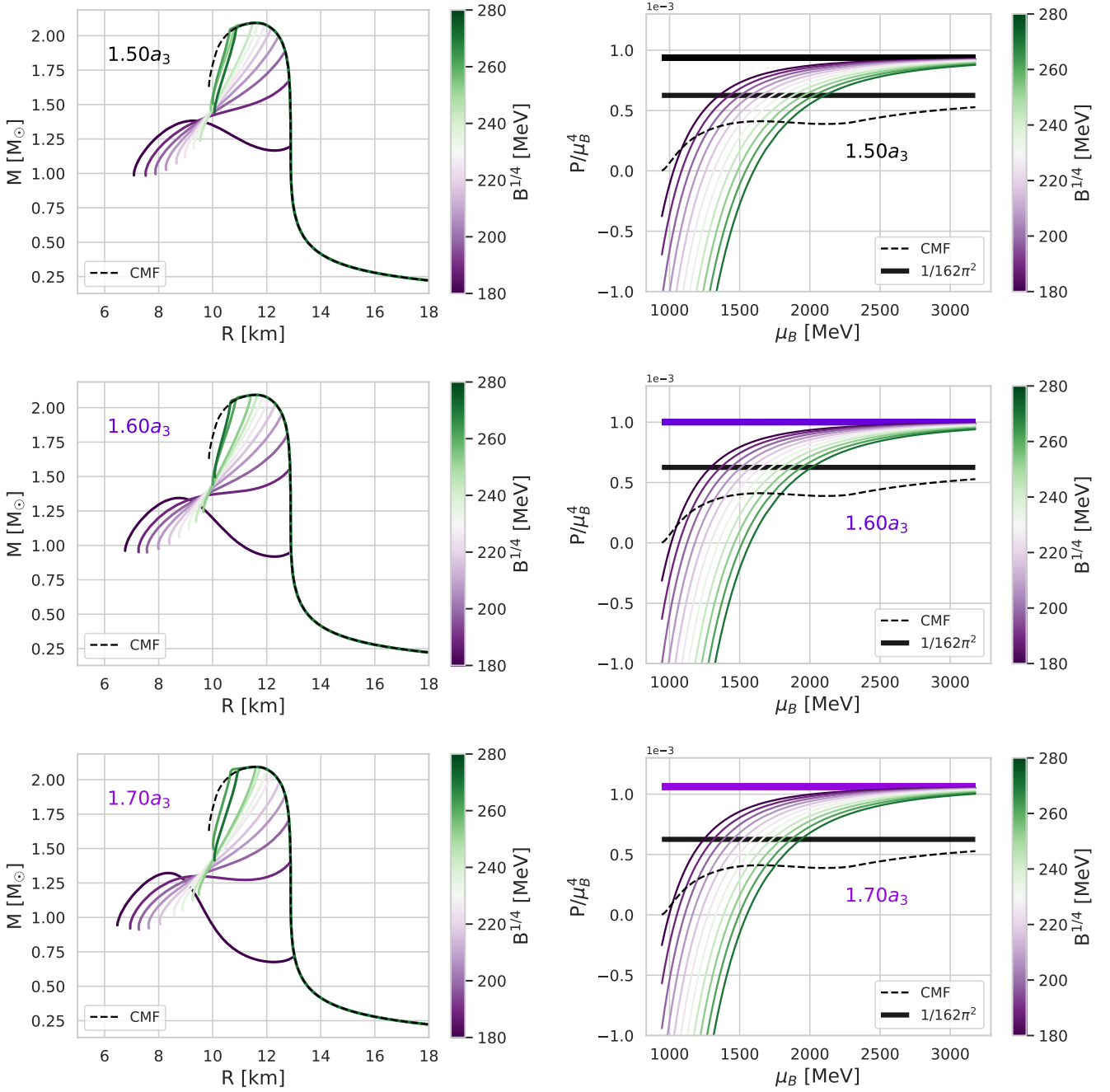


Figure 16: **Left column:** M-R relations for  $N_{\text{flavor}} = 3, 3.2, 3.4$ . The prefactor of  $a_3$  (colored text in each plot) multiplied with 2 gives the amount of quarks.

**Right column:** Corresponding EoS. Several Bag constants for each plot, their values are color encoded. The horizontal line in the right column is shifted if one increases the degeneracy factor. The colored text in each plot shows  $c \cdot a_3$  of the definition in eq. 93. A higher degeneracy factor leads to an earlier phase transition and thus earlier off branching between CMF and Bag branch in the M-R plane. Twin star solutions are more likely for larger degeneracy factors because the latent heat then is higher, see the description in the text. For  $1.70a_3$  we see that the dark and light green Bag model curves exceed the mass of the pure CMF model at a given radius. For  $1.60a_3$  and  $1.80a_3$  this effect is also present but less pronounced.

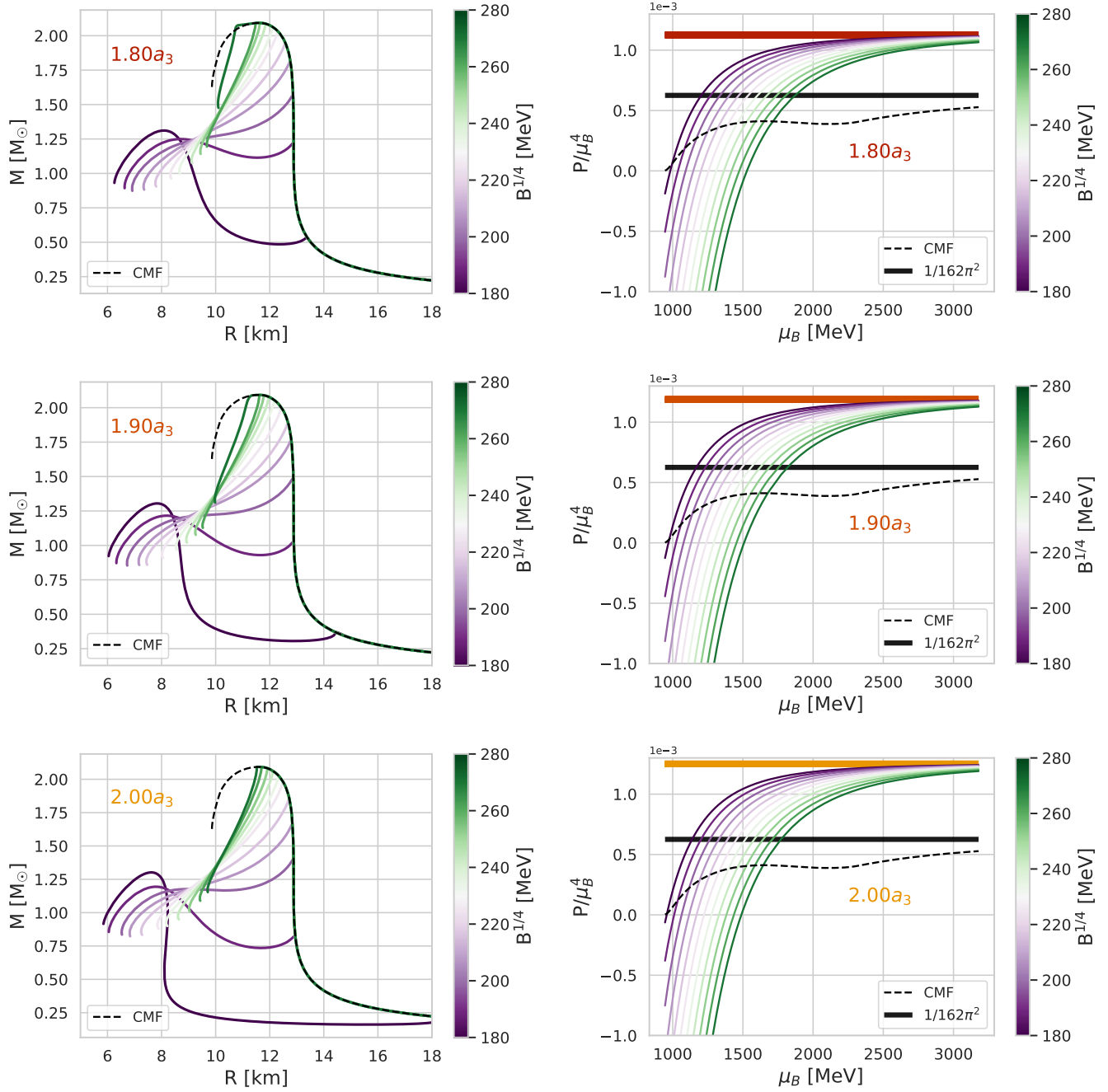


Figure 17: **Left column:** M-R relations for  $N_{\text{flavor}} = 3.6, 3.8, 4.0$ . The prefactor of  $a_3$  (colored text in each plot) multiplied with 2 gives the amount of quarks.

**Right column:** Corresponding EoS.

Several Bag constants for each plot, their values are color encoded. The horizontal line in the right column is shifted if one increases the degeneracy factor. The colored text in each plot shows  $c \cdot a_3$  of the definition in eq. 93. A higher degeneracy factor leads to an earlier phase transition and thus earlier off branching between CMF and Bag branch in the M-R plane. It is interesting how all curves in the M-R plane intersect. This could be subject of further investigation. For  $1.70a_3$  we see that the dark and light green Bag model curves exceed the mass of the pure CMF model at a given radius. For  $a.60a_3$  and  $1.80a_3$  this effect is also present but less pronounced.

Oppenheimer and Volkoff already calculated the lowest masses for NSs in 1939 with a lower bound of  $\sim 0.7M_{\odot}$  [82]. High masses can precisely be measured with the Shapiro time delay and have an upper bound of  $2M_{\odot}$  [83]. The possible maximum mass of a hypothetical Bag EoS quark star made up purely of quark matter can be approximated by numerical integration of the TOV equations using the universal Bag EoS in eq. 96 and [4, 84]. For the maximum mass one obtains

$$M_{\max} \sim 1.78 \left( \frac{155 \text{ MeV}}{B^{1/4}} \right)^2 M_{\odot} \quad (94)$$

(95)

The corresponding radius scales as  $R \sim 9.5 \left( \frac{155 \text{ MeV}}{B^{1/4}} \right)^2 \text{ km}$ .

Changing quark flavors does not change the maximum masses and radii since only  $B, P$  and  $\epsilon$  enter the EoS  $P = \frac{1}{3}(\epsilon - 4B)$ . A higher Bag constant lowers the maximum mass and the corresponding radius. I plotted the M-R relation in fig. 18a and fig. 18b for two and three flavor Bag model respectively. The M-R relations are identical with the ones in fig. 15a and fig. 15b. In this plot here, I included points that refer to the maximum pure quark Bag model mass and corresponding radius. The maximum Bag masses for a two flavors Bag model in fig. 18a and  $B^{1/4} \in [160, 190]$  lie below the transition masses. No Twin star solutions occur. For the M-R relation of the three flavors Bag model in fig. 18b with  $B^{1/4} \in [180, 280]$  MeV we see that Twins are possible because the maximum mass of 94 lies below. One has to keep in mind that a direct comparison of both EoS, Bag and modified CMF Bag EoS, is not possible since the hadronic part distorts the maximum Bag model mass and corresponding radius.

### *Conclusion*

In this chapter I investigate possible twin star solutions with a combined CMF Bag model. As we have seen, the Bag constant  $B$  determines the chemical potential at which the Maxwell construction takes place. We have also seen that a two flavour model is not sufficient to obtain twin stars but that a three flavour Bag model yield them within a certain range for  $B$ . I will now give a overview over the two parameters  $a_3$  and  $B$  that I varied and their consequences for the EoS and the M-R relation

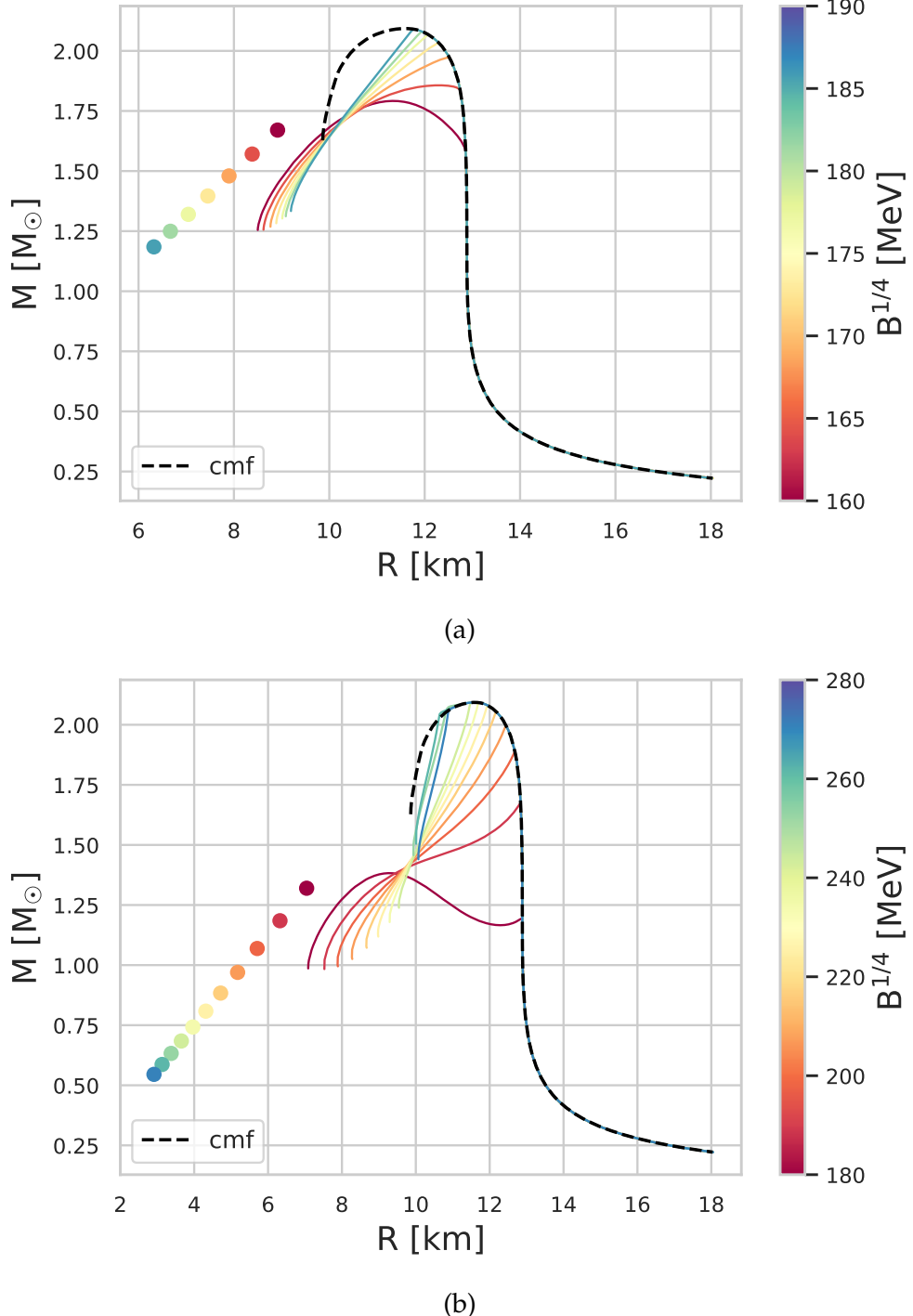


Figure 18: **M-R relation** of the two and three flavor Bag **EoS**. Each dot represents a maximum Bag model mass and the corresponding radius of a pure Bag star without **CMF** part. If the mass at the Maxwell construction of the “modified **CMF EoS**” is above the maximum Bag mass then no Twins occur. This is the case in the **upper** plot where I used the two flavor Bag model. All points lie below the masses of the modified **EoS** at the Maxwell construction. The **bottom plot** shows qualitatively the same but this time with a three flavor Bag **EoS**. There lowest M-R curve is a Twin star solution because it has two maxima. Only for the lowest Bag constant of  $B^{1/4} = 180$  MeV two maxima are possible because all other transition masses are higher than the corresponding pure Bag maximum mass.

- **Bigger values for  $a_3$**  lead to a steeper slope at a **lower chemical potential** (recall:  $P(\mu) = a_3 - B/\mu^4$  diverges faster at  $\mu \rightarrow 0$  for larger values of  $B$ ), this leads to an **earlier phase transition** (i.e. at lower pressure). The angle of intersection of the two curves e.g.  $\angle(\text{cmf}, \text{bag model})$ <sup>3</sup> is larger. This increases the jump height in the baryon density. This in turn implicates a **larger jump in energy density**. Since the Baryon density is the partial derivative of pressure with respect to baryon chemical potential, the change in slope of the **CMF** model and bag model is direct proportional to the latent heat.
- **Bigger values for  $B$**  increase the **maximum mass** and shift the phase transition to a **higher chemical potential**. Twin stars appear for lower Bag constants. For the three flavor model, twins occur for  $B^{1/4} \in [170, 180]$  MeV. The reason why higher Bag values do not lead to twins is the same reasoning as for lower values for  $a_3$ :  $\angle(\text{cmf}, \text{bag model})$  is bigger leading to a **higher jump in energy density**. Scaling the **TOV** equation for the particular choice of free quarks one can show that radii and masses scale  $\propto B^{1/2}$  [4].

This behaviour is illustrated in fig. 19.

The investigation above demonstrates that for two flavours the phase transition is not sufficient sharp to destabilize the star. For three flavours on the other hand, twin star solutions occur for lower values of  $B$ . However, the masses are still very low for all Bag constants and different limits of  $a_3$ . The Bag model is constructed in such a way that it does not exceed the Stefan Boltzmann limit of  $1/3c$  at  $T = 0$ . The validity of this choice has been confirmed by lattice calculations [85]. The MIT Bag model softens the **EoS** and fixes the speed of sound  $v_s^2 = \frac{dp}{de}$  to  $1/3$  as one can see by basic thermodynamic relations

$$\begin{aligned}
P_{Bag} &= a_3 \mu^4 - B \\
n_B &= \frac{\partial P}{\partial \mu_B} = 4a_3 \mu_B^3 \\
\epsilon_{Bag} &= -P_{Bag} + 4a_3 \mu_B^4 \\
&= 3a_3 \mu_B^4 + B \\
\Rightarrow P_{Bag} &= \frac{1}{3}(\epsilon_{Bag} - 4B)
\end{aligned} \tag{96}$$

---

<sup>3</sup>Clockwise

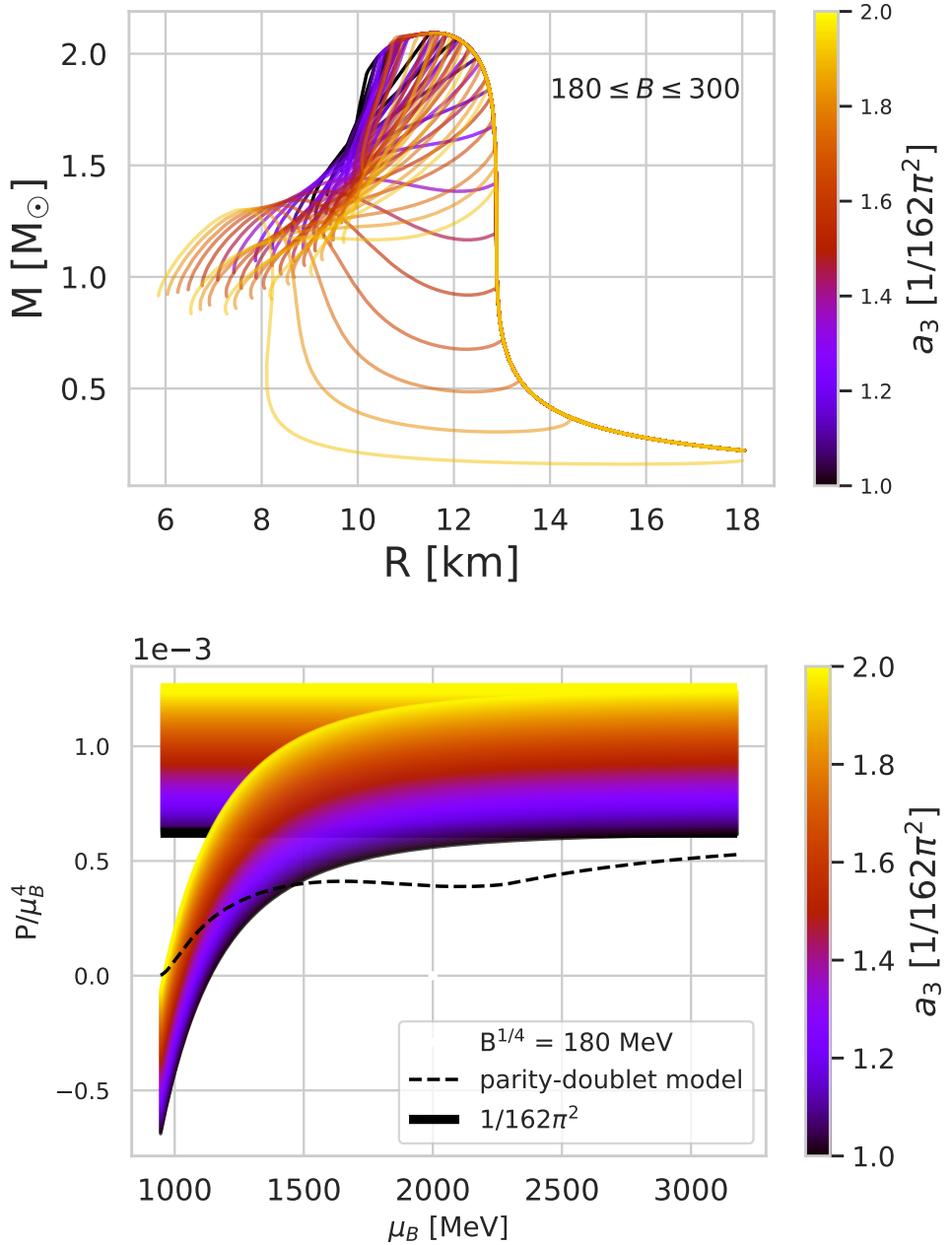


Figure 19: **Upper:** Mass-radius relation for different degeneracy factors that result in shifted Stefan-Boltzman limits. A higher degeneracy leads to lower masses and possible twin star solutions. I also plotted different Bag constants  $B \in [180, 300]$ . Each curve of the same color corresponds to one fixed Bag constant. **Bottom:** Pressure as function of chemical potential in units of  $\mu_B^4$ . Different colors show different Stephan Boltzman limits up again which the EoS converges.  $a_0 = 1.5$  corresponds to 3 flavors and  $a_0 = 1$  to two flavors. The black dashed line is the pure CMF EoS. The lowest limit (black) corresponds to a prefactor for  $a_3$  of 1.

$B^{1/4}$	$\in [166, 250]$ MeV
$a_0 \equiv g_q/m_\omega$	$\in [0, 1.75]$ fm $^{-2}$

Table 2: Varying parameters

## 2.4 VMIT BAG MODEL

The motivation to use a vector enhanced Bag model is to construct a stiffer EoS for the quark phase. The standard MIT Bag model softens the EoS, see eq. 96 with a constant speed of sound of 1/3. With the vMIT bag model we consider repulsive vector interactions<sup>4</sup>. This stiffening could lead to higher mass twin star solutions. The masses of up, down and strange quarks are 1 MeV for up and down and 100 MeV for the strange quark. To summarize some fundamental changes to the standard MIT Bag model as follows

- quark masses are non zero
- mesons appear in the Lagrangian
- additional pressure contribution form the quark -  $\omega$  interaction  $g_V^\omega$

The fig. 20 and fig. 21 show 6 different M-R relations (left) with their corresponding EoS (right) with 6 different Bag constants [166, 171, 180, 190, 200, 250] MeV, as written is the title of the plot. The different color lines with corresponding color bar in each plot show different quark coupling parameters  $a_3$ .  $a_3$  is proportional to the repulsion of the quarks to the  $\omega$  meson and proportional to the stiffness of the EoS.

The black star in each EoS figure is the maximum mass as obtained from the pure CMF model. Higher values for  $a_0$  stiffen the equation of state because they increase the repulsive force between quarks. Note that in the  $P/\mu^4 - \mu$ -plane, stiffer means smaller slope  $\frac{dP}{d\mu}$ . A higher Bag constant leads to a later phase transition, this is the same behaviour we observed for the pure Bag model. For  $B^{1/4} = 180$  MeV we observe twins however they do not yield masses above  $1.5M_\odot$ . The ambition behind choosing a repulsive Bag model was to increase the maximum masses of Twins however it seems that a stiff enough quark EoS alone is not a sufficient criterion for stable stars. Let's have a look at high coupling constants (grey color) in the EoS. Both EoS, CMF and Bag model EoS

---

<sup>4</sup>A vector meson is a meson with total spin 1 and odd parity. In this model we consider  $\omega$  and  $\rho$  mesons.

lie nearly parallel. On the one hand this is expected since the Bag curve is now very stiff, the change in slope of both EoS models differs less. But the crucial point is, in analogy to the reasoning for the flavor variation of the simple Bag model, that the quantitative change in slope of both curves is a direct measure for the latent heat  $\Delta\epsilon$ . Even if the vMIT Bag EoS is very stiff it does not destabilize the star because  $\Delta\epsilon$  lies below the Seidov limit.

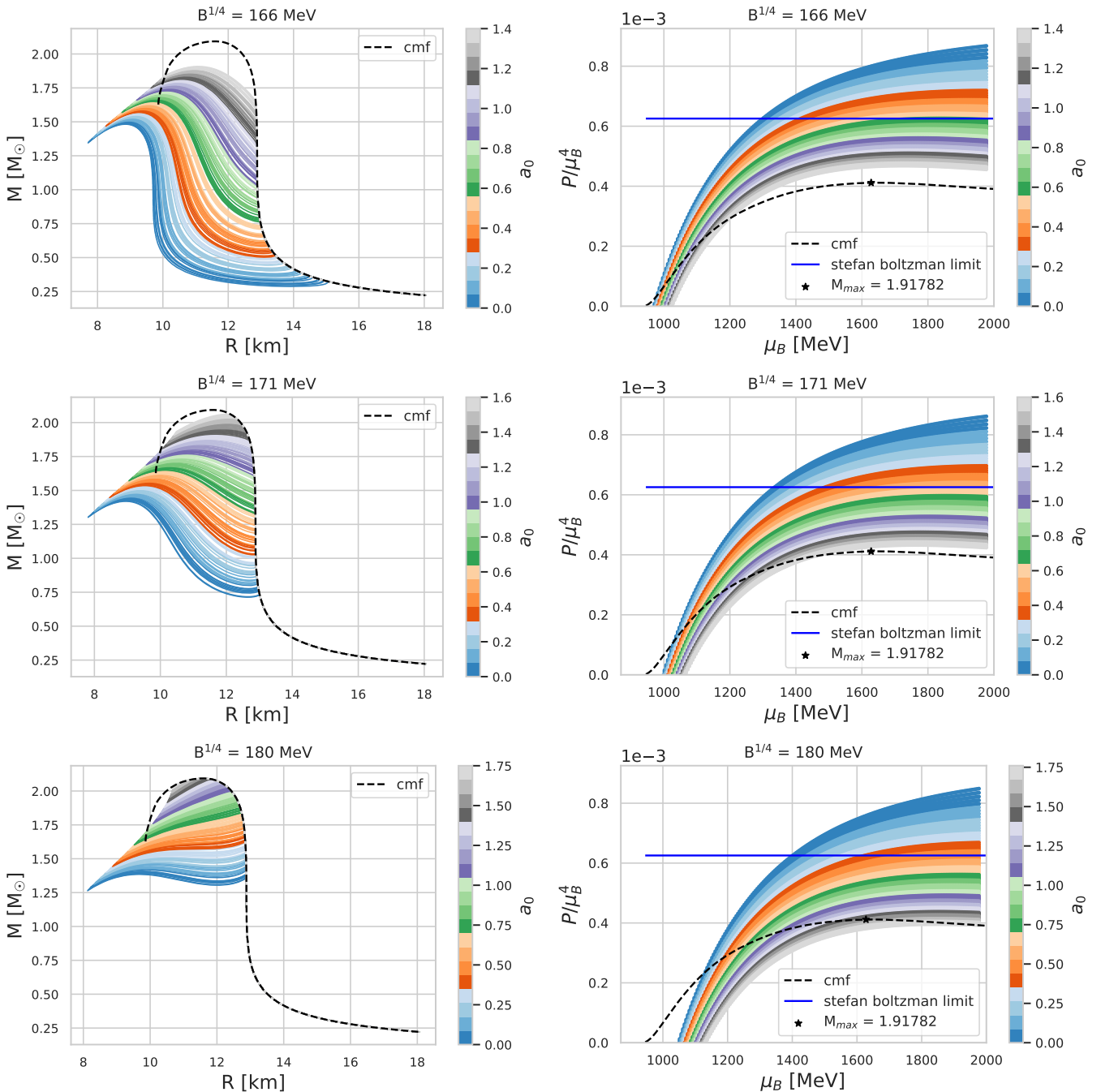


Figure 20: **Left column:** [M-R relation](#) for three different Bag constants  $B^{1/4} \in [166, 171, 180]$  MeV. The colorbar in each row shows different quark couplings ranging from small values (blue) to high values (grey). **Right column:** corresponding [EoS](#). The black star  $M_{\text{max}}$  is the maximum mass of the pure [CMF](#) curve and the blue horizontal line is the two flavor Stefan-Boltzmann limit. Smaller values for  $B$  shift the transition to smaller masses, this behaviour was also observed for the pure Bag model. Higher repulsion shifts the transition to slightly higher transition chemical potentials. It also changes the slope, higher values ( $\rightarrow$  higher repulsion) stiffens the [EoS](#).

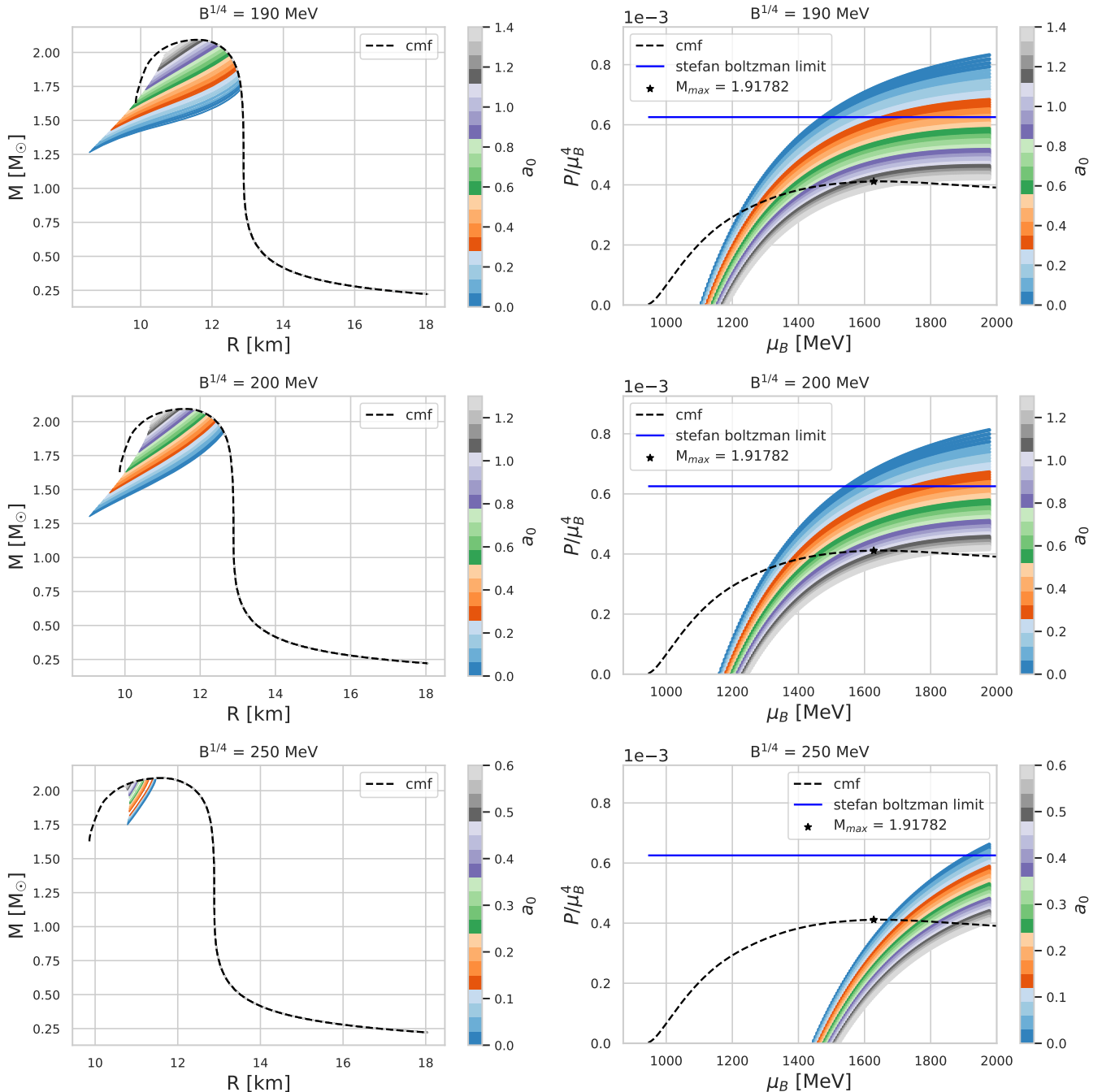


Figure 21: **Left** column: [M-R relation](#) for three different Bag constants  $B^{1/4} \in [190, 200, 250]$  MeV. The colorbar in each row shows different quark couplings ranging from small values (blue) to high values (grey). **Right** column: corresponding [EoS](#). The black star  $M_{\max}$  is the maximum mass of the pure CMF curve. There are no Twin star solutions because the Bag constant shifts the transition to a too high chemical potential where the pure CMF EoS is much stiffer than the vMIT Bag EoS.

### Conclusion

To summarize the interplay of the coupling strength  $a_0$  and the Bag constant  $B$  in the framework of the vMIT Bag model, we have the following properties:

1. The **coupling**  $a_0$  influences the onset of transition. A smaller coupling leads to a smaller latent heat. The reason is the decreasing angle between the CMF and Bag model curve which influences the latent heat.
2. The **Bag constant** also regulates the latent heat. A smaller Bag constant decreases the latent heat and the onset of the phase transition is shifted towards lower chemical potential. Possible Twins only occur if the Bag constant is above *sim*180 MeV, this softens the vMIT EoS because it shifts the curve parallel along the x-axis to higher chemical potentials. The star is then immediately unstable after the transition.

Following these points, problems arise when the latent heat  $\Delta\epsilon$  is too small. This is the case if the angle of both EoS lie nearly parallel. A stiff quark EoS decreases this angle. A stiff EoS in the deconfined phase is necessary if one want to enforce Twins. One could chose a very large coupling  $a_0$  so that the quark EoS is stiffer than the hadronic EoS, but this clearly contradicts the deconfinement mechanism. Specifically in this framework it would not be possible since  $a_0$  has an upper limit that arises simply by the fact that both curves need to intersect. Instead of stiffening the quark EoS one cold soften the hadronic EoS. This could be done in future work, for example by adding  $\Delta$  Baryons. The third idea on how to enforce a Twin star solution would be to have a stiff hadronic EoS at the transition, followed by a soft quark EoS that stiffens quickly after the transition.

## 2.5 SEIDOV LIMIT AND TWIN STARS

In this section I investigate how the transition pressure and latent heat change behaviour of M-R relations, the  $k_2$  number and tidal deformability  $\Lambda$ . There is a generic condition for stellar equilibrium, called Seidov limit. It provides a constraint for the latent heat  $\Delta\epsilon^5$  and the transition pressure  $p_{\text{trans}}$  and is defined as

$$\frac{\Delta\epsilon_{\text{trans}}}{\epsilon_{\text{trans}}} \geq \frac{1}{2} + \frac{3}{2} \frac{p_{\text{trans}}}{\epsilon_{\text{trans}}} \quad (97)$$

---

<sup>5</sup>Latent heat refers to the discontinuity in energy density at the phase transition.

The instability of a star is proportional to the value of  $p_{\text{trans}}$  and inverse proportional to the gap  $\Delta\epsilon_{\text{trans}}$  in energy density. Twin star branches can only occur if condition (97) is fulfilled. To create this discontinuity in  $\epsilon$  I use the naive ansatz to add a constant in  $\epsilon$  to the CMF EoS. The EoS above this point is parallel to the original CMF model EoS. Since the energy density of the modified EoS is slightly higher while the pressure is unchanged, one expects the M-R relation to become unstable earlier than as for the unchanged CMF EoS<sup>6</sup>. The chemical potential at the Maxwell construction with the two “phases” 1 and 2, for before and after the “transition” respectively reads

$$\mu_B^1(P_{\text{trans}}) = \mu_B^2(P_{\text{trans}}) \quad (98)$$

where  $\mu_B$  is the baryon chemical potential. Fig. 22 to fig. 24 shows the masses, tidal deformabilities and  $k_2$  Love numbers for different transition pressures and jumps in energy density. The columns show different values for  $\Delta\epsilon$  and each row has a different  $p_{\text{trans}}$ . It is more likely to have twins in the upper right where the transition pressure is smaller and the latent heat bigger, this follow from the Seidov limit in condition 97. The shaded areas are configurations with a second branch where the energy density is high and the pressure low enough to destabilize the star. In this case, the Seidov limit (black text) at the transition pressure is lower than the energy gap so that on top of each column which leads to a unstable branch. I chose multiple values for energy density and transition pressure in the range  $\Delta\epsilon \in [100, 600] \text{ MeVfm}^{-3}$  and  $p_{\text{trans}} \in [10, 270] \text{ MeVfm}^{-3}$  and also plotted the  $k_2$  Love number and tidal deformability  $\Lambda$ .

---

<sup>6</sup>An increase in energy density increases the gravitational mass of the star.

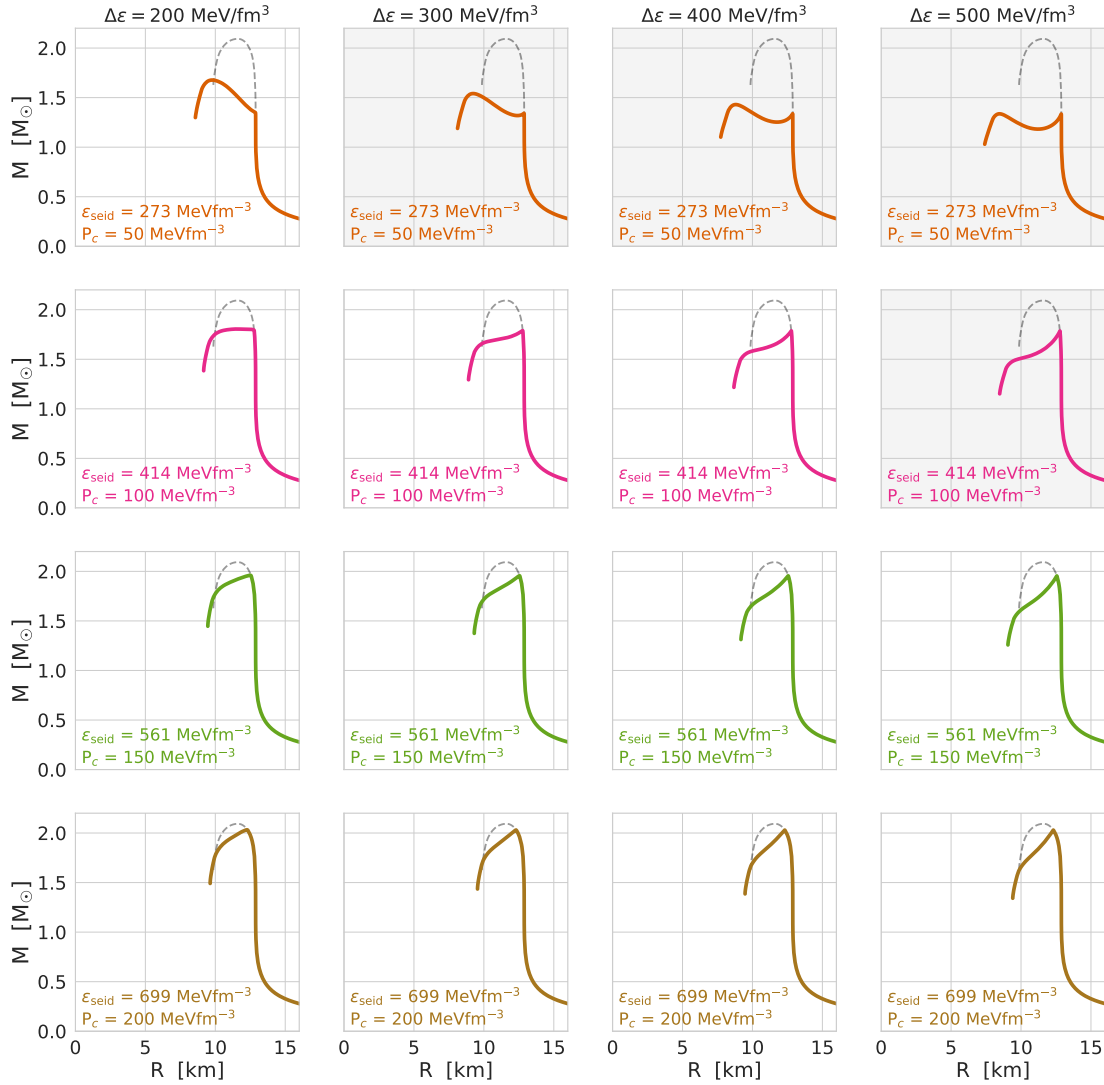


Figure 22: Here we see  $4 \times 4$  different **M-R relations**. 4 different transition pressures (see color bar) and 4 different latent heats (see text at top) are shown with all possible combinations of  $\Delta \varepsilon$  and  $p_{\text{trans}}$ . Identical colors refer to the same transition pressure. There are plots with a light grey shaded background. These are configurations that fulfill the Seidov limit in eq. 97. Stable Twins can only occur in shaded areas but they don't have to: They occur in the upper right part of the first row but the right plot in the second row does not show Twins. Twins do not appear also if the pure **CMF EoS** still supports stable stars and the latent heat lies above the Seidov limit. This shows that speed of sound (i.e. stiffness) alone is not a sufficient criterion for stable stars. An already mentioned reason here is that the energy density is increased by a constant factor, leading to a shift in the star's gravitational potential.

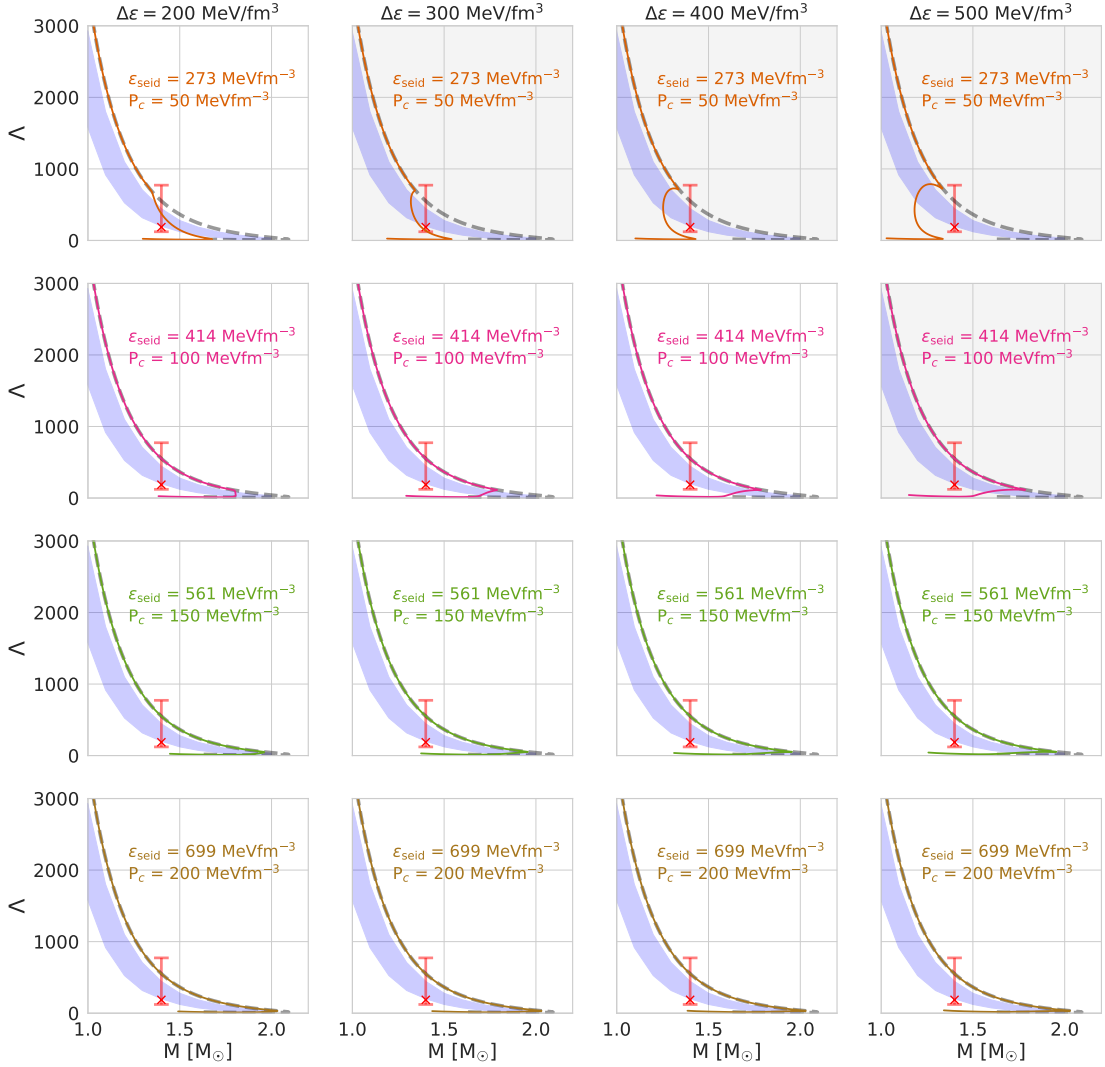


Figure 23: The  $4 \times 4$  plots show the dimensionless tidal deformability as a function of mass. Each plot corresponds to the [M-R relation](#) above. Each row (and so each color) has a different transition pressure and each column shows 4 different latent heats  $\Delta\epsilon$ . The shaded area is a prediction from a neural network from Fukushima [77]. It has the same shape and slope as the [CMF EoS](#) but lies below it (I have discussed this in Chapter 2.2). The red cross is the observed signal from GW170817 with the light red errorbars in  $\Lambda$  and  $R$ . The beginning of an unstable branch in the M-R plane can be observed as a drop in a drop in  $\Lambda$ . We observe this for all Twin star solutions. It can be interpreted as follows: The [EoS](#) at the transition from phase 1 to phase 2 leads to a sudden softening of the [EoS](#). A softer [EoS](#) lowers the tidal deformability of a star (stars with softer [EoS](#) have a higher compactness).

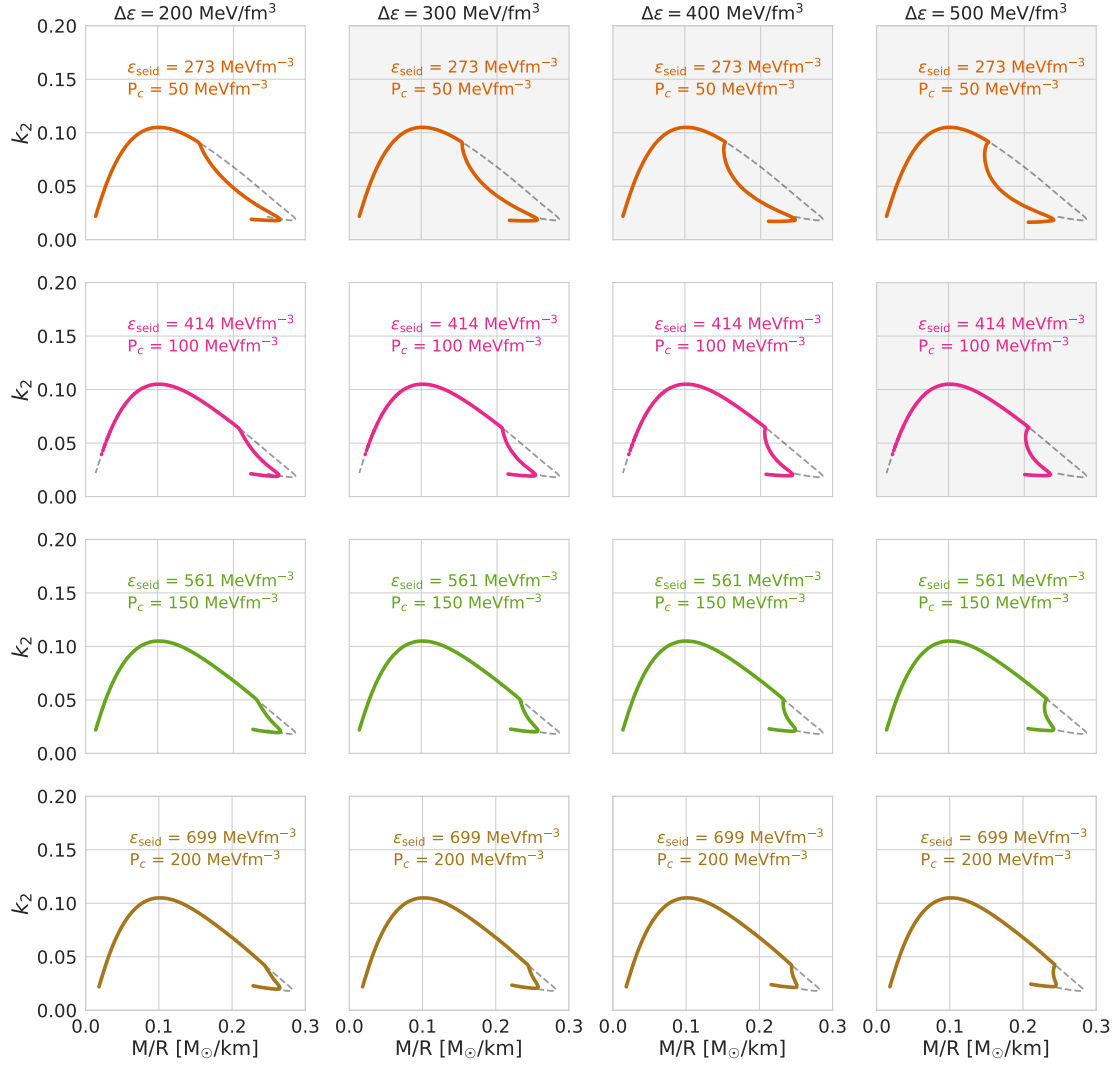


Figure 24: Here, the  $4 \times 4$  plots show the  $k_2$  Love number (in units of  $[km/M_\odot]$ ) as function of compactness. Each plot corresponds to the [M-R relation](#) above. Each row (and so each color) has a different transition pressure and each column represents different latent heats  $\Delta\epsilon$ . The  $k_2$  Love numbers of the first unstable and second stable branch have lower compactness than the pure [CMF EoS](#) stars (this corresponds to the region where the modified curves differ from the dashed [CMF](#) ones). A reason is that  $k_2$  is very sensitive to the compactness and to the star's internal structure. One can observe here that  $k_2$  decreases if one softens the [EoS](#) (softening in this example means increasing the energy density).

## 2.6 CONCLUSION AND OUTLOOK

In my thesis it is studied whether high mass Twins are viable if the following first two points are used:

1. Stiffening of neutron matter at high densities.
2. Soft behaviour of quark matter at the hadron-quark phase transition, in order to have a sufficiently large latent heat.
3. Stiffening of quark matter above the deconfinement transition to obtain second stable branch (this could also be approached by a density dependent quark vector coupling).

This is in agreement with results from [86]. A stiff hadronic EoS and soft quark EoS in the transition region gives the necessary amount of latent heat. The quark EoS would then again have to stiffen to ensure a second stable branch. This could be formulated within a density dependent repulsive quark coupling framework, as it has been investigated here [87]. This is an interesting concept that could be investigated in future studies. The attempt to use the MIT and vMIT Bag model to obtain high mass twin solutions above  $2M_{\odot}$  was not successful in this limited framework. But even if we obtained higher masses, it is worth looking at implications and constraints from vector interactions in the quark and in the baryon phase by comparison to lQCD. The question that arises is whether a stiff quark EoS contradict results from lQCD. This has been investigated in the past by comparing model and lQCD baryon number susceptibilities. It has been shown that even a small coupling constant would lead to a significant deviation of the baryon number susceptibilities as calculated in lQCD [63, 62]. This does not contradict the two solar mass constraint for Twins, it only states that high mass NSs might not be described within this framework by a repulsive quark EoS but rather by a very stiff hadronic EoS, as described above.

The role of hyperons for the structure of NSs is not clear. Hyperons are baryons with non-zero strangeness. The high Fermi energy at large density could favor adding hyperons if their masses lie below their chemical potential of the nucleons. Stable non-zero strangeness stars can not be ruled out from a particle physics perspective. Because they may soften the EoS, problems can arise with the observed two solar mass constraint. In this thesis, only baryons from baryon octet were taken into account, see the l.h.s. of table 3. Adding delta baryons and other higher resonances may soften the EoS. It would be interesting to see

neutrons, protons	$n, p$	Delta baryons	$\Delta^-, \Delta^0, \Delta^+, \Delta^{++}$
Lambda particle	$\Lambda$	Sigma baryons	$\Sigma^{*-}, \Sigma^{*0}, \Sigma^{*+}$
Sigma baryons	$\Sigma^-, \Sigma^0, \Sigma^+$	Xi baryons	$\Xi^{*-}, \Xi^{*0}$
Xi baryons	$\Xi^-, \Xi^0$	Omega baryon	$\Omega^-$

Table 3: Baryon octet (l) and decouplet (r). The eight-fold way is a classification scheme for hadrons. Baryons can be grouped into octets and decouplets [88]. Particles of the baryon octet are composed of three quarks with two spins paired so their total angular momentum is 1/2. The decouplet baryons consist of three quarks with aligned spins, so they have total angular momentum 3/2.

how higher resonances and in particular the baryon decouplet would affect NS masses. Quark vector repulsion in the CMF model is an interesting way to further explore effects of quark matter in NSs.



# A

## WEIGHT OF A PINHEAD

---

Let's assume the following approximations for radius, core density and shape of a NS:

$$\begin{aligned} R_{\text{NS}} &= 10 \text{ km} \\ \bar{\rho}_{\text{core}} &= 9 \cdot 10^{17} \frac{\text{kg}}{\text{m}^3} \\ V_{\text{NS}} &= \frac{4}{3} \pi R^3 \bar{\rho} \\ \Rightarrow \text{Mass of neutron star} &\approx 2.1 \cdot 10^{30} \text{ kg} \end{aligned}$$

The radius of a pinhead is approximated by:

$$R_{\text{pinhead}} = 1 \text{ mm}$$

The ratio of both radii to the power of three is then  $\left(\frac{R_{\text{pinhead}}}{R_{\text{NS}}}\right)^3 \approx 1 \cdot 10^{-21}$ .

From this results one obtains the mass of a pinhead filled with neutron star core matter:

$$\begin{aligned} m_{\text{pinhead}} &= 1 \cdot 10^{-21} \times 2.1 \cdot 10^{30} \text{ kg} \\ &\approx 2 \cdot 10^9 \text{ kg} \end{aligned}$$

The following estimation is made for the adult human mass [89]

$$M_{\text{humans}} \approx 3 \cdot 10^8 \text{ kg}$$

Therefore the pinhead would weigh several times more than the current world population for typical neutron star core densities.



## REFERENCES

---

- [1] B. W. Carroll and D. A. Ostlie. *An introduction to modern astrophysics*. Pearson, 2nd edition, 2017, page 1400. ISBN: 0805304029.
- [2] J. W. T. Hessels, S. M. Ransom, I. H. Stairs, P. C. C. Freire, V. M. Kaspi, and F. Camilo. A Radio Pulsar Spinning at 716 Hz. *Science*, 311(5769):1901–1904, 2006. ISSN: 0036-8075. doi: [10.1126/science.1123430](https://doi.org/10.1126/science.1123430). arXiv: [0601337](https://arxiv.org/abs/0601337) [astro-ph].
- [3] F. Tondeur, D Berdichevsky, and M Farine. Nuclear matter saturation density: From finite nuclei to infinite matter. *Zeitschrift für Physik A Atomic Nuclei*, 325(4):405–413, 1986.
- [4] G. Baym, T. Hatsuda, T. Kojo, P. D. Powell, Y. Song, and T. Takatsuka. From hadrons to quarks in neutron stars: a review. *Reports on Progress in Physics*, 81(5):56902, 2018.
- [5] R. O. Gomes, S. Schramm, and V. Dexheimer. Modeling magnetic neutron stars: a short overview. *arXiv preprint arXiv:1805.00341*, 2018. arXiv: [1805.00341](https://arxiv.org/abs/1805.00341).
- [6] B. M. Gaensler, C Kouveliotou, J. D. Gelfand, G. B. Taylor, D Eichler, R. A.M. J. Wijers, J Granot, E Ramirez-Ruiz, Y. E. Lyubarsky, R. W. Hunstead, D. Campbell-Wilson, A. J. v. d. Horst, M. A. McLaughlin, R. P. Fender, M. A. Garrett, K. J. Newton-McGee, D. M. Palmer, N. Gehrels, and P. M. Woods. An expanding radio nebula produced by a giant flare from the magnetar SGR 1806-Å§20. *Nature*, 434(7037):1104–1106, 2005. ISSN: 0028-0836. doi: [10.1038/nature03498](https://doi.org/10.1038/nature03498).
- [7] H. T. Cromartie, E. Fonseca, S. M. Ransom, P. B. Demorest, Z. Arzoumanian, H. Blumer, P. R. Brook, M. E. DeCesar, T. Dolch, J. A. Ellis, R. D. Ferdman, E. C. Ferrara, N. Garver-Daniels, P. A. Gentile, M. L. Jones, M. T. Lam, D. R. Lorimer, R. S. Lynch, M. A. McLaughlin, C. Ng, D. J. Nice, T. T. Pennucci, R. Spiewak, I. H. Stairs, K. Stovall, J. K. Swiggum, and W. Zhu. A very massive neutron star: relativistic Shapiro delay measurements of PSR J0740+6620. *arXiv preprint arXiv:1904.06759*, 2019. arXiv: [1904.06759](https://arxiv.org/abs/1904.06759).
- [8] F. J. Llanes-Estrada and E. Lope-Oter. Hadron matter in neutron stars in view of gravitational wave observations. *Progress in Particle and Nuclear Physics*:103715, 2019. arXiv: [1907.12760](https://arxiv.org/abs/1907.12760).

- [9] A. W. Steiner, J. M. Lattimer, and E. F. Brown. The neutron star mass-radius relation and the equation of state of dense matter. *The Astrophysical Journal Letters*, 765(1):L5, 2013.
- [10] S. Guillot, M. Servillat, N. A. Webb, and R. E. Rutledge. Measurement of the radius of neutron stars with high signal-to-noise quiescent low-mass X-ray binaries in globular clusters. *The Astrophysical Journal*, 772(1):7, 2013.
- [11] V. Kalogera and G. Baym. The Maximum Mass of a Neutron Star. *Phys. Rev. Lett.*, 32(6):324–327, 1996. DOI: [10 . 1086 / 310296](https://doi.org/10.1103/PhysRevLett.32.324). arXiv: [9608059 \[astro-ph\]](https://arxiv.org/abs/9608059).
- [12] M. Alford, D. Blaschke, A. Drago, T Klähn, G. Pagliara, and J. Schaffner-Bielich. Astrophysics: Quark matter in compact stars? *Nature*, 445(7125):E7, 2007.
- [13] F. Weber. *Pulsars as Astrophysical Laboratories for Nuclear and Particle Physics (Series in High Energy Physics, Cosmology and Gravitation)*. CRC Press, 1999, page 696. ISBN: 0750303328.
- [14] V. Dexheimer. *Chiral Symmetry Restoration and Deconfinement in Neutron Stars*. PhD thesis, Johann Wolfgang Goethe-Universitaet, 2009, page 104.
- [15] Schaffner-Bielich. Compact Star Physics. Vorlesungsskript.
- [16] N. K. Glendenning. *Compact stars: Nuclear physics, particle physics and general relativity*. Springer Science & Business Media, 2012, page 468. ISBN: 978-0-387-98977-8.
- [17] M. E. Gusakov, D. G. Yakovlev, P. Haensel, and O. Y. Gnedin. Direct Urca process in a neutron star mantle. *Astronomy & Astrophysics*, 421(3):1143–1148, 2004. ISSN: 0004-6361. DOI: [10 . 1051 / 0004 - 6361 : 20040288](https://doi.org/10.1051/0004-6361:20040288).
- [18] K. Schwarzschild. On the gravitational field of a mass point according to Einstein’s theory. *arXiv preprint physics/9905030*, 1999. arXiv: [9905030 \[physics\]](https://arxiv.org/abs/9905030).
- [19] G. D. Birkhoff and R. E. Langer. *Relativity and modern physics*. Harvard University Press, 1923. ISBN: 9780674734487.
- [20] E. Alécian and S. M. Morsink. The effect of neutron star gravitational binding energy on gravitational radiation-driven mass-transfer binaries. *The Astrophysical Journal*, 614(2):914, 2004.
- [21] D. J. Griffiths. *Introduction to electrodynamics*. Cambridge University Press, 2005, page 620. ISBN: 1108420419.
- [22] P. Landry and E. Poisson. Relativistic theory of surficial Love numbers. *Physical Review D*, 89(12):124011, 2014. ISSN: 1550-7998. DOI: [10 . 1103 / PhysRevD.89.124011](https://doi.org/10.1103/PhysRevD.89.124011). arXiv: [1404.6798](https://arxiv.org/abs/1404.6798).

- [23] T. Regge and J. A. Wheeler. Stability of a Schwarzschild Singularity. *Physical Review*, 108(4):1063–1069, 1957. ISSN: 0031-899X. doi: [10.1103/PhysRev.108.1063](https://doi.org/10.1103/PhysRev.108.1063).
- [24] T. Hinderer, L. Rezzolla, and L. Baiotti. Gravitational Waves from Merging Binary Neutron-Star Systems. In *The Physics and Astrophysics of Neutron Stars*, pages 575–635. Springer, 2018. doi: [10.1007/978-3-319-97616-7\\_10](https://doi.org/10.1007/978-3-319-97616-7_10).
- [25] A. E. H. Love. The Yielding of the Earth to Disturbing Forces. *Proceedings of the Royal Society A: Mathematical, Physical and Engineering Sciences*, 82(551):73–88, 1909. ISSN: 1364-5021. doi: [10.1098/rspa.1909.0008](https://doi.org/10.1098/rspa.1909.0008).
- [26] K. S. Thorne and A. Campolattaro. Non-Radial Pulsation of General-Relativistic Stellar Models. I. Analytic Analysis for  $L \leq 2$ . *The Astrophysical Journal*, 149:591, 1967. ISSN: 0004-637X. doi: [10.1086/149288](https://doi.org/10.1086/149288).
- [27] T. Damour and A. Nagar. Relativistic tidal properties of neutron stars. *Physical Review D*, 80(8):84035, 2009. doi: [10.1103/PhysRevD.80.084035](https://doi.org/10.1103/PhysRevD.80.084035). arXiv: [0906.0096](https://arxiv.org/abs/0906.0096).
- [28] E. E. Flanagan and T. Hinderer. Constraining neutron star tidal Love numbers with gravitational wave detectors. *Physical Review D*, 77(2):021502, 2007. ISSN: 1550-7998. doi: [10.1103/PhysRevD.77.021502](https://doi.org/10.1103/PhysRevD.77.021502). arXiv: [0709.1915](https://arxiv.org/abs/0709.1915).
- [29] T. Binnington and E. Poisson. Relativistic theory of tidal Love numbers. *Physical Review D*, 80(8):084018, 2009. ISSN: 1550-7998. doi: [10.1103/PhysRevD.80.084018](https://doi.org/10.1103/PhysRevD.80.084018). arXiv: [0906.1366](https://arxiv.org/abs/0906.1366).
- [30] D. Bandyopadhyay, S. A. Bhat, P. Char, and D. Chatterjee. Moment of inertia, quadrupole moment, Love number of neutron star and their relations with strange matter equations of state. *The European Physical Journal A*, 54(2):26, 2017. ISSN: 1434-6001. doi: [10.1140/epja/i2018-12456-y](https://doi.org/10.1140/epja/i2018-12456-y). arXiv: [1712.01715](https://arxiv.org/abs/1712.01715).
- [31] J. M. Bardeen, K. S. Thorne, and D. W. Meltzer. A Catalogue of Methods for Studying the Normal Modes of Radial Pulsation of General-Relativistic Stellar Models. *The Astrophysical Journal*, 145:505, 1966. ISSN: 0004-637X. doi: [10.1086/148791](https://doi.org/10.1086/148791).
- [32] T. Hinderer, B. D. Lackey, R. N. Lang, and J. S. Read. Tidal deformability of neutron stars with realistic equations of state and their gravitational wave signatures in binary inspiral. *Physical Review D*, 81(12):123016, 2009. ISSN: 1550-7998. doi: [10.1103/PhysRevD.81.123016](https://doi.org/10.1103/PhysRevD.81.123016). arXiv: [0911.3535](https://arxiv.org/abs/0911.3535).
- [33] A. Urbano and H. Veermäe. On gravitational echoes from ultracompact exotic stars. *Journal of Cosmology and Astroparticle Physics*, 2019(04):11, 2018. doi: [10.1088/1475-7516/2019/04/011](https://doi.org/10.1088/1475-7516/2019/04/011). arXiv: [1810.07137](https://arxiv.org/abs/1810.07137).

- [34] N. Chamel, P. Haensel, J. L. Zdunik, and A. F. Fantina. On the maximum mass of neutron stars. *International Journal of Modern Physics E*, 22(07):1330018, 2013.
- [35] E. Annala, T. Gorda, A. Kurkela, and A. Vuorinen. Gravitational-wave constraints on the neutron-star-matter Equation of State. *Physical Review Letters*, 120(17):172703, 2018.
- [36] B. P. Abbott, R. Abbott, T. D. Abbott, F. Acernese, K. Ackley, C. Adams, T. Adams, P. Addesso, R. X. Adhikari, V. B. Adya, and Others. GW170817: observation of gravitational waves from a binary neutron star inspiral. *Physical Review Letters*, 119(16):161101, 2017.
- [37] N. K. Glendenning and C. Kettner. Non-identical neutron star twins. *arXiv preprint astro-ph/9807155*, 1998.
- [38] M. G. Alford, S. P. Harris, and P. S. Sachdeva. On the stability of strange dwarf hybrid stars. *The Astrophysical Journal*, 847(2):109, 2017.
- [39] S Chandrasekhar. Dynamical instability of gaseous masses approaching the Schwarzschild limit in general relativity. *Physical Review Letters*, 12(4):114, 1964.
- [40] M. G. Alford and S. Han. Characteristics of hybrid compact stars with a sharp hadron-quark interface, 2016. arXiv: [arXiv:1508.01261v2](https://arxiv.org/abs/1508.01261v2).
- [41] J. E. Christian, A. Zacchi, and J. Schaffner-Bielich. Classifications of twin star solutions for a constant speed of sound parametrized equation of state. *European Physical Journal A*, 54(2), 2018. ISSN: 1434601X. doi: [10.1140/epja/i2018-12472-y](https://doi.org/10.1140/epja/i2018-12472-y). arXiv: [1707.07524](https://arxiv.org/abs/1707.07524).
- [42] C. Gattringer and C. Lang. *Quantum chromodynamics on the lattice: an introductory presentation*. Springer Science & Business Media, 2009, page 788.
- [43] C. Gattringer and K. Langfeld. Approaches to the sign problem in lattice field theory. *International Journal of Modern Physics A*, 31(22):1643007, 2016.
- [44] T. Klähn and T. Fischer. Vector interaction enhanced bag model for astrophysical applications. *The Astrophysical Journal*, 810(2):134, 2015.
- [45] D. Rischke. Theoretische Physik VI: Fortgeschrittene Quantenmechanik. University Lecture, 2016.
- [46] S. Weinberg. *Dreams of a final theory*. Vintage, 1994, page 352. ISBN: 0679744088.
- [47] A. Motornenko, V. Vovchenko, J. Steinheimer, S. Schramm, and H. Stoecker. QCD at high density: Equation of state for nuclear collisions and neutron stars. *Nuclear Physics A*, 982:891–894, 2019.
- [48] P. N. Bogoliubov. Sur un modèle à quarks quasi-indépendants. *Annales de l'IHP Physique théorique*, 8(2):163–189, 1968.

- [49] A. Chodos, R. L. Jaffe, K. Johnson, C. B. Thorn, and V. F. Weisskopf. New extended model of hadrons. *Physical Review D*, 9(12):3471–3495, 1974. ISSN: 0556-2821. doi: [10.1103/PhysRevD.9.3471](https://doi.org/10.1103/PhysRevD.9.3471).
- [50] P. J. Stachel and P. D. K. Reygers. QGP Physics – From Fixed-Target to LHC . Thermodynamics of the QGP. *Physics*:1–32, 2011.
- [51] J. Stachel, M. Oberthaler, T. Gasenzer, and J. Pawłowski. Lattice QCD and QGP. *Preseminar Extreme Matter Institute EMMI Workshop on Quark-Gluon-Plasma and Cold Atomic Physics*:1–10, 2008.
- [52] S Théberge, A. W. Thomas, and G. A. Miller. Pionic corrections to the MIT bag model: The (3,3) resonance. *Physical Review D*, 22(11):2838–2852, 1980. ISSN: 0556-2821. doi: [10.1103/PhysRevD.22.2838](https://doi.org/10.1103/PhysRevD.22.2838).
- [53] E. Rodionov. *The MIT bag model in nuclear and particle physics*. PhD thesis, The University Of Adelaide, 1997.
- [54] N. T. Anh. The Bag Model of Nuclei. Lecture Notes. 1993, page 30. arXiv: [9912029 \[physics\]](https://arxiv.org/abs/9912029).
- [55] R. K. Bhaduri and G. Karl. Models of the Nucleon: From Quarks to Soliton. *Physics Today*, 42(6):76–76, 1989. ISSN: 0031-9228. doi: [10.1063/1.2811056](https://doi.org/10.1063/1.2811056).
- [56] M. Thaler. *Phases of QCD: Lattice Thermodynamics and Quasiparticle Approaches*. PhD thesis, Technische Universitaet Muenchen, 2006, page 147.
- [57] C. Yagnik. The MIT Bag Model. *Summer Research Fellowship Programme of India's Science Academies* 2017:1–26, 2017.
- [58] M. Hanusaue. *Eigenschaften von kompakten Sternen in QCD motivierten Modellen*. PhD thesis, Johann Wolfgang Goethe Universitaet, 2004, page 244.
- [59] D. H. Rischke, Y. Pürsün, and J. A. Maruhn. Relativistic hydrodynamics for heavy-ion collisions. II. Compression of nuclear matter and the phase transition to the quark-gluon plasma. *Nuclear Physics, Section A*, 595(3):383–408, 1995. ISSN: 03759474. doi: [10.1016/0375-9474\(95\)00356-3](https://doi.org/10.1016/0375-9474(95)00356-3). arXiv: [9504021v1 \[arXiv:nucl-th\]](https://arxiv.org/abs/9504021v1).
- [60] A Bazavov, H.-T. Ding, P Hegde, O Kaczmarek, F Karsch, N Karthik, E Laermann, A. Lahiri, R Larsen, S.-T. Li, and Others. Chiral crossover in QCD at zero and non-zero chemical potentials. *Physics Letters B*, 795:15–21, 2019.
- [61] T. Klähn and T. Fischer. Vector interaction enhanced Bag model for astrophysical applications. *The Astrophysical Journal*, 810(2):134, 2015. ISSN: 1538-4357. doi: [10.1088/0004-637X/810/2/134](https://doi.org/10.1088/0004-637X/810/2/134). arXiv: [1503.07442](https://arxiv.org/abs/1503.07442).
- [62] J. Steinheimer and S. Schramm. The problem of repulsive quark interactions - Lattice versus mean field models. *Physics Letters B*, 696(3):257–261, 2010. doi: [10.1016/j.physletb.2010.12.046](https://doi.org/10.1016/j.physletb.2010.12.046). arXiv: [1005.1176](https://arxiv.org/abs/1005.1176).

- [63] J. Steinheimer and S. Schramm. Do lattice data constrain the vector interaction strength of QCD? *Physics Letters B*, 736:241–245, 2014. DOI: [10.1016/j.physletb.2014.07.018](https://doi.org/10.1016/j.physletb.2014.07.018). arXiv: [1401.4051](https://arxiv.org/abs/1401.4051).
- [64] T Klähn, R Łastowiecki, and D. Blaschke. Implications of the measurement of pulsars with two solar masses for quark matter in compact stars and heavy-ion collisions: A Nambu–Jona-Lasinio model case study. *Physical Review D*, 88(8):85001, 2013.
- [65] R. O. Gomes, P. Char, and S. Schramm. Constraining strangeness in dense matter with GW170817. *The Astrophysical Journal*, 877(2):139, 2019.
- [66] J. Antoniadis, P. C. C. Freire, N. Wex, T. M. Tauris, R. S. Lynch, M. H. v. Kerkwijk, M. Kramer, C. Bassa, V. S. Dhillon, T. Driebe, and Others. A massive pulsar in a compact relativistic binary. *Science*, 340(6131):1233232, 2013.
- [67] M. Linares, T. Shahbaz, and J. Casares. Peering into the dark side: Magnesium lines establish a massive neutron star in PSR J2215+ 5135. *The Astrophysical Journal*, 859(1):54, 2018.
- [68] Y. Motohiro, Y. Kim, and M. Harada. Erratum: Asymmetric nuclear matter in a parity doublet model with hidden local symmetry [Phys. Rev. C 92, 025201 (2015)]. *Physical Review C*, 95(5):059903, 2017.
- [69] A. Mukherjee, J. Steinheimer, and S. Schramm. Higher-order baryon number susceptibilities: Interplay between the chiral and the nuclear liquid-gas transitions. *Physical Review C*, 96(2):25205, 2017.
- [70] M. Gell-Mann. A schematic model of baryons and mesons. In *Murray Gell-Mann: Selected Papers*, pages 151–152. World Scientific, 2010.
- [71] J. Steinheimer, S. Schramm, and H. Stöcker. Hadronic SU(3) parity doublet model for dense matter and its extension to quarks and the strange equation of state. *Physical Review C*, 84(4):45208, 2011.
- [72] V. Dexheimer, S. Schramm, and D. Zschiesche. Nuclear matter and neutron stars in a parity doublet model. *Physical Review C*, 77(2):25803, 2008.
- [73] K. Fukushima. Chiral effective model with the Polyakov loop. *Physics Letters B*, 591(3-4):277–284, 2004.
- [74] Y. Nambu and G. Jona-Lasinio. Dynamical Model of Elementary Particles Based on an Analogy with Superconductivity. I. *Physical Review*, 122(1):345–358, 1961. ISSN: 0031-899X. DOI: [10.1103/PhysRev.122.345](https://doi.org/10.1103/PhysRev.122.345).
- [75] Y. Nambu and G. Jona-Lasinio. Dynamical Model of Elementary Particles Based on an Analogy with Superconductivity. II. In *Physical Review*. Volume 124, number 1, pages 246–254. World Scientific, 1961. DOI: [10.1103/PhysRev.124.246](https://doi.org/10.1103/PhysRev.124.246).

- [76] G. Baym, C. Pethick, and P. Sutherland. The ground state of matter at high densities: equation of state and stellar models. *The Astrophysical Journal*, 170:299, 1971.
- [77] Y. Fujimoto, K. Fukushima, and K. Murase. Mapping neutron star data to the equation of state of the densest matter using the deep neural network. *arXiv preprint arXiv:1903.03400*, 2019. arXiv: [1903.03400](#).
- [78] L. Lindblom. Determining the nuclear equation of state from neutron-star masses and radii. *The Astrophysical Journal*, 398:569–573, 1992.
- [79] E. L. Oter, A. Windisch, F. J. Llanes-Estrada, and M. Alford. nEoS: Neutron Star Equation of State from hadron physics alone. *Journal of Physics G: Nuclear and Particle Physics*, 2019. arXiv: [1901.05271](#).
- [80] K Schertler, C Greiner, J Schaffner-Bielich, and M. H. Thoma. Quark phases in neutron stars and a third family of compact stars as signature for phase transitions. *Nuclear Physics A*, 677(1-4):463–490, 2000.
- [81] B. Freedman and L. McLerran. Quark star phenomenology. *Physical Review D*, 17(4):1109, 1978.
- [82] J. R. Oppenheimer and G. M. Volkoff. On Massive Neutron Cores. *Phys. Rev.*, 55(4):374–381, 1939. DOI: [10.1103/PhysRev.55.374](#).
- [83] P. Demorest, T. Pennucci, S. Ransom, M. Roberts, and J. Hessels. Shapiro delay measurement of a two solar mass neutron star. *nature*, 467(7319):1081, 2010. DOI: [10.1038/nature09466](#). arXiv: [1010.5788](#).
- [84] E. Witten. Cosmic separation of phases. *Physical Review D*, 30(2):272, 1984.
- [85] S. Borsányi, G Endrődi, Z Fodor, S. D. Katz, S Krieg, C Ratti, and K. K. Szabó. QCD equation of state at nonzero chemical potential: continuum results with physical quark masses at order  $\mu^2$ . *Journal of High Energy Physics*, 2012(8):53, 2012. ISSN: 1029-8479. DOI: [10.1007/JHEP08\(2012\)053](#).
- [86] M. A. R. Kaltenborn, N.-U. F. Bastian, and D. B. Blaschke. Quark-nuclear hybrid star equation of state with excluded volume effects. *Physical Review D*, 96(5):056024, 2017. ISSN: 2470-0010. DOI: [10.1103/PhysRevD.96.056024](#).
- [87] S. Soma. *Neutron Stars: Celestial Laboratories for Dense Matter*. Master’s thesis, Saha Institute of Nuclear Physics, India, 2019.
- [88] M. Gell-Mann. The Eightfold Way: A Theory of strong interaction symmetry, 1961. DOI: [10.1142/9789812836854\\_0006](#).
- [89] S. C. Walpole, D. Prieto-Merino, P. Edwards, J. Cleland, G. Stevens, and I. Roberts. The weight of nations: an estimation of adult human biomass. *BMC public health*, 12(1):439, 2012. DOI: [10.1186/1471-2458-12-439](#).